

**IMPROVING THE PRECISION AND ACCURACY  
OF MONTE CARLO SIMULATION  
IN POSITRON EMISSION TOMOGRAPHY**

Yani Picard

Medical Physics Unit  
McGill University, Montreal

September 1993

A thesis submitted to the Faculty of Graduate Studies and Research in partial fulfilment of the requirements of the degree of Master of Science.

© Yani Picard, 1993.

# **IMPROVING THE PRECISION AND ACCURACY OF MONTE CARLO SIMULATION IN PET**

Yani Picard

Medical Physics Unit  
McGill University, Montreal

September 1993

A thesis submitted to the Faculty of Graduate Studies and Research in partial fulfilment of the requirements of the degree of Master of Science.

© Yani Picard, 1993.

# TABLE OF CONTENTS

---

	Page
Abstract	iii
Résumé	iv
Acknowledgements	v
List of Figures	vi
List of Tables	ix
<b>CHAPTER 1</b>	
Positron Emission Tomography	1
1.1 What is Positron Emission Tomography	1
1.2 Decays processes and photon-matter interactions in PET studies	2
A. $\beta^+$ decay	3
B. Annihilation	4
C. Definition of linear attenuation coefficient	6
D. Compton scattering	7
E. Photoelectric absorption	11
1.3 Possible types of coincident detection in PET	12
1.4 Monte Carlo simulation of PET systems	14
A. DRG program	17
B. PHANTOM program	18
C. COLLIMATOR program	24
D. DETECTOR program	24
<b>CHAPTER 2</b>	
Reasons to Improve Monte Carlo Simulation	26
2.1 Introduction	26
2.2 Random number generator	27
2.3 Monte Carlo simulation efficiency of PET scanners	31
2.4 PETSIM's accuracy	34

<b>CHAPTER 3</b>	
<b>Improvements in Monte Carlo Simulation</b>	<b>36</b>
<b>3.1 Introduction</b>	<b>36</b>
<b>3.2 PETSIM's accuracy</b>	<b>36</b>
<i>A. Compton scattering: first parameter in look-up table</i>	<i>38</i>
<i>B. Photoelectric absorption: last five parameters in look-up table</i>	<i>40</i>
<b>3.3 Monte Carlo simulation efficiency of PET scanners</b>	<b>42</b>
<i>A. Improving the efficiency using variance reduction techniques</i>	<i>42</i>
<i>B. Improving the efficiency using recycling</i>	<i>45</i>
<b>CHAPTER 4</b>	
<b>Methodology to Validate the Improvements</b>	<b>54</b>
<b>4.1 Introduction</b>	<b>54</b>
<b>4.2 Building an Analytical Mean Projection</b>	<b>56</b>
<b>4.3 Superposing the Mean Projections</b>	<b>76</b>
<b>4.4 Comparing the Results</b>	<b>81</b>
<b>CHAPTER 5</b>	
<b>Results and Discussion</b>	<b>86</b>
<b>5.1 Introduction</b>	<b>86</b>
<b>5.2 Improvements in PETSIM's accuracy</b>	<b>86</b>
<b>5.3 Characteristics of a conventional Monte Carlo simulation</b>	<b>94</b>
<b>5.4 Efficiency improvements due to recycling</b>	<b>97</b>
<i>A. Time saved</i>	<i>103</i>
<i>B. Disk space saved</i>	<i>105</i>
<b>CHAPTER 6</b>	
<b>Conclusion</b>	<b>107</b>
<b>References</b>	<b>108</b>
<b>Appendix A: Example of a Simulation Batch File</b>	<b>113</b>
<b>Appendix B: Fitting of Photoelectric Coefficients</b>	<b>115</b>
<b>Appendix C: <math>\chi^2</math> Distribution</b>	<b>118</b>

# Abstract

---

PETSIM, a Monte Carlo simulation program of Positron Emission Tomography (PET) systems, was improved in terms of accuracy and efficiency. First, the accuracy, the speed and the ease of use of PETSIM were improved by using tabulated values of the Compton scattering and photoelectric absorption partial interaction attenuation coefficients for all common biological, collimator and detector materials. These were generated from chemical formula, or physical composition, and density of the absorbing medium.

Furthermore, simulations of PET systems waste considerable time generating events which will never be detected. For events in which the original photons are usually directed towards the detectors, the efficiency of the simulations was improved by giving the photons additional chances of being detected. For simulation programs which cascade the simulation process into source, collimation, and detection phases such as PETSIM, the additional detections resulted in an improvement in the simulation precision without requiring larger files of events from the source/phantom phase of the simulation. This also reduced the simulation time since fewer positron annihilations were needed to achieve a given statistical precision. This was shown to be a useful improvement over conventional Monte Carlo simulations of PET systems.

## Résumé

---

PETSIM, un programme de simulation Monte Carlo des systèmes de Tomographie par Émission de Positrons (TÉP), a été amélioré au point de vue précision et efficacité. Premièrement, la précision, la rapidité et la facilité d'utilisation de PETSIM a été améliorées grâce à l'utilisation de valeurs tabulées des coefficients partiels d'atténuation des interactions Compton et photo-électriques pour tous les matériaux biologiques et ceux des collimateurs et des détecteurs communément rencontrés en TÉP. Ceux-ci ont été générés à partir de leur formule chimique ou de leur composition physique et de leur densité.

De plus, les simulations de TÉP perdent énormément de temps à générer des événements qui ne seront jamais détectés. Pour les événements dont les photons sont généralement orientés vers les détecteurs, l'efficacité d'une simulation complète a été améliorée en donnant aux photons de nouvelles chances d'être détectés. Pour les programmes de simulations qui effectuent la simulation en phases, soit la simulation de la source, des collimateurs et des détecteurs, les détections additionnelles améliore la précision des simulation sans nécessité de fichiers d'événements de plus grande dimension de la part de la phase source de la simulation. Ceci a permis de réduire aussi le temps de simulation puisque moins d'annihilations de positrons sont nécessaires pour obtenir une précision statistique donnée. Ceci s'avère une amélioration utile des simulateurs Monte Carlo conventionnels.

# Acknowledgements

---

I would like to thank my supervisor, Dr. Thompson, for his support, his understanding and his recognition of my work. I also thank my girlfriend Nathalie for her patience, her efforts and her understanding. I want to express my recognition to my parents, they are responsible for my enchantment for nature. Finally, the financial support of a NSERC Postgraduate Scholarship during this work is gratefully acknowledged.

This thesis is dedicated to my fathers and to my sons.

# List of Figures

---

Figure 1.1	Schematic representation of (a) Compton scattering, (b) photoelectric absorption.	8
Figure 1.2	Dominant photon-matter interaction for various energies and absorbing materials (from ref. [9]).	10
Figure 1.3	The three types of coincident events occurring in PET (from ref. [12]).	13
Figure 3.1	The two curves, one below and one above the K-shell absorption edge energy, which completely describe the photoelectric absorption partial interaction linear attenuation coefficient.	41
Figure 3.2	Flow chart of recycling in the collimation phase of the simulation.	48
Figure 3.3	(a) Original photon track after source/phantom phase. (b) Recycling in collimation phase showing the effect of the random axial displacement on the original photon track.	49
Figure 3.4	Flow chart of recycling in the detection phase of the simulation.	51
Figure 3.5	(a) Original photon track after collimation phase. (b) Recycling in detection phase showing the effect of the random rotation on the original photon track.	52
Figure 4.1	Variables used to define a line of integration.	62
Figure 4.2	Definitions of $\psi_{min}$ , $\psi_{max}$ , $r_{min}$ and $r_{max}$ .	63
Figure 4.3	Geometrical example of $\theta_{max}$ as computed in Equation (4.15) for (a) $r_1 \leq h$ and for (b) $r_2 > h$ .	67
Figure 4.4	Triangle used to define $h$ .	68



Figure 4.5	Geometrical description of the variables used to define the detector functions. Only the ones related to the first coincident crystal are shown.	70
Figure 4.6	Attenuation geometry used to test the recycling procedure. (a) Transverse cross section of the geometry at $z=0$ . (b) Axial cross section of the geometry at $y=0$ .	73
Figure 4.7	Analytical mean projection for the simulated system.	76
Figure 4.8	The $\chi^2$ probability density with $\nu=64$ .	81
Figure 5.1	Command lines used by the PHANTOM program to define the attenuation geometry of a simple 10 cm radius 11 cm high cylindrical water phantom. (a) Previous PETSIM version. (b) New PETSIM version.	88
Figure 5.2	Examples of how well the parameters fit curves through photoelectric and Compton scattering partial linear attenuations coefficients. The data points are from XGAM.	91
Figure 5.3	Spectrum from PETSIM simulation for (a) true coincidences and (b) scattered coincidences	93
Figure 5.4	Comparison between the simulated mean projection of a long conventional Monte Carlo simulation and the theoretical mean projection. The system used was the one described in section 4.2.	95
Figure 5.5	Quality factor as a function of the total number of counts in the mean projection for part of the long conventional Monte Carlo simulation of the system described in section 4.2.	96
Figure 5.6	Comparison between the simulated mean projection of a simulation using the recycling procedure Col 1, Det 1 and the theoretical mean projection.	98
Figure 5.7	Comparison between the simulated mean projection of a simulation using the recycling procedure Col 3, Det 2 and the theoretical mean projection.	100
Figure 5.8	Quality factor for simulations using different recycling procedures. For each set, the left-hand data point corresponds to Det 1 and the right-hand, to Det 7 (Det 6 for the last set).	102

Figure 5.9	Relative simulation time required for 35 different recycling combinations compared to a conventional Monte Carlo simulation (100%) to obtain a given statistical precision.	103
Figure 5.10	Example of relative simulation time required for different phases of the simulation to obtain a given statistical precision.	104
Figure 5.11	Relative disk space required for 35 different recycling combinations compared to a conventional Monte Carlo simulation (100%) to obtain a given statistical precision.	105
Figure 5.12	Example of relative disk space required for different phases of the simulation to obtain a given statistical precision.	106

# List of Tables

---

Table 1.1	Maximum positron energy for the most frequently used radionuclides in PET.	4
Table 1.2	Information stored for each photon in GRH file.	17
Table 2.1	Comparison of the number of photons initially directed towards the detector ring versus the number of annihilations generated for different scanners.	31
Table 4.1	Summary of the parameters used to compute the theoretical mean projection.	74
Table 4.2	Analytical number of true coincident counts per pair of crystals when each photon of the pair is depositing 511.1 keV into the crystal at only one interaction point.	75
Table 5.1	Compton scattering and photoelectric absorption partial interaction linear attenuation coefficient parameters for biological materials.	87
Table 5.2	Compton scattering and photoelectric absorption partial interaction linear attenuation coefficient parameters for collimator materials.	87
Table 5.3	Compton scattering and photoelectric absorption partial interaction linear attenuation coefficient parameters for detector materials.	88
Table 5.4	Compton scattering and photoelectric absorption partial interaction linear attenuation coefficient parameters for packing materials and other solid materials.	89
Table 5.5	Compton scattering and photoelectric absorption partial interaction linear attenuation coefficient parameters for gases.	89
Table 5.6	Characteristics of a long conventional Monte Carlo simulation using PETSIM.	94

Table 5.7	Characteristics of the simulation using the recycling procedure Col 1, Det 1.	97
Table 5.8	Characteristics of the simulation using the recycling procedure Col 3, Det 2.	99

# Positron Emission Tomography

---

### 1.1 What is Positron Emission Tomography

Positron Emission Tomography (PET) is a medical imaging technique that quantitatively maps the distribution of physiologically interesting chemical compounds present in living biological systems. The compound of interest is labelled with a positron-emitting isotope such as carbon-11 ( $^{11}\text{C}$ ), nitrogen-13 ( $^{13}\text{N}$ ), oxygen-15 ( $^{15}\text{O}$ ) or fluorine-18 ( $^{18}\text{F}$ ). The first three are isotopes of the elements occurring most frequently in organic compounds. They are therefore particularly suitable for labelling biomolecules and drugs without changing their chemical and physical behaviour in the living organism.  $^{18}\text{F}$  is used as a substitute for hydrogen or hydroxyl groups.

The positron-emitting labelled compound is then administered by inhalation or intravenously to the subject under study. It is distributed throughout the organism in a manner determined by the biochemical processes which it undergoes. With the time, the number of unstable atoms labelling the compound decrease exponentially, each of them undergoing positron emission into its more stable form. The emitted positron travels up to a few millimetres from its nucleus origin before combining itself with a free electron of the surrounding medium. This unstable specie then annihilates. The annihilation process is characterized by the transformation of the total energy of the positron-electron system into electromagnetic energy. This usually takes the form of two simultaneously created photons with an energy of 511.1 keV each which diverge in opposite direction. If these two photons

are observed by two detectors in time coincidence on a detector ring surrounding the subject, the annihilation is assumed to have taken place on the line joining the two detectors. The detected events are then sorted in the form of projections of the activity distribution (of the annihilations) and can be converted to transaxial images by computation methods similar to those used in x-ray computed tomography. The projections measured are convolved with a filter function and projected back onto the image plane to produce an image matrix of the activity distribution. For a more detailed and completed description of PET systems, the reader is referred to [1,2].

This chapter introduces the reader to the basic principles and terminologies which are essential to understand this work. Section 1.2 discusses the interactions and decay processes which occur in PET. Section 1.3 introduces the three types of coincident detection which are possible. Section 1.4 deals with the basic principles of Monte Carlo simulation program before giving the description of PETSIM, a Monte Carlo simulation program used to simulate PET systems.

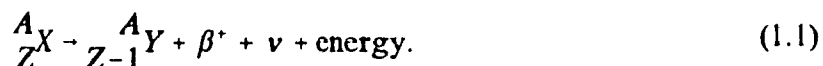
## **1.2 Decays processes and photon-matter interactions in PET studies**

As discussed in the previous section, the two principal decay processes in PET are the positron ( $\beta^+$ ) decay and the ( $\beta^+, \gamma$ ) decay (annihilation). The annihilation photons which have an initial energy of 511.1 keV can interact with matter by undergoing Compton scattering or photoelectric absorption. Pair production is not possible at 511.1 keV since the threshold for the pair production process is 1.022 MeV. The previous decay processes as well as the possible photon-matter interactions in PET studies are treated separately in the

following sub-sections. One of these sub-sections also defines the linear attenuation coefficient, an important parameter to determine the range of the photons in the medium and the relative probabilities of interaction.

#### A. $\beta^+$ decay

If a nucleus has one or more protons than a more stable nucleus, it can undergo  $\beta^+$  decay. In this radioactive decay, a proton of the unstable nucleus is transformed into a neutron and a positively charge electron or positron ( $\beta^+$ ). This positron and a neutrino are then ejected from the nucleus. Schematically, the process is



The parent radionuclide,  $X$ , and the daughter product,  $Y$ , represent different chemical elements because the atomic number,  $Z$ , of the parent decreases by one in the process. However, the mass number,  $A$ , does not change.

When a positron is emitted it has an energy ranging from zero to a maximum energy  $E_{max}$ . The value of  $E_{max}$  and the shape of the energy probability density depend on the parent nuclide, with the value of  $E_{max}$  for positron emitters ranging from tens of keV to several MeV. Table 1.1 shows the value of  $E_{max}$  for the most frequently used isotopes in PET.

**Table 1.1** Maximum positron energy for the most frequently used radionuclides in PET.

Radionuclides	Maximum Positron Energy (MeV)
Carbon 11	0.97
Nitrogen 13	1.19
Oxygen 15	1.70
Fluorine 18	0.64
Rubidium 82	3.35

### ***B. Annihilation***

The positron is the antiparticle of an ordinary electron. After ejection from the nucleus, the positron loses more than 99% of its energy through ionization and excitation interactions with the orbital electrons of the medium (collisional losses) and less than 1% through bremsstrahlung processes. During these collisions, the positron travels a few millimetres into the surrounding media in a zigzag path until it is finally brought to rest. This occurs within about  $10^{-9}$  sec. The actual range of the positron depends on its initial energy and the electron density of the absorbing medium. Because of the influence that the positron range can have on the spatial resolution of a PET system, several studies have examined the range of positron emitted from biomedically important nuclides in water (which is a tissue-equivalent material) [3,4,5]. The range probability density in water can be described by a sum of two exponentials such that the probability density  $f_{ann}$  for a positron to travel a distance  $r$  [cm] can be expressed as [3]:

$$f_{ann}(r) = \frac{A e^{-\frac{r}{r_1}} + (1 - A) e^{-\frac{r}{r_2}}}{A r_1 + (1 - A) r_2}, \quad (1.2)$$



where  $A$ ,  $r_1$  and  $r_2$  are three empirical parameters. They depend on the nuclide's maximum energy  $E_{max}$  given to the positron and the electron density of the medium. For example, for  $^{11}\text{C}$  in water, the parameters are  $A = 0.916$ ,  $r_1 = 0.078$  mm and  $r_2 = 0.457$  mm [3].

When the positron is nearly at rest, it then combines with one of the quasi-free (loosely bounded) electrons of the medium in an annihilation decay in which its mass and that of the electron are converted into energy to produce two photons. Annihilation into more than two photons is also possible but with a much smaller probability than two photon annihilation ( $10^{-4}$  times lower) [6]. Since two electron masses are converted, the total energy release is 1.022 MeV. To conserve momentum, the two photons or gamma rays, each having an energy of 511.1 keV, are ejected in opposite directions from the scene of the annihilation.

However, in general, the positron has a residual momentum, as does the free electron with which it interacts. The resulting centre-of-mass motion of the electron-positron system causes a Doppler broadening of the two 511.1 keV photon energies and a deviation of their relative directions from  $180^\circ$ . For PET systems, the Doppler broadening is not significant since energy resolution is not a critical factor, but the non-collinearity is, for large volume or high resolution detection systems. The probability density of the two photons' relative directional angle  $f(\alpha)$  can be approximately described as a Gaussian in water-equivalent materials with a mean of  $180^\circ$  and a full width at half maximum (FWHM) of  $0.5^\circ$  [7,8], that is:

$$f(\alpha) = \frac{1}{\sqrt{16\pi \cdot \ln 2 \cdot 0.5^\circ}} \cdot e^{-\frac{1}{2} \left( \frac{\alpha - 180^\circ}{\sqrt{8 \cdot \ln 2 \cdot 0.5^\circ}} \right)^2} \quad (1.3)$$

This effect is negligible in PET if the coincident detectors are relatively close. Before explaining the possible photon interactions in matter, let define an important parameter, the linear attenuation coefficient.

### *C. Definition of linear attenuation coefficient*

Suppose a beam of  $N$  photons impinges on a thin layer,  $dx$ , of an attenuator. The change in the number of photons in the beam,  $dN$ , is proportional to  $N$  and  $dx$  and may be written

$$dN = -\mu N dx \quad (1.4)$$

where  $\mu$  is the constant of proportionality called linear attenuation coefficient. The solution to this differential equation is

$$N = N_0 e^{-\mu x}, \quad (1.5)$$

where  $N_0$  is the initial number of photons and  $N$  is the number of photons which went through the layer.

After its creation, an annihilation photon of energy  $h\nu$  (511.1 keV or less if it already had an interaction) can, through its trajectory, interact with the surrounding medium. From Equation (1.5), the number of photons transmitted decreases exponentially with the thickness of the material. The range probability density  $f_\gamma(x)$  for a photon is thus

$$f_\gamma(x) = \mu e^{-\mu x}, \quad (1.6)$$

where  $x$  is the range and  $\mu$  is the linear attenuation coefficient. At 511.1 keV or less only Compton scattering and photoelectric absorption are possible. Thus in PET, the linear attenuation coefficient is

$$\mu = \sigma + \tau, \quad (1.7)$$

where  $\sigma$  is the Compton scattering partial interaction linear attenuation coefficient and  $\tau$  is the photoelectric absorption partial interaction linear attenuation coefficient. The linear attenuation coefficient depends on the energy of the photon since both the Compton scattering and photoelectric partial interaction linear attenuation coefficients depend on the energy. These coefficients are defined in the following sub-sections.

#### *D. Compton scattering*

After its creation, an annihilation photon of energy  $h\nu$  (511.1 keV or less if it already had an interaction) can, through its trajectory, collide with a free electron. After the collision, the photon is deflected and some of its initial kinetic energy and momentum are transmitted to the recoil electron which is set in motion. Figure 1.1(a) illustrates the process. Since energy and momentum are conserved, it can be shown using classical mechanics (see for example reference [9]) that if the scattered photon is emitted at an angle  $\theta$  to the incident photon direction, its energy,  $h\nu'$ , is given by:

$$h\nu' = \frac{h\nu}{1 + \frac{h\nu}{m_0 c^2} (1 - \cos\theta)}, \quad (1.8)$$

where  $m_0c^2$  is the rest-mass energy of the electron ( $m_0c^2 = 511.1$  keV).

The relative probability density of Compton scattering at an angle  $\theta$  may be determined by quantum mechanics analysis by calculating the probability of transition from the initial state of the system to the final state, both being described with suitable wave functions. By a complex analysis of this type, Klein and Nishina showed [10,11] that the differential Compton partial interaction linear attenuation coefficient  $d\sigma$  [ $\text{cm}^{-1}$ ] per unit solid angle  $d\Omega$  is given by:

$$\frac{d\sigma}{d\Omega} = \rho_e \frac{r_0^2}{2} (1 + \cos^2\theta) F_{\text{KN}}, \quad (1.9)$$

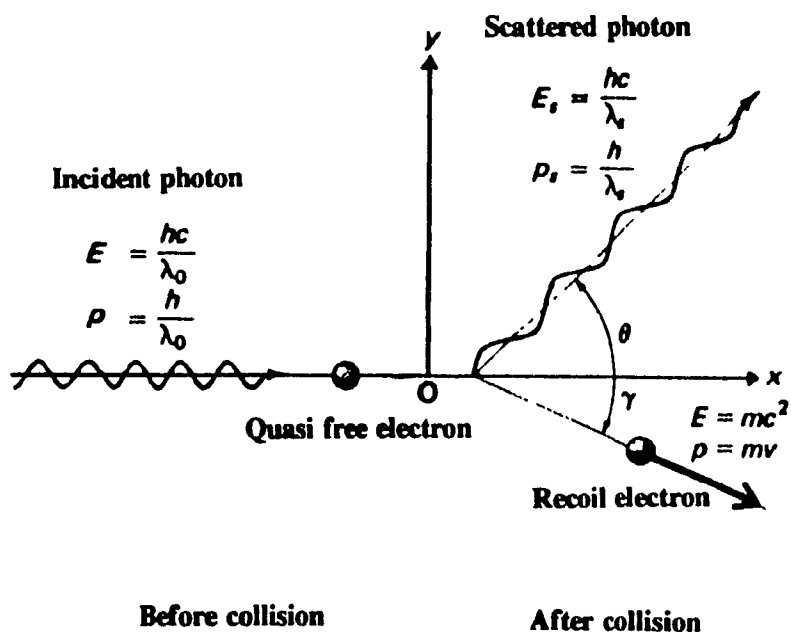
where  $r_0$  is the classical electron radius ( $2.817938 \times 10^{-13}\text{cm}$ ) and  $\rho_e$  is the electron density of the material [ $\text{electrons}/\text{cm}^3$ ]. The Klein-Nishina factor  $F_{\text{KN}}$  is:

$$F_{\text{KN}} = \left\{ \frac{1}{1 + \alpha(1 - \cos\theta)} \right\}^2 \left\{ 1 + \frac{\alpha^2(1 - \cos\theta)^2}{(1 + \alpha(1 - \cos\theta))(1 + \cos^2\theta)} \right\}, \quad (1.10)$$

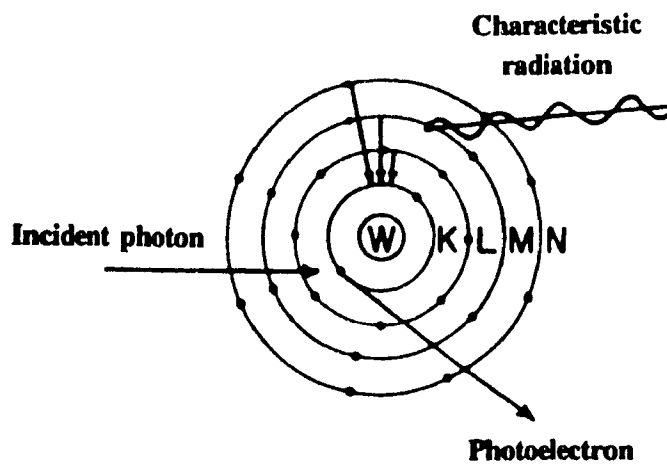
where  $\alpha$  is the initial reduced photon energy ( $h\nu/m_0c^2$ ). The probability density of Compton scattering at an angle  $\theta$  is then

$$f_o(\theta) = \frac{\frac{d\sigma}{d\Omega}}{\sigma}, \quad (1.11)$$

where  $\sigma$  is the Compton partial interaction linear attenuation coefficient. It is obtained by integrating Equation (1.9) over the solid angle. After integration, the Compton partial interaction linear attenuation coefficient  $\sigma$  is:



(a)



(b)

**Figure 1.1** Schematic representation of (a) Compton scattering, (b) photoelectric absorption.

$$\sigma = \rho_e \cdot 2\pi r_o^2 \left\{ \frac{1+\alpha}{\alpha^2} \left( \frac{2(1+\alpha)}{(1+2\alpha)} - \frac{\ln(1+2\alpha)}{\alpha} \right) + \frac{\ln(1+2\alpha)}{2\alpha} - \frac{1+3\alpha}{(1+2\alpha)^2} \right\}. \quad (1.12)$$

Notice that Equation (1.11) depends on the energy of the incident photon but does not depend on the electron density of the surrounding medium. However, Equation (1.12) shows that the Compton partial interaction linear attenuation coefficient depends on both the energy of the incident photon and the electron density of the medium.

The relative probability that a photon will interact with a free electron in a Compton process is simply the ratio between the Compton partial interaction linear attenuation coefficient and the linear attenuation coefficient ( $\sigma/\mu$ , where  $\mu$  is defined by Equation (1.7)). As illustrated in Figure 1.2, Compton scattering is the most important interaction mechanism in biological tissues ( $Z \approx 8$  for biological materials) for photons of the energies of interest in PET (from about 75 keV to 511.1 keV).

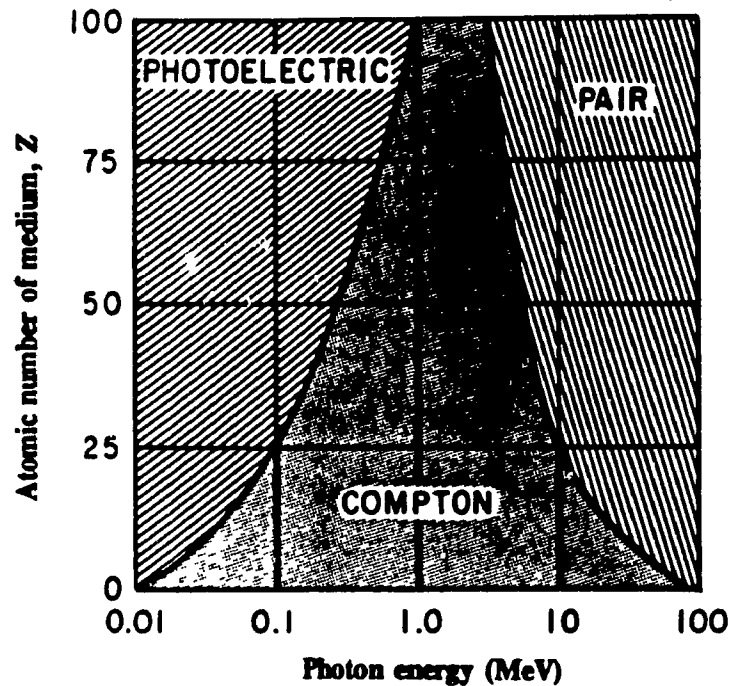


**Figure 1.2** Dominant photon-matter interaction for various energies and absorbing materials (from ref. [9]).

### *E. Photoelectric absorption*

An annihilation photon of energy  $h\nu$  can also collide with an atom and eject one of the orbital electrons from the K, L, M, or N shells. The ejection of the electron leaves the atom in an excited state so the atom emits characteristic X-ray radiation or Auger electrons. The process is illustrated in Figure 1.1b. Figure 1.2 shows that this process is the dominant interaction mechanism for photons of the energies of interest in PET for materials having an atomic number larger than about 50. This is usually the case for collimator and detector materials.

Photoelectric absorption is most likely to occur if the energy of the photon is slightly larger than the binding energy of the electron. Energies just less than the binding energy cannot eject the electron and therefore the cross section varies with energy in a complicated way with discontinuities at the energy corresponding to each shell. Experimentally, the photoelectric absorption partial interaction linear attenuation coefficient ( $\tau$ ) varies approximately as

$$\tau = a \cdot (h\nu)^{-b}, \quad (1.13)$$

where  $a$  and  $b$  are two fitting parameters which depends on the material. Parameter  $b$  is approximately equal to -3. The relative probability that a photon will undergo photoelectric absorption is the ratio between the photoelectric absorption partial linear attenuation coefficient and the linear attenuation coefficient ( $\tau/\mu$ ).

### 1.3 Possible types of coincident detection in PET

The reader is now aware of the possibility for the photons to interact with the surrounding medium and be either scattered or absorbed. Of course, the desirable type of detection in PET to reconstruct the activity distribution properly is the one which occurs when the two annihilation photons travel without any interaction and are observed by two detectors in time coincidence on the detector ring of the system. These are called true coincident events. Unfortunately, as explained in the previous section, as the annihilation photons pass through the biological tissues, they can interact with them and can undergo Compton scattering or photoelectric absorption. Photoelectric absorption, unimportant in biological tissues for photon of the energies of interest, transfers all the photon energy to an electron in the medium so coincident detection of the corresponding photon pair can not occur. Although this reduces the number of coincident events detected, it does not lead to an erroneous image. Compton scattering, however, is the most important interaction mechanism in biological materials. This type of interaction causes one or both photons of the pair to change direction before detection. This leads to erroneous information about the source location. Some of the scattered photons can be rejected by energy discrimination since the energy of the photon is changed when it scatters. However, since the average scattered photon energy lost is relatively small, a significant number of these events are still accepted. They are called scattered coincident events and constitute the second type of coincident detection in PET.

A third type of detection can also occur: two photons from two different annihilations can be detected in coincidence. These are called random coincidences. Thus,



as summarized in Figure 1.3, three types of coincident events exist in PET. Minimizing the detection of scattered and random coincident events while maintaining a high sensitivity for true coincident events is essential in the design of a PET system.

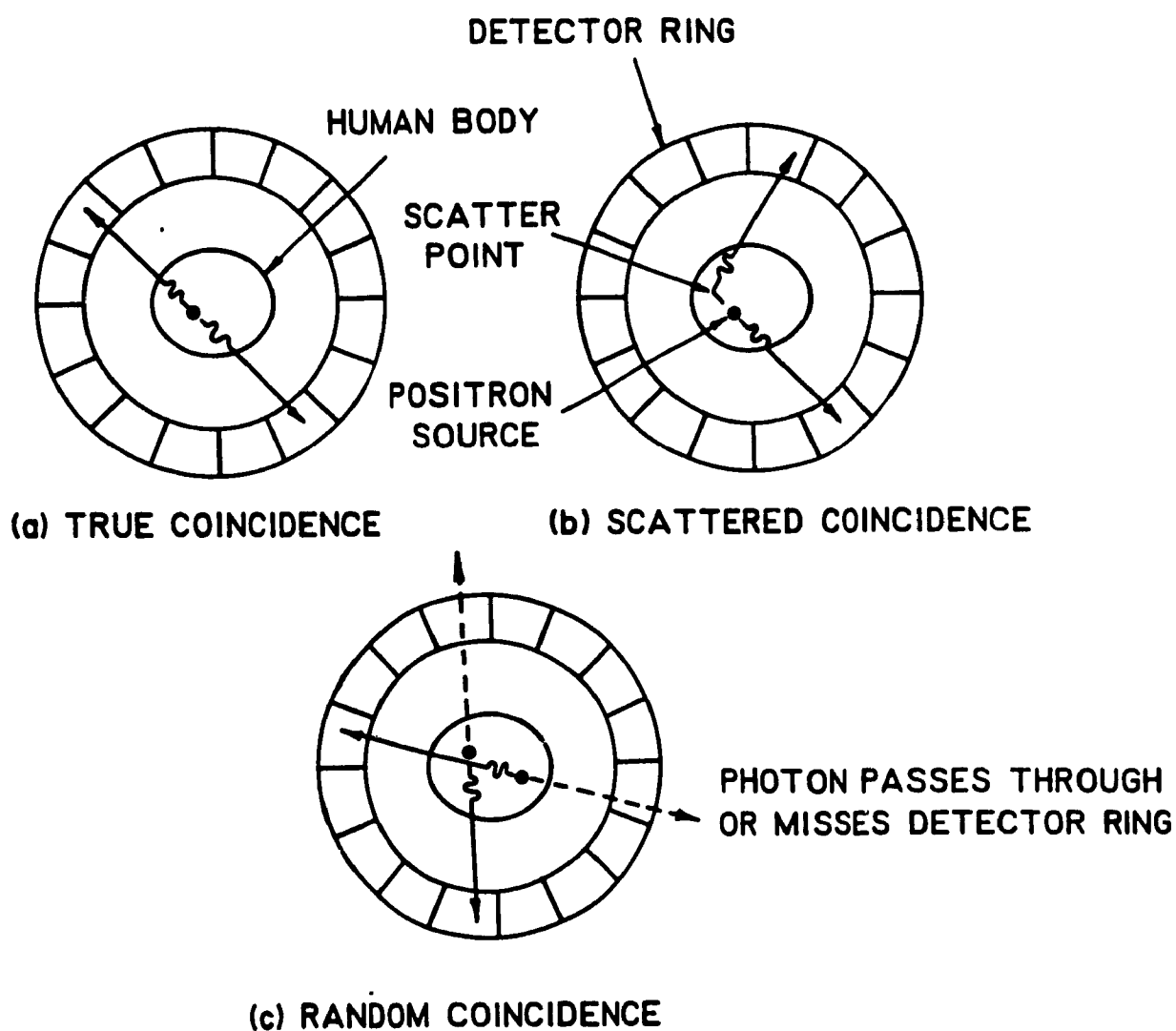


**Figure 1.3** The three types of coincident events occurring in PET (from ref. [12]).

### 1.4 Monte Carlo simulation of PET systems

Since minimizing the detection of scattered and random coincidences while maintaining a high sensitivity for true coincident events is essential in the design of a PET system, simulation of PET systems is a solution of choice and possibly the only one available for designer of PET systems to provide a knowledge of the performance of an imaging system before manufacturing it. Advantages of simulations over experimental measurements are that simulations on a digital computer can often be performed cheaply, quickly and yield information about the imaging system that would be difficult or even impossible to establish by direct physical measurement (for example, was the coincident event a true coincidence?). Recent advances in processing power and disk storage capacity as well as a continuing cost reductions have made simulation the most widely used and accepted tools to evaluate the performance of PET systems as well as other medical imaging devices.

Monte Carlo simulation [13,14,15,16] is a preeminently realistic simulation technique. It is performed by actually following each of a set of particles from the source throughout its life history to its "death" in some cases, its escape from the system or its detection in other cases. To determine its fate, the random quantities needed to track the particle are computed using random numbers and the elementary probability densities of the quantities at each stage of the particle history. Usually, a random quantity  $x$  having a probability density of the form  $f(x)$  is found from the relationship

$$x = F^{-1}(\epsilon) \quad (1.14)$$

where  $\epsilon$  is a random number in the unit interval  $[0,1]$  and  $F^{-1}(x)$  is the inverse of the probability distribution function defined by:

$$F(x) = \int_{-\infty}^x f(w) dw. \quad (1.15)$$

From these equations, it comes up, for example, that taking the logarithm of the random number gives an exponential probability distribution of  $x$ , and taking the square of the random number gives a square root probability distribution of  $x$ . To determine these random quantities which are very often related to the state of the particles, each particle is completely characterized by a set of parameters which are sufficient to determine its behaviour in all situations it may encounter during its history. These always include its position, its direction coordinates and its energy.

Monte Carlo Simulation method is appropriate to simulate PET systems since all the probabilities are known for the elementary events susceptible to occur in the life history of both the positron and the annihilation photons. The present state of development of high-speed digital computers permits the use of samples of a size sufficiently large to ensure satisfactory accuracy for the evaluation of the performance of a PET system (sensitivity, count-rate performance and resolution).

In the last 12 years, several Monte Carlo program have been developed to simulate linear PET detector arrays [17], single ring positron tomographs [18,19,20], Multi-Slice Positron Emission Tomography systems (MS-PET) [21,22,23,24,25,26] and, more recently, both MS-PET and Positron Volume Imaging systems (PVI) [27,28]. The Monte Carlo simulation programs used for the simulation of PET scanners at the Montreal Neurological Institute are called PETSIM. These programs are derived from the work of Lupton and Keller [19,29]. The original programs have been modified considerably to

permit more realistic simulations of modern PET scanners such as MS-PET and PVI systems [30,31,32,33,34,35]. The simulation programs are written in VMS FORTRAN and are now run on a VAXstation 4000/60. Monte Carlo simulation of PET systems using PETSIM is done in three phases using independent programs: the PHANTOM program is used to simulate the source/phantom phase, the COLLIMATOR program, to simulate the collimation phase and the DETECTOR program, to simulate the detection phase. The phases are linked together with intermediate gamma ray history (GRH) files stored on a disk or a tape. A GRH file is also produced by the DETECTOR program to analyze the results and compute the resolution of the scanner. Each GRH file is of identical format. It consists of a file header (64 lines of 80 characters) into which each program writes its geometric data in preallocated area. The bulk of the file contains all needed data on each photon processed. The data is saved in the most compact form possible to maximize the disk storage efficiency. Its format is given in Table 1.2. Executing the simulation in phases is more efficient when many collimator or detector geometries and materials are being compared for a given source distribution in the phantom, since the source distribution is simulated only once. The disadvantage is that for a given statistical precision of the final results large files of the gamma-rays emerging from the COLLIMATOR program and especially from the PHANTOM program are required.

The simulations are usually executed by running a VMS batch file containing the name of the simulation programs which the user wants to run and the data required for each of these programs. These independent programs are described below.

**Table 1.2** Information stored for each photon in GRH file.

<u>Details</u>	<u>Size</u>	<u>Range</u>	<u>Precision</u>
$x, y, z$ origin <sup>1</sup>	3x2 bytes	$\pm 64$ cm	0.002 cm
$x, y, z$ current position <sup>2</sup>	3x2 bytes	$\pm 64$ cm	0.002 cm
$\alpha, \beta, \gamma$ direction angles	3x2 bytes	$\pm 180^\circ$	0.01°
<b>Photon status:</b>	2 bytes:		
Photon type <sup>3</sup>	2 bits	0-3	Exact
Number of scatters <sup>4</sup>	3 bits	0-7	Exact
Number of interactions <sup>5</sup>	2 bits	1-4	Exact
Energy <sup>6</sup>	9 bits	0-511 keV	1 keV
<b>TOTAL:</b>	20 bytes		

<sup>1</sup> first photon of a pair has positron creation coordinates; second photon has positron annihilation coordinates

<sup>2</sup> or position of the interaction centroid within a detector block after detection phase

<sup>3</sup> first (0) or second (1) photon of a pair, unpaired photon in (2) or after (3) phantom phase

<sup>4</sup> before entering detector ring

<sup>5</sup> within a detector block, used only after detector phase

<sup>6</sup> of photon or deposited in a detector block after detection phase

### **A. DRG program**

The complete Monte Carlo simulation of a PET system using PIETSIM consists in first modelling the geometry of the imaging device in a batch file as well as the phantom to be imaged, including the attenuation characteristics of each material present within the source/phantom phase, the collimation phase and the detection phase. This is done by entering the coordinates and the dimensions of several nested solids such as boxes, cylinders or spheres. The source distribution of the activity is also geometrically modelled. It consists of lines, hollow or solid cylinders, spheres or boxes placed anywhere in the scanner's field of view (FOV). The user also specifies the positron emitter's  $E_{max}$  and the

non-collinearity angle FWHM. A relative activity concentration of the positron emitter under study is also assigned to each source. An example of a typical batch file is given in Appendix A, page 113.

Afterward, the information contained in the batch file can be displayed on the screen or plotted on a laser or colour printer using a program which the author wrote to familiarize himself with PETSIM before starting this work. The program is called DRG. The DRG program allows the user to see what the computer is asked to simulate and correct for any mistakes. The file header of any created GRH file can also be read and plotted with the DRG program to remind the user what was simulated. The simulation is then ready to be started.

### ***B. PHANTOM program***

The source/phantom phase of the simulation first calculates the volume of each activity region to obtain the correct fraction of  $\beta^+$  decays in each region. The computer then generates pseudo-random numbers uniformly distributed over the unit interval  $[0,1]$  using a multiplicative congruential pseudo-random generator [36]. To generate the numbers, the user enters an initial large odd integer seed  $s_0$  (32-bit integer). Every time the program requires a pseudo-random number, the generator updates the seed using the relation\*

$$s_i = |69069 \cdot s_{i-1} + 1|_{2^{32}}, \quad (1.16)$$

---

\* The notation signifies that  $s_i$  is the remainder when the value between the vertical lines is divided by  $2^{32}$ . This function is called modulo- $2^{32}$ .

and converts the high-order 24 bits to a floating-point number. These floating-point numbers are returned as a sequence of pseudo-random numbers.

These pseudo-random numbers are first used to locate the position of the  $\beta^+$  decay within the 3D source distribution by a well established technique [29] that produces a uniformly distributed positron creation density throughout each source region. The positron creation coordinates are part of the parameters recorded in the photon history. A positron then is emitted from that position with a direction randomly selected from a uniform probability density between 0 and  $2\pi$  (by multiplying the pseudo-random number by  $2\pi$ ) in the scanner's transverse plane (plane perpendicular to the axis of the scanner or  $xy$ -plane). From there, the positron travels for a distance based on Equation (1.2) where [37]

$$\begin{aligned} A &= 0.85, \\ r_1[\text{cm}] &= 0.085 \cdot E_{\max}[\text{MeV}], \\ r_2[\text{cm}] &= 0.660 \cdot E_{\max}[\text{MeV}]. \end{aligned} \tag{1.17}$$

The range of the positron is determined by integrating Equation (1.2), which gives the probability distribution of the range. However, the result is a sum of transcendental functions and its inverse is an explicit function of  $r$ . Thus, the technique described by Equations (1.14) and (1.15) can not be used to determine the positron range. Instead, numerical methods could be used to solve for  $r$  but these methods are time consuming. The distance travel by the positron is thus selected by two pseudo-random numbers. The first random number selects which term is going to be used to compute the range: if the random number is less than  $A$ , then only the first term will be used; otherwise, only the second term will be used. This gives a probability density such as:

$$f_{ann}(r) = \frac{1}{r_x} e^{-\frac{r}{r_x}}, \quad (1.18)$$

where  $r_x$  is equal to  $r_1$  or  $r_2$  depending on the first random number. That Equation can now be integrated between 0 and  $r$  (in a way similar to Equation (1.15)) to give a probability distribution such that:

$$P_{ann}(r) = \int_0^r p_{ann}(r) = 1 - e^{-\frac{r}{r_x}}. \quad (1.19)$$

The inverse of Equation (1.19) being an explicit function, the technique described by Equation (1.14) with the second pseudo-random number generated is used to determine the range. The positron is moved from its creation position to its annihilation position determined by its random range and direction. The annihilation coordinates are also part of the parameters recorded in the photon history.

After calculating the point of annihilation, PETSIM generates an annihilation producing two photons. The first photon direction is isotropic and is determined by a uniform probability density on a sphere [29]. The second gamma-ray direction is determined by an offset angle from the first photon direction derived from Equation (1.3) (the probability density of the offset angle) a pseudo-random number and the technique described by Equations (1.14) and (1.15). Its random azimuthal angle is selected from a uniform



distribution between 0 and  $2\pi^*$ . The FWHM of the Gaussian probability density of the offset angle is usually set to  $0.5^\circ$ , but can be set to any angle. The photons' direction and energy (511.1 keV) are then recorded as part of their own history parameters.

From now on, the simulation program tracks the two photons in matter. To do so, it first computes a random range for each photon of the pair to find out the location of an interaction point. To compute the random range, the linear attenuation coefficient of the surrounding medium must be known. It is defined as the sum of the Compton scattering and photoelectric absorption partial interaction linear attenuation coefficients (Equation (1.7)). These two partial interaction linear attenuation coefficients are computed using Equations (1.12) and ? for the energy of each photon and the electron density of the medium surrounding the origin of the photon. Once these quantities are calculated, the random range is selected using one pseudo-random number, Equation (1.6) (the probability density of the range) and the technique described by Equations (1.14) and (1.15).

The next step is to move each photon of the pair to the interaction location unless it when through the boundary of the attenuation region it was in. If it is the case, the photon is moved to the intersection of its path with the attenuation region boundary. A new photon range is then computed (as above) for the photon considering the photon energy and the attenuation properties of the material in the new region. The photon is then moved to the interaction location or again, the boundary of the current attenuation region.

---

\* PETSIM actually determines the direction of the second gamma ray by adding the offset angle to the projection of the first gamma ray direction on the X-Y plane.

At the interaction point, a pseudo-random number is generated to determine the type of interaction: if the random number is less than the ratio of the Compton partial interaction linear attenuation coefficient over the linear attenuation coefficient ( $\sigma/\mu$ ), the photon undergoes Compton scattering; otherwise, it undergoes photoelectric absorption.

If the photon undergoes photoelectric absorption, the photon is lost and nothing else has to be computed for that photon. It is discarded. However, if the photon undergoes Compton scattering, a new direction angle and energy has to be determined. The scattering angle is not easily computable since the inverse of its probability distribution (integration of Equation (1.11) between 0 and  $\theta$ ) is an implicit function and thus the technique described by Equations (1.14) can not be used. Instead, an equal-probability scatter group concept [12] is used to simulate the scattering process. These groups were computed before running any Monte Carlo programs. An initial 100 energy group structure was chosen based upon a mid-group energy of 511.1 keV for group 1 and a uniform step size of 5 keV between each mid-group energies down to a mid group energy of 16 keV for group 100. For each of the 100 mid-group energies, the probability density of the Compton partial interaction linear attenuation coefficient (Equation (1.11)) was numerically integrated in steps of  $0.1^\circ$ . This was done to find 100 groups with an equal-probability of scatter. The mid-scattering angle's cosine of the scatter group were tabulated and stored on disk for use in Monte Carlo simulation. In the Monte Carlo simulation the energy group is determined by the incident photon energy. A pseudo-random number uniformly distributed between 1 and 100 determines the scatter group within that energy group. The corresponding scattering angle's cosine is then used to compute the new photon energy (Equation (1.9)).

This scatter group concept determines one angle in space corresponding to the surface of a cone. The azimuthal angle of the new direction is determined by a uniform probability density between 0 and  $2\pi$ . The photon new direction is calculated from these two angle. A new range corresponding to the photon's new direction and energy is then selected randomly as explained above to find the position of another interaction point.

The process of computing photon's ranges and interaction characteristics goes on until the photon are photoelectrically absorbed or reaches the outside cylinder delimiting the phantom. At that point, the parameters of the photons are saved on disk in an output GRH file having the format specified in Table 1.2. The photons which reach the top or the bottom of the cylinder are discarded because their detection probability is almost inexistent. The storage is always done if both photons survive. To save storage space without losing precision for dead time and random count estimation, the singles are saved once in ten. However, they are always saved in the collimation and detection phase.

When the decision about the storage is taken, the photon is stored or discarded and another positron is generated. The same process, from the positron creation until the photon history is saved on disk or discarded, goes on again, until the GRH file which size was specified by the user is completely filled.

The program that tracks the particles from the positron creation until the outer cylinder delimiting the phantom is the first of the PETSIM simulation program. It is called PHANTOM. The positron range as well as the non-collinearity of the annihilation photons can be turned off by the user within the PHANTOM program. When one or both of them are turned off, the PHANTOM simulation program takes less time to fill the GRH file since

fewer random numbers and computation processes are necessary for each photon pair. The simulation is however less realistic.

### ***C. COLLIMATOR program***

The second program of the PETSIM Monte Carlo simulation programs is called COLLIMATOR. The collimator geometry is defined by nested hollow cylinders or frustra of cones (truncated cones). The collimator phase of the simulation reads the GRH file produced by the source/phantom phase and tracks the photons from the outside cylinder delimiting the phantom to the outside cylinder delimiting the collimator region using the same process as in the PHANTOM program. The photons that reach the collimator outside cylinder radius are all saved on disk in a new GRH file similar to the one in the PHANTOM program (Figure 1.4).

The COLLIMATOR program is less time consuming than the PHANTOM program since positrons are not generated in the scanner's collimator. Another reason for this is that the general direction of the photon is toward the detector ring: just a few photons unlikely to be detected are discarded. It is not the case in the PHANTOM program: the annihilations produce photons distributed isotropically. Thus, the PHANTOM program spend a lot of time generating photons which will never be detected.

### ***D. DETECTOR program***

The third program of PETSIM is called DETECTOR. As in most new PET scanners, the detector geometry is defined by an annulus made up of blocks of detector

material, separated by gaps which is filled with a dense material to absorb photons scattered from one detector block to the next. In a way similar to the PHANTOM and COLLIMATOR programs, the detection phase of the simulation tracks the photons from the outside cylinder delimiting the collimator region until the photon energy is less than the energy discriminator set up by the user or until the photon escapes from the detector region. As opposed to the two previous phases of PETSIM, the DETECTOR programs also keeps in memory all the interaction points of each photon within the detector material and the energy deposited at each point. For each photon having at least one interaction in the detector material, the centroid of all interaction within the individual blocks of the detecting material is computed based on the interaction positions weighted by the energy deposited at each interaction. The centroid of interaction of each photon is then stored in the DETECTOR GRH file (Figure 1.4).

At the end of the simulation the DETECTOR GRH file can be read by the ANALYZE program or the RESOLUTION program. These programs are used to analyze the performance and the resolution of the simulated PET system. Since these programs were not used for this work, they will not be described here. For a complete description of the ANALYZE and RESOLUTION programs, the reader is thus referred to reference [34].

# Reasons to Improve Monte Carlo Simulation

---

### 2.1 Introduction

An important concern in Monte Carlo simulation is to obtain a reasonably good statistical precision in the final results. Monte Carlo simulation is a simulation of a counting experiment where the data represent the number of events detected. It then follows Poisson statistics. Thus, the standard error on the final results (standard deviation of the sampling distributions) is inversely proportional to the square root of the sample size  $n$  and therefore, to reduce the standard error by a factor of  $k$ , the sample size needs to be increased  $k^2$ -fold. This reduction of the statistical precision becomes impracticable when  $k$  is large. The remedy lies in careful design of the way in which the data is collected and analyzed. The efficiency of a Monte Carlo process may be taken as inversely proportional to the product of the sampling variance (square of the standard error) and the amount of labour expended in obtaining the estimated results [15]. It pays handsome dividends to allow some increase in the labour if that decreases the sampling variance.

As well as the efficiency, another concern in Monte Carlo simulation is that the simulation replicates as much as possible the real system. For the simulation to be realistic, the simulated behaviour of the particles in all situations they may encounter during their history must match that of the real particles. In this work, the realism of the simulated particles' behaviour will be called the accuracy of the simulation.

In this chapter, the problems encountered with most Monte Carlo simulation programs used to simulate PET systems will be discussed. Section 2.2 concentrates on the way to generate random numbers in Monte Carlo simulation. Section 2.3 deals with the efficiency of Monte Carlo simulation programs for simulation time and disk storage space. In some cases, the discussion involves only the PETSIM programs. The reader will be informed conveniently when the former will apply. The last section of this chapter examines the accuracy of PETSIM.

## **2.2 Random number generator**

The essential feature common to all Monte Carlo simulations is that at some point the random variable has to be substituted by a corresponding sequence of values having the statistical properties of a random variable. These values are called random numbers on the grounds that they could well have been produced by chance by a suitable random process. But this approach runs into practical difficulties because strictly speaking, simulations require the production of an infinite set of random numbers and that an infinite set of statistical tests on them have to be made to ensure fully that they are really coming from a random process. To alleviate this problem, one could use published tables of random numbers for Monte Carlo work [38,39]. These tables are generated by physical processes which are, as far as one can tell, random in the strict sense, but they have also been successfully subjected to several statistical tests. But these tables do not contain an infinite set of random variables. Furthermore, for electronic digital computers, it is not convenient to store such large tables. It is possible to generate one's own random numbers by a

physical-like process [40] but is relatively slow. One then has the additional task of repeatedly verifying that the process is functioning properly.

For electronic digital computers it is most convenient to calculate a sequence of numbers one at a time as required, by a completely specified rule. However, this rule must be so devised that no reasonable statistical test will detect any significant departure from randomness. Such a sequence is called pseudo-random. The advantage of a specified rule is that the sequence can be exactly reproduced for computational checking.

In 1951, Lehmer [41] suggested that a pseudo-random sequence could be generated by the recurrence relation

$$s_i = |as_{i-1}|_m, \quad (2.1)$$

later generalized [42] to

$$s_i = |as_{i-1} + c|_m, \quad (2.2)$$

where  $m$  is a large integer determined by the design of the computer (usually a large power of 2) and  $a$ ,  $c$  and  $s_i$  are integers between 0 and  $m-1$ . Usually the pseudo-random sequence  $\epsilon_i$  is computed from the sequence of positive integers  $s_i$  via the relation

$$\epsilon_i = \frac{s_i}{m}. \quad (2.3)$$

Equation (2.2) is known as the multiplicative congruential method of generating pseudo-random numbers.

Such a sequence will repeat itself after at most  $m$  steps, and will therefore be periodic. For example, if  $m = 16$ ,  $a = 3$ ,  $c = 1$  and  $s_0 = 2$ , the sequence of  $s$ 's generated



by (2.2) is 2, 7, 6, 3, 10, 15, 14, 11, 2, 7, ..., so that the period is 8. Since Monte Carlo simulation requires a very large set of random numbers, one must always ensure that the period is longer than the number of random numbers required in any single experiment. The value of  $m$  is usually large enough to permit this. But, it can be shown [43] that if recurrence (2.1) is used the period is always less than  $m$ . However, if recurrence (2.2) is used, the full period of  $m$  can always be achieved if [43]:

- (i)  $c$  and  $m$  have no common divisor;
- (ii)  $|a|_p \equiv 1$  for every prime factor  $p$  of  $m$ ;
- (iii)  $|a|_4 \equiv 1$  if  $m$  is a multiple of 4.

Fortunately, this is the case for the random number generator of VMS FORTRAN (Equation (1.16)) used by the PETSIM program. For this particular generator,  $a$  is 69069,  $c$  is 1 and  $m$  is  $2^{32}$ . Since the random numbers are generated using the 24 most significant bits to produce the random number, the computer will divide these by  $2^{24}$  instead of  $m$  as computed in Equation (2.3), to obtain a floating point numbers uniformly distributed [35] between the unit interval  $[0, 1]$ . Thus, the generator provide a sequence of  $2^{32}$  random numbers from a set of  $2^{24}$  different floating points. This allows the PHANTOM program of PETSIM to produce many random events from the positron creation position until the photons are stored in the GRH file or are lost.

The number of different random events produced in a single simulation run could be as large as the random number generator period if care is taken to ensure that the first seed of every event are all different. Remember that one random event requires many random numbers. These imply that even if the total number of random numbers generated

during a single simulation run is larger than the random number generator period, new random events can still be produced. To ensure that the first seed of all random events are different the PHANTOM program warns the user when the first seed of a random event is the same as the first seed of the first random event generated by this source simulation program. The exact number depends on the source and the attenuation geometry complexity as well as the average number of random numbers used to generate the random events. For example, an average of 28.6 random numbers per annihilation are required to the PHANTOM program to track the photons outside a simple 10 cm high and 10 cm radius cylindrical water flood phantom, when the program includes the positron range (3 random numbers per annihilation), the non-collinearity of the photon pair (2 random number per annihilation) and the attenuation in water.

From the instant where a random event has the same seed as the first random event generated for a given run, it is useless to run the simulation for a longer time: the random event sequence is going to repeat itself. To alleviate this problem, one could increase the random number generator period by using a more complicated or a larger random number generator. Another solution is to change the stride of the random number generator [44]. These possible improvements on the random number generator will not be considered in this thesis because any attempt to increase the period of the random number generator would slow down the simulations. A VAXstation 4000/60 takes 3.6 sec to generate 1 million random numbers in a loop using the random number generator of VMS FORTRAN (Equation (1.16)). Other systems are given in reference [35].

The repetition of the random number sequence is less important in the COLLIMATOR program and in the DETECTOR program. In these programs, each photon is tracked randomly, starting from a random location read from the GRH file. So even if the first seed of a random track generated is the same as the first seed of the first random track generated in the run, the events will still be different: it is unlikely that the starting locations of the two corresponding photons will be the same.

### 2.3 Monte Carlo simulation efficiency of PET scanners

Most of the photons generated following positron annihilation in subjects undergoing PET studies never reach the detectors of the imaging device. Similarly, simulations of PET systems waste considerable time generating events which are not directed toward the detector ring and thus will never be detected. Table 2.1 gives the ratio between the number of pairs of photons or singles that are directed towards the detector ring and the

**Table 2.1** Comparison of the number of photons initially directed towards the detector ring versus the number of annihilations generated for different scanners.

Scanner	Detector ring diameter (cm)	Detector height (cm)	Maximum axial acceptance angle (°)	Coincidence ratio (%)	Singles ratio (%)
HEAD PENN-PET	42.0	21.4	27.0	12.1	24.6
Scanditronix PC2048-B	50.5	10.0	11.2	9.97	20.3
PENN-PET Scanner	84.0	12.8	8.7	5.94	12.0

total number of annihilations that occurs within the source volume for different brain and body scanners. The source was a typical 20 cm water-filled cylinder 10 cm high phantom simulated with the PHANTOM program including positron range and non-collinearity effect. However, all attenuations within the water phantom itself or the collimator septa were excluded to emphasize on the number of photons which are initially directed toward the detector ring as opposed to the ones which would reach the detector in a normal simulation including the attenuation and scattering effects. The ratios were taken as the number of coincident photons or singles that were reaching the detector ring inner surface over the total number of annihilations generated by the PHANTOM program (between 5 and 10 millions annihilations, depending on the scanner). So even with the HEAD PENN-PET, the scanner having the largest acceptance angle (defined as the arctangent of the ratio detector ring height over its diameter), 63.3% of the annihilations generated ( $100 - (12.1 + 24.6)$ ) produced photons which were not directed towards the detector ring. Furthermore, only 12.1% of these annihilations produce photon pairs for which both photons were directed towards the detector ring. These results were even worse for the two other scanners. Solutions suggested [35,45] to alleviate this problem will be discussed in the next chapter. Notice that the water attenuation will further reduce the ratio of coincidences (both true and scattered) by a factor of about 2 and slightly increase the singles ratio since some photons will be unpaired due to absorption or scattering. The use of collimator septa will also decrease the ratio of coincidences. Lower ratios of coincidences signify that simulations have to be run for a longer time to obtain a given statistical precision.

As explained above, simulation of PET systems is not efficient in terms of events detected versus the number of annihilations generated. Nevertheless, continuing cost reduction in processing power and disk storage have allowed improved precision of recent simulation programs. Faster computers reduce simulation time. For example, consider the simulation of a typical simple 20 cm diameter 10 cm high water-filled cylindrical phantom with the PHANTOM program of PETSIM which includes positron range and non-collinearity effects and tracks both photons until they are absorbed or emerge from a 50 cm diameter, 12 cm high cylinder. This creates only 25000 positrons per minute on a VAXstation 3100 but over 120000 positrons per minute on a VAXstation 4000/60. The present practical limit is actually imposed by the 4.5 Gbyte storage capacity of an Exabyte 8500 tape. Since one gamma ray history takes 20 bytes of memory in the GRH file, over 225 million gamma ray histories can be saved in a 4.5 Gbyte file, representing the decay of several billion atoms.

Besides storing the photon information in a compact format (see Figure 1.4, page 17), the PETSIM simulation programs have always recognized the importance of sampling to avoid storing photons which are going to be irrelevant to the final results to get the most of the disk space available. For example, photons whose directions make them very unlikely to reach the detectors are not saved in the GRH file, even if they were carefully tracked by the simulation programs. Furthermore, for most PET systems, there are always more singles events than coincident events. Most of the parameters used to evaluate the performance of a scanner are based on coincident detection. Thus, only one tenth of the singles photons are stored in the GRH files produce by the PHANTOM program to increase the storage efficiency.

Nevertheless, billions of coincidences are required to reconstruct real scanner images. Much more storage space, computer speed or simulation efficiency are required to generate enough data to reconstruct into simulated PET images that look like real scanners' images. However, by using cylindrical objects or geometrical symmetries or by forcing the photons to go in a determined direction, satisfactory results (such as energy spectrum analysis, sensitivity to true coincidences, scattered coincidences and singles events as well as the effect of these parameters on detector dead time) can be obtained. Solutions to further improve the efficiency of Monte Carlo simulations will be discussed in the next chapter.

## 2.4 PETSIM's accuracy

When this work started, the PETSIM programs did include positron range and non-collinearity of the photons. Also there was a realistic Compton scattering probability distribution for free electron derived from the Klein-Nishina relationship (refer to Section 1.3). Nevertheless, its photoelectric absorption model needed improvement.

In fact, bismuth germanate (BGO or  $\text{Bi}_4\text{Ge}_3\text{O}_{12}$ ) is nowadays the most commonly used detector material. The high atomic number of bismuth ( $Z = 83$ ) gives BGO a photoelectric K-shell absorption edge energy peak of about 95 keV, which is within the energy of interest in PET. However, this peak is not considered in Equation ? used in PETSIM to model the photoelectric attenuation coefficient. Because of its relatively high K-shell binding energy, the K-shell absorption energy peaks now need to be taken into account in Monte Carlo simulation.

Another problem that arose when using PETSIM is there were only few materials that could characterize the attenuation geometry of the system. They were: air, water, aluminum, BGO, foam, lead and tungsten. A longer list of materials would be more realistic to simulate today's phantoms and scanners. Moreover, PETSIM required that "magic" parameters (in the sense that they seem to come from nowhere) corresponding to the Compton scattering and photoelectric absorption coefficients need to be entered by the user to specify the attenuation media. Instead, specifying materials by name would make the programs more user friendly. These solutions are discussed in the next chapter.

# Improvements in Monte Carlo Simulation

---

### 3.1 Introduction

In the previous chapter, the inefficiency of Monte Carlo simulation of PET scanners as well as the need of a better accuracy from the PETSIM programs were mentioned. This chapter treats in detail the modifications that were implemented in the PETSIM programs during the author's research to solve most of the problems mentioned earlier. Section 3.2 deals with the improvement towards a better accuracy of the PETSIM programs. This is treated first since it is the easiest to implement and validate. Section 3.3 presents techniques to improve the efficiency of PET Monte Carlo simulations. It first deals with techniques found in the literature before suggesting a new technique which is called "recycling".

### 3.2 PETSIM's accuracy

To simulate the Compton scattering, PETSIM needs the energy of the photon and the electron density of the surrounding medium. To simulate the photoelectric effect, PETSIM needs parameters defining the photoelectric absorption partial interaction linear attenuation coefficient as a function of the photon energy. The original version came with a list of only 7 materials and 3 parameters for each of them: the electron density, and two parameters corresponding to the fitting of the photoelectric absorption partial interaction



linear attenuation coefficients (see Equation ?). Furthermore, the K-shell absorption peak could not be described by the two photoelectric absorption parameters and Equation ?.

The PETSIM simulation program was first improved by a more appropriate description and a longer list of the attenuation materials which could be used in the simulations. This was achieved with a commercially available program called XGAM [46], which runs on an IBM compatible PC. This program calculates the Compton scattering and photoelectric absorption cross sections for user-specified energies from databases constructed from references [47] for Compton scattering and from reference [48] the photoelectric absorption for user-specified compounds or mixtures. The Compton scattering cross sections are obtained from a combination of the Klein-Nishina Formula and non-relativistic Hartree-Fock incoherent scattering functions. Radiative and double Compton scattering corrections are also included. The photoelectric cross sections are obtained by phase-shift calculation for a central potential and the Hartree-Slater atomic model. The program can generate an output file containing the cross sections on the user-selected energy grid. That output file also contains the weighting factors, that is the fraction by weight of the constituents. They are calculated from the chemical formula entered by the user. For mixture, the user must supply the fractions by weight of the various components.

To implement the material description improvements to PETSIM, the density and the composition of several materials that may be present in the phantom, the collimator or the detector of a PET scanners were determined using references [9,49,50,51,52,53, 54,55]. For these materials, XGAM was used to output a table which contains the weighting factor of each elements in the material entered and the Compton scattering and photoelectric

absorption cross sections by steps of 5 keV from 15 keV to 511.1 keV. A program called ATTNPARAM was written to use these output tables to compute six parameters (instead of three) for each material which completely describe the attenuation properties of the materials. These six parameters are described in the following sub-sections. For each material, these six parameter were transcribed besides the material name on a look-up table.

The look-up table is a simple text (ASCII) file that can be read by every PETSIM program. It contains information which allows the PETSIM programs to calculate the Compton scattering and photoelectric absorption partial interaction linear attenuation coefficients needed for the different photon energies encounter during the simulation (between 15 keV and 511.1 keV). The user does not have to enter the attenuation parameter in the simulation batch file but only the name of the attenuation material. The simulation program will open the look-up table and will look for the attenuation parameters corresponding to the materials the user requested. The use of the six parameters which define the attenuation properties of the materials and the computation of the different partial interaction linear attenuation coefficients in the PETSIM programs are described below.

#### *A. Compton scattering: first parameter in look-up table*

PETSIM uses the equal-probability group concept (refer to Section 1.4b) to compute a random scattering angle. This scattering angle depends on the incident photon energy but does not dependent on the attenuation properties of the surrounding medium. This can be seen from Equation (1.11).

However, PETSIM uses Equations (1.12) to compute the Compton partial interaction linear attenuation coefficient. Besides the incident photon energy, this relationship requires that the electron density of the surrounding medium is known. The electron density constitutes the first of the six parameters used to define the attenuation properties of each material included in the look-up table. This parameter is also the only one needed to evaluate the Compton partial interaction linear attenuation coefficient of every material of the look-up table. The five others are used to compute the photoelectric partial interaction linear attenuation coefficient as it will be described in the following sub-sections. The electron density  $\rho_e$  [electrons/cm<sup>3</sup>] of a material is computed by the ATTNPARAM program using the relationship

$$\rho_e = \rho \cdot N_a \sum_{i=1}^N \frac{Z_i W_i}{A_i} \quad (3.1)$$

where,  $\rho$  is the density of the material [g/cm<sup>3</sup>],  $N_a$  is Avogadro's number ( $6.0221367 \times 10^{23}$  mol<sup>-1</sup>),  $N$  is the total number of elements composing the material and  $Z_i$ ,  $W_i$  and  $A_i$  are the atomic number, the weight fraction (in percent) and the atomic weight (in g/mol) respectively of the  $i^{th}$  element composing the material. The atomic numbers, the weight fraction and the total number of elements composing the material are obtained from the XGAM output table corresponding to the materials under investigation. ATTNPARAM includes an array of the atomic weight of each element between  $Z=1$  up to  $Z=100$  obtained from the data in reference [50]. During the execution of ATTNPARAM the user is asked to enter the density

of the materials under investigation to compute their electron density. Densities can be directly measured or can be obtained from the previous references.

***B. Photoelectric absorption: last five parameters in look-up table***

The other five parameters of the six stored in the look-up table are used to describe the photoelectric partial interaction linear attenuation coefficients. One of those parameters corresponds to the highest K-shell absorption edge energy of the material. It is computed by the ATTNPARAM program by scanning the photoelectric cross section for the energies stored in the XGAM output table (between 15 keV and 511.1 keV, by steps of 5 keV) corresponding to the material under investigation. The cross sections are then multiplied by the density of the material to obtain data points on a graph of the photoelectric partial interaction linear attenuation coefficients against the tabulated energies of the incident photon. Two curves, one above and one below the K-shell absorption edge energy, are computed to fit the data points. These curves are shown in Figure 3.1.

On each side of the K-shell absorption edge energy the photoelectric partial interaction linear attenuation coefficients can be approximated by curves similar to Equation ?. Thus, in the ATTNPARAM program, a linear log-log fitting (see Appendix B, page 115) of this family of curves through the data points on each side of the absorption edge computes the remaining four parameters of each material included in the look-up table. These parameters correspond to the behaviour of the photoelectric partial interaction linear attenuation coefficients  $\tau$  [ $\text{cm}^{-1}$ ] of each material and are used in the PETSIM program such that:

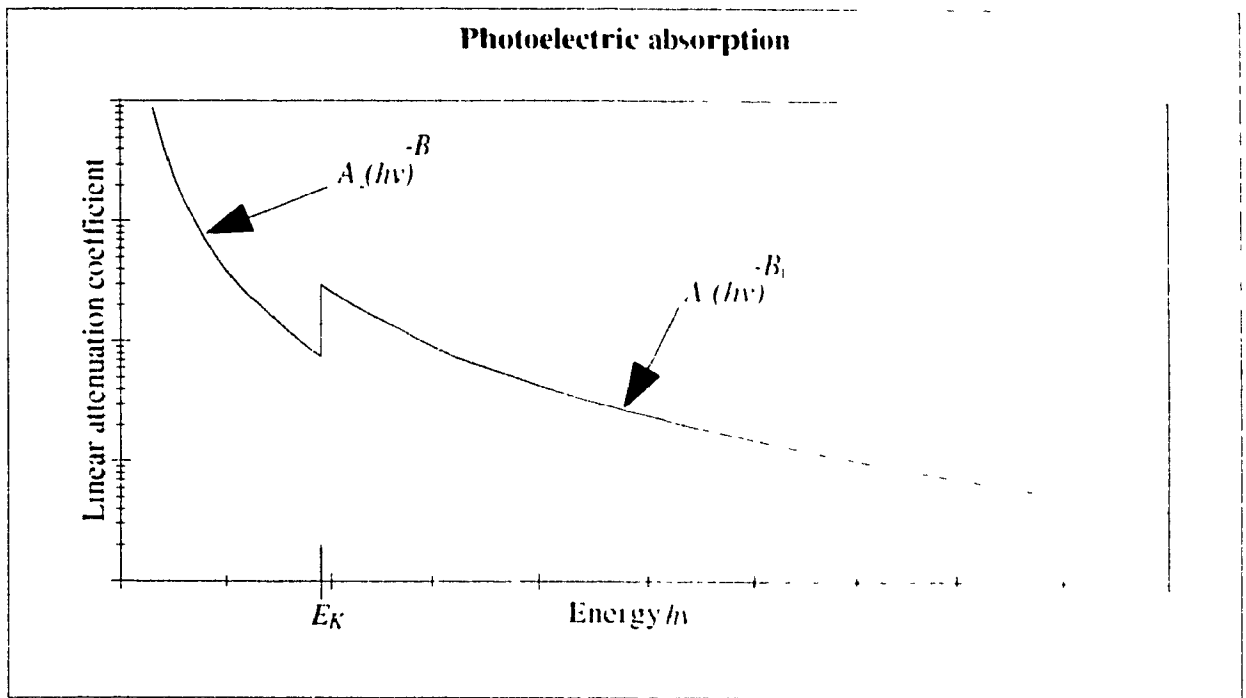


**Figure 3.1** The two curves, one below and one above the K-shell absorption edge energy, which completely describe the photoelectric absorption partial interaction linear attenuation coefficient.

$$\tau[\text{cm}^{-1}] = \begin{cases} A_1 (h\nu[\text{keV}])^{-B_1} & h\nu \geq E_K \\ A_2 (h\nu[\text{keV}])^{-B_2} & h\nu < E_K \end{cases} \quad (3.2)$$

where  $h\nu$  is the energy of the incident photon [keV],  $E_K$  is the energy of the highest K-shell absorption edge of the material [keV] (second parameter of the look-up table).  $A_1$ ,  $A_2$ ,  $B_1$  and  $B_2$  are empirical parameters. They constitute the four remaining parameters of every material. So, at most two curves, or five parameters, are necessary to completely describe the photoelectric partial interaction linear attenuation coefficient in the energy range of PET since, for any material, the L- M- and N-shell absorption energies are always lower than 15 keV. If the K-shell absorption energy of the material under investigation is lower than 15

keV, there is no K-edge energy peak in the photoelectric partial interaction coefficient tabulated. Thus only one curve is necessary to fit the data. The parameters  $A_2$  and  $B_2$  are then not required.

### 3.3 Monte Carlo simulation efficiency of PET scanners

As the reader could conclude from the Section 2.2, conventional Monte Carlo simulations are computationally inefficient. Only a few percent of the photons generated and tracked will actually be detected. This is due to the size and geometry of the detector array itself and the collimation of the photons in a MS-PET scanner. A more efficient use of the resources available today (such as disk storage space and computer speed) will automatically lead to an improvement in statistical precision of Monte Carlo simulation of PET scanner.

#### *A. Improving the efficiency using variance reduction techniques*

To improve the efficiency of Monte Carlo simulation of PET systems, a group at the University of Washington [23] recently developed a method using variance reduction techniques [45]. The method consists in increasing the "yield" of detected photons. Their Monte Carlo simulation program can use some or both of these two variance reduction techniques which they call "stratification" and "forced detection". In their simulation program, the photons are not tracked randomly as they occur in reality but in ways chosen to increase the frequency of detected events. Bias is avoided by giving each simulated photon a weight that indicates how many real photons it represents.

In stratification, the starting location and direction of the generated photons are sampled unevenly. Stratification cells are defined with two variables: the axial slice in which the photon production occurs and the angle of emission about the axis of the tomograph. The simulation begins with a very short conventional Monte Carlo simulation to compute a productivity function for each stratification cell, i.e. the probability that a photon starting at the stratification cell location and having the stratification cell direction will be detected. Then, an initial number of starting events per stratification cell is chosen so the expected weight at detection of each simulated photon is a constant, to make the final set of weights as uniform as possible. If the spread in weights is large, the apparent gain in the precision of the results may be illusory. To reduce the spread, the starting weight of a simulated photon starting in a given stratification cell is chosen to be the ratio between the expected number of photons that would be produced in the same cell in a real experiment or a conventional Monte Carlo simulation and the chosen number of starts for the same cell to make the expected weights at detection a constant.

With forced detection, a user-defined "critical zone" is first defined. The critical zone usually looks like a cylinder with cone-shaped dents at the top and bottom and having a radius equal to the inner radius of the detector. The scanner's FOV is nested within the critical zone. The photons which originate or scatter in the critical zone are forced to hit the detectors. Thus, photoelectric absorption is not allowed. Bias is avoided by changing the weight of the photon to reflect the probability of the interactions that were forced. The procedure is done as follows. The generated photon is first checked if it is going towards the inner radius of the detector without scattering. If it is, a copy of the

photon is projected unscattered to the detector inner radius. The copy is recorded as detected photon with its weight reduced to account for the possibility of scattering or absorption along its path. The generated photon is then tracked in the conventional manner except that photoelectric absorption is not allowed. The photon weight is lowered at each interaction point to reflect the possibility of photoelectric absorption or scattering at another angle. The generated photon is tracked until it escapes the critical zone or its energy drops below a user-defined minimum. At this stage, the generated photon is discarded, even if it was going toward the detector ring.

During the tracking, a procedure is used to keep the photon weights within a weight window. A copy of the photon, including its current weight, is also made at each interaction point. Each copy is then forced to scatter towards the inner radius of the detector ring. Their weights are reduced to reflect the probability of the forced interaction. Each copy is then projected to the inner radius of the detector ring. Their weights are reduced another time to account for the possibility of scattering or absorption between the forced interaction point and the inner radius of the detector ring. Each copy is recorded as detected photon. In the final phase of the simulation, each detected photon is tracked in the conventional manner within the detector ring.

Simulation programs which use variance reduction techniques compute the flux through various detectors by counting the photons which hit the detectors and adding up their weight. This flux is still a random variable but is no longer a Poisson one. In conventional methods, all particle weights are the same and thus follow Poisson statistics. Implementing



this technique in PETSIM is possible, but requires major modifications to the programs. Most of the modifications must be done in the PHANTOM program. They are related to:

- (i) the weight of the photons, not used in conventional simulations,
- (ii) the fact that the photon can not be absorbed photoelectrically in the critical zone in conventional Monte Carlo simulations and
- (iii) to the fact that for each interaction point within the critical zone, the photon has to be forced to scatter towards the collimator inner radius.

The compact GRH file format actually used would also have to be modified to store the weight factor for each photon stored in the file. However, it was considered desirable to implement in PETSIM a technique which is easy to implement and improves the efficiency of conventional Monte Carlo simulation and, above all, still produce data which follow Poisson statistics. To achieve this goal, a new technique called recycling was implemented in the PETSIM programs. It is described in the next sub-section.

### ***B. Improving the efficiency using recycling***

As mentioned earlier, PETSIM uses independent programs such as the PHANTOM program, the COLLIMATOR program and the DETECTOR program to simulate the source/phantom phase, the collimation phase and the detection phase of the simulation respectively. The processes are linked together with intermediate GRH files stored on a disk or a tape: the GRH file produced during the source/phantom phase is retrieved by the COLLIMATOR program, as is the GRH file produced during the collimation phase by the DETECTOR program. When PETSIM simulates the collimator or

the detection phase of the simulation, the random number generator's last seed from the previous phase (source/phantom or collimator) is read from the GRH file. This seed is retrieved to prime the random number generator of the current phase. The seed allows the random number generator to continue generating its sequence of random number from where it stopped in the previous phase. Each photon stored in the GRH file is read by the programs, is tracked using the random number generated and is stored in the output GRH file or discarded.

The author included into the PETSIM simulation programs a technique which takes advantage of the intermediate GRH files to increase the number of photons input in the phases which retrieve an intermediate GRH file. In the collimator and the detection phases, once the intermediate GRH file is read, the programs reuse the file by going back to the start of the file and read the so called original photons (i.e. the photons stored in the intermediate GRH file) a second time or more if needed. By reusing the original photons without resetting the random number generator, new tracks for the photons through the current phase are generated in the second and later times the photons are reused. The random number sequence being different, a new track is generated, even if the original photon has the same initial parameters as when it was read the first time. Nevertheless this technique is more efficient if care is taken to avoid having, for the original photons which are reused, exactly the same initial parameters as the original photon. The procedure for this is described below. Simulations using this procedure are faster overall than conventional Monte Carlo simulations. This is partly because the creation, annihilation and tracking processes in the source/phantom phase of the simulation take longer than tracking the photons in the other

phases of the simulation and mostly because so many photons are lost in the source/phantom phase of the simulation compared to the other phases of the simulation.

Most phantoms used to test PET systems extend beyond the active volume (FOV) of the imaging device in the axial ( $z$ -axis) direction. This geometrical property of the phantoms can be included with the reuse of the original photons from the intermediate GRH file retrieved by the COLLIMATOR program by moving the phantom in and out in the axial direction by a random displacement each time an original single photon or a pair of annihilation photons is reused. The random displacement can be anything but it must be kept small enough to allow the phantom to always cover the full FOV in the axial direction. Usually, a displacement corresponding to a random fraction of the slice width is chosen. This is implemented in the COLLIMATOR program by moving the  $z$ -axis origin coordinate of the original photon as well as its  $z$ -axis position coordinate at the inner edge of the collimator by a random displacement each time the original photon is reused. The photon is then tracked as usual through the collimator. This procedure is called *recycling*. The flow chart of recycling for the collimation phase of the simulation is shown in Figure 3.2. The grey-shaded boxes represent the COLLIMATOR program's original procedures. The white boxes represent the procedure that were added to the COLLIMATOR program to allow it to recycle the original photons. Recycling gives the photons which were stopped by the collimator septa another chance to get through the collimator and be recorded in the GRH file. Figure 3.3(a) shows an example of an original photon track retrieved by the COLLIMATOR program. Its current position is at the inner radius of the collimator ring.

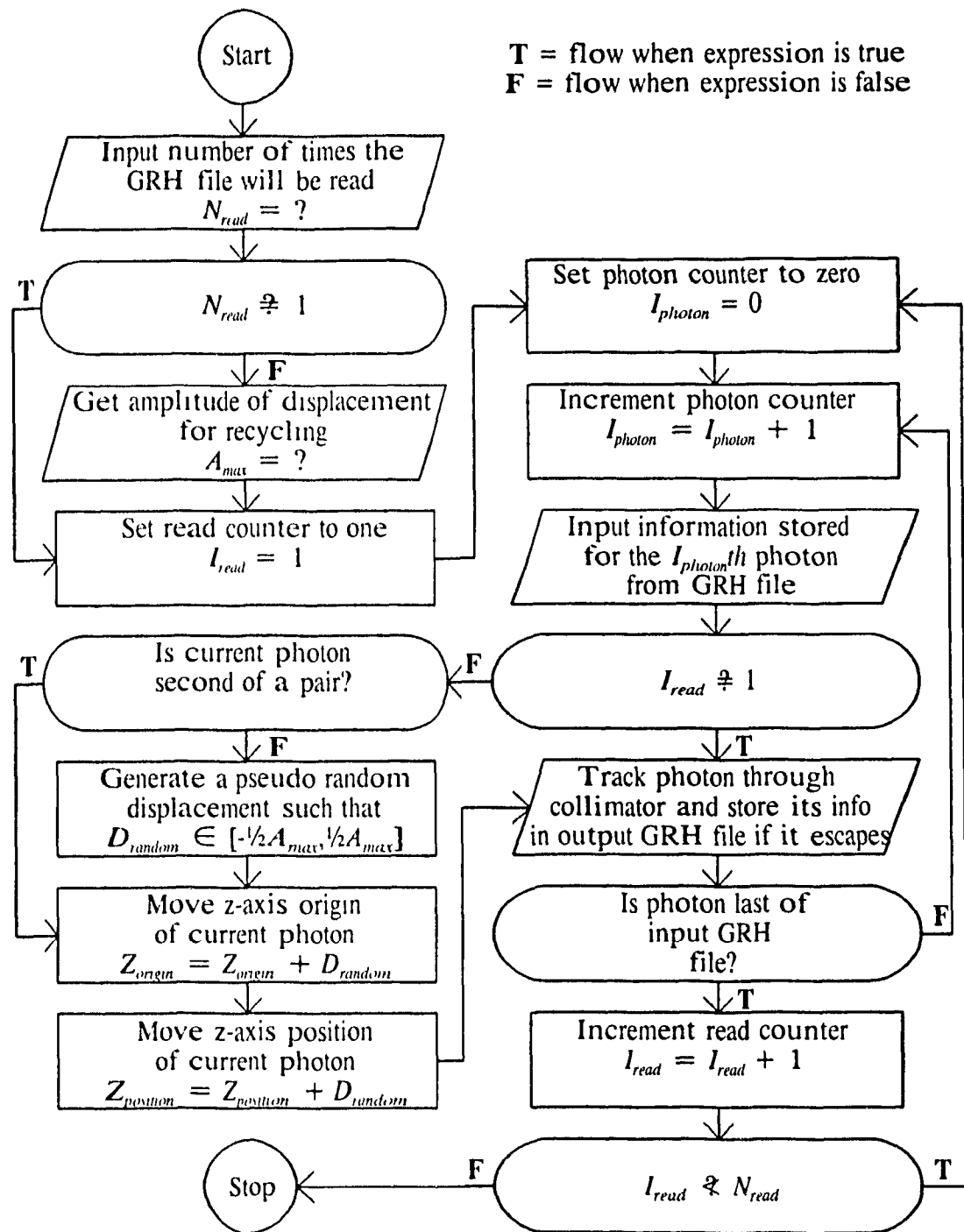
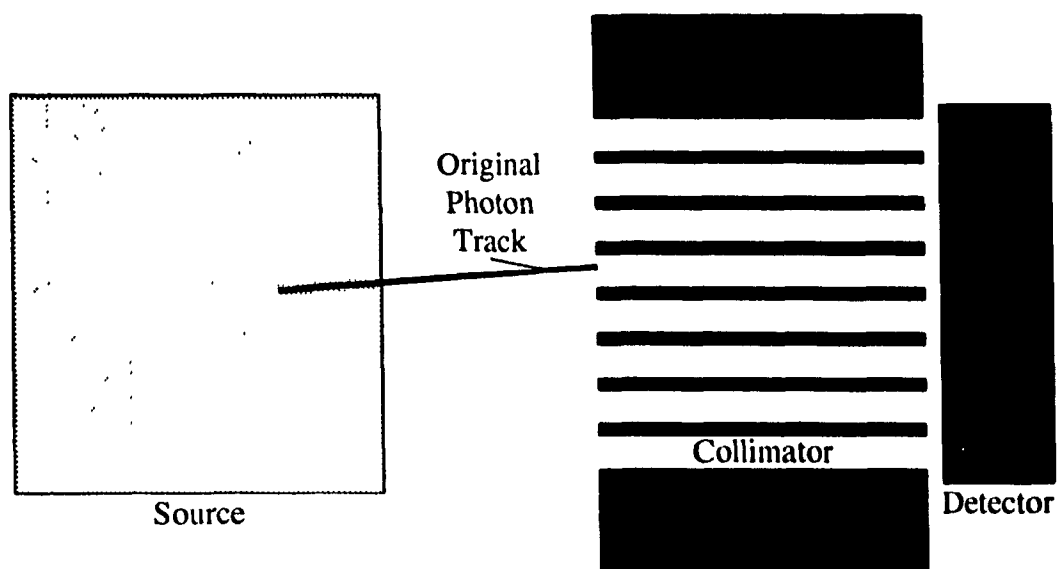
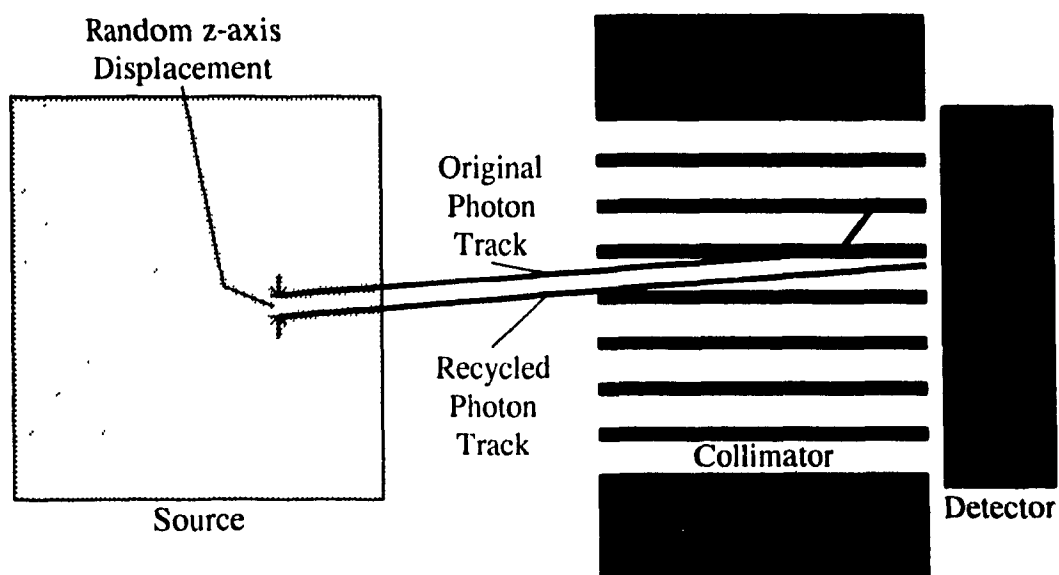


**Figure 3.2** Flow chart of recycling in the collimation phase of the simulation.



(a)

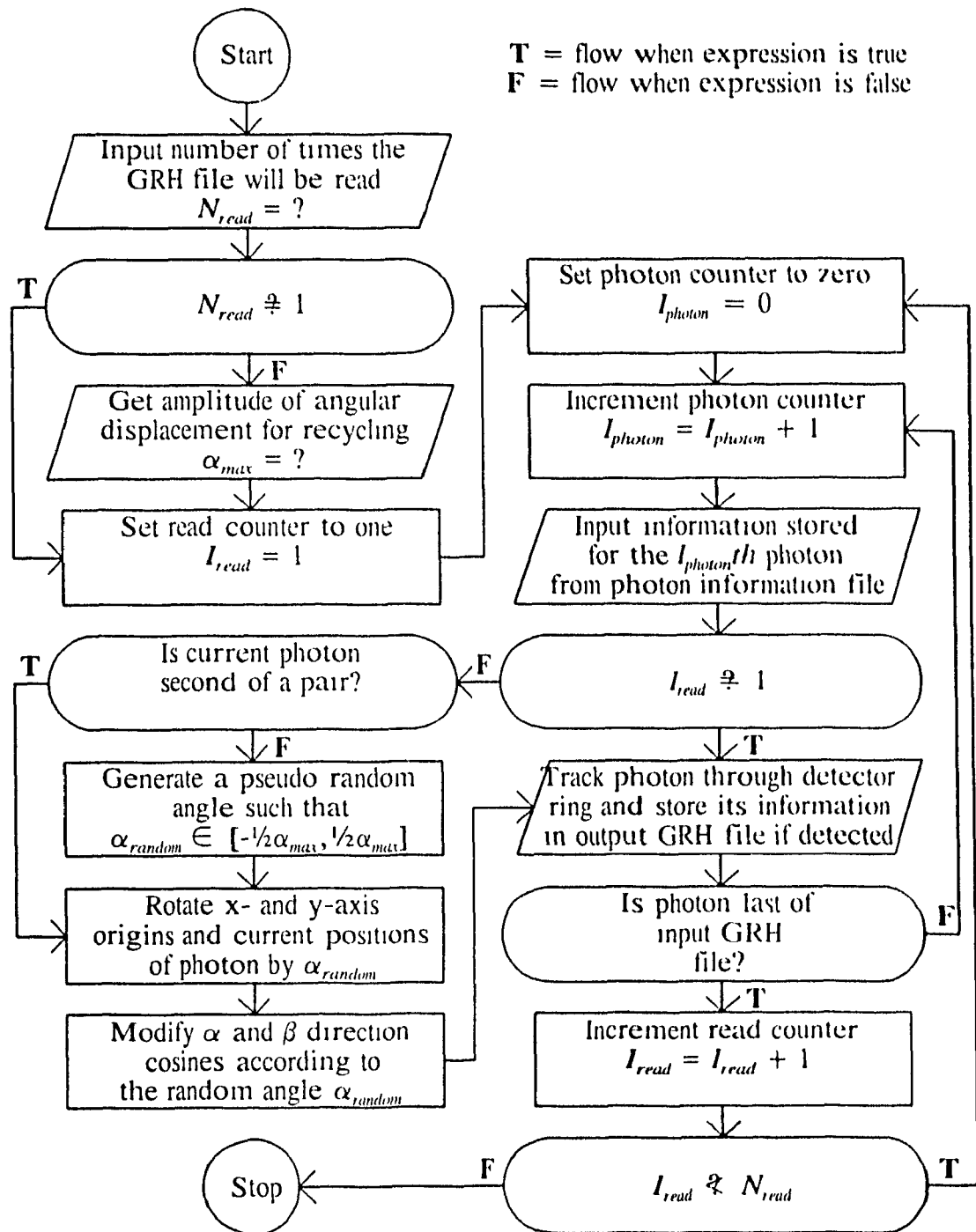


(b)

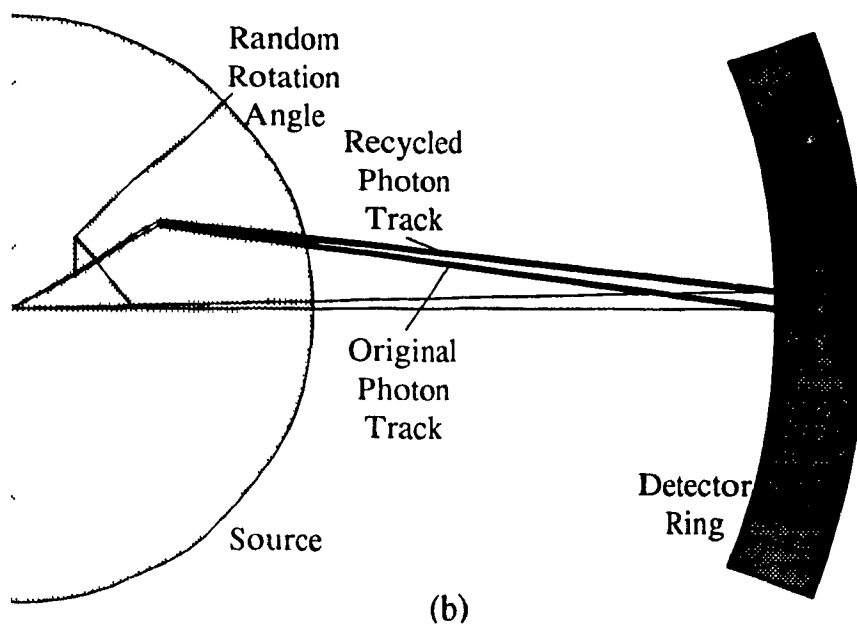
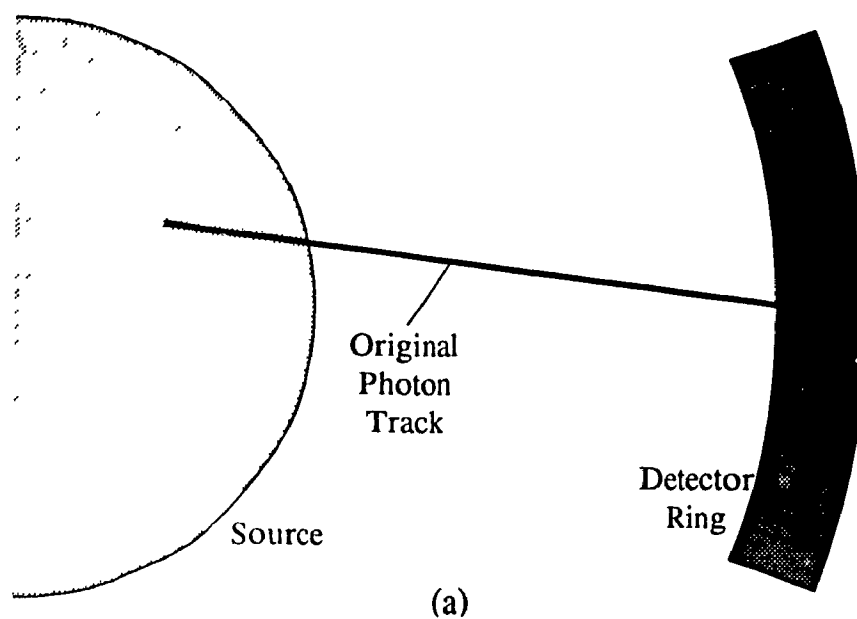
**Figure 3.3** (a) Original photon track after source/phantom phase. (b) Recycling in collimation phase showing the effect of the random axial displacement on the original photon track.

Figure 3.3(b) shows an example of the effect of recycling on this original photon track. In the COLLIMATOR program, the original photon is tracked and is lost in the collimator. The recycled photon, that is the original photon moved by a random displacement in the axial direction, is tracked and finds its way to the detector ring.

Recycling can also be used by the DETECTOR program. Indeed, most phantoms used to test PET systems are circularly symmetric. The collimators are also circularly symmetric. These geometric characteristics can be included with the reuse of the original photons from the intermediate GRH file retrieved by the DETECTOR program by rotating the phantom by a random angle each time an original single photon or a pair of annihilation photons is reused. The random angle is usually set to a random fraction of the detector block to block angular separation. This is implemented by rotating the original photon track by the random angle in the  $xy$ -plane, that is by rotating the  $x$ - and  $y$ -axis origin coordinates as well as the  $x$ - and  $y$ -axis position coordinates of the original photon by the random angle. This random angle is also added to the original photons direction in the  $xy$ -plane. ( $\alpha$  and  $\theta$  in Table 1.2). The photon is then tracked as usual through the detector. The flow chart of recycling for the detection phase of the simulation is shown in Figure 3.4. The white boxes represent the procedure that were added to the DETECTOR program to allow it to recycle the original photons. Recycling gives the photons which were absorbed in the septa or escape the detectors another chance to be detected. Figure 3.5(a) shows an example of an original photon track retrieved by the DETECTOR program. Its current position is at the inner radius of the detector ring. Figure 3.5(b) shows an example of the effect of recycling on this original photon. In the DETECTOR program, the original photon



**Figure 3.4** Flow chart of recycling in the detection phase of the simulation.



**Figure 3.5** (a) Original photon track after collimation phase. (b) Recycling in detection phase showing the effect of the random rotation on the original photon track.



is tracked and is lost in the septa. The recycled photon, that is the original photon rotated by a random angle in the  $xy$ -plane, is tracked and is detected.

To resume, recycling consists in moving the original photons by random displacements in the axial direction or by random angles in the  $xy$ -plane the later times the original photons are reused. Notice that the random offsets are not used the first time the original photons are read (see the flow charts in Figure 3.2 and Figure 3.4). In all cases the tracking of the photons is done with the Monte Carlo conventional manner. In practice when the GRH file is read from disk, recycling is done by resetting the file block pointer to 1 when it points the end of file (EOF) mark. If the file is on tape, the tape is rewound and then advanced over the header block which described the file.

Recycling should improve the precision of the simulation without requiring larger GRH files from the source/phantom phase thus increasing the storage efficiency. Recycling should also reduce the simulation time since fewer positron annihilations are needed to achieved a given statistical precision of the complete simulation. Its validation is the main topic of the two next chapters.

# Methodology to Validate the Improvements

---

### 4.1 Introduction

The main concern when using the recycling technique is that the data still follows Poisson statistics. One way to verify this is to repeat the same simulation using the same recycling procedure a large number of times with different sets of random numbers and compute the distribution frequency of the results. If the distribution of the results is a Poisson distribution, the simulation follows Poisson statistics. However, this approach is extremely long to accomplish and is often not computationally feasible.

Another approach is to compare the simulated results with the results obtained with a real scanner. This is usually an unsatisfactory approach since some information such as the real position creation and annihilation locations in the source, the photons' interaction locations and the number of scattered events detected are impossible to determine in "real life". This approach is also subject to experimental uncertainties.

Another possibility is to compare the results of the Monte Carlo simulation with theoretical or analytical results. Assuming that the analytical results correspond to the means of a large number of similar simulations, the simulation results could be compared to the analytical ones to see if they are within a confidence interval of the theoretical distribution of the results about the means. However, the analytical results are very often very complex to compute since a very large number of parameters have to be taken into account. This is in fact the reason why Monte Carlo simulation is usually used instead of

theoretical means to compute the performance of a PET scanner. Nevertheless, this approach was chosen to validate the improvement in efficiency of the recycling technique.

In preparing a previous paper about recycling [35], the authors realised that it was not so obvious to compute analytical results for a PET system [56,57,58]. The validation of recycling as an efficiency improvement in Monte Carlo simulation of PET systems was done by fitting a third-degree polynomial by the least-squares method through the coincident spectrum of each simulation, from 180 keV to 480 keV. The authors assumed then that the theoretical coincident spectrum in this region was smooth and could be represented by a third-degree polynomial. In fact, the exact theoretical shape was (and still is) unknown. So, if recycling the photons from a constant number of annihilations was reducing the least-squares value, it meant that new coincident events were detected, thus improving the efficiency of the simulation. But, this approach was not quantifying the efficiency improvements. It was also probably not convincing since one can argue that anything can be fit with a third-degree polynomial.

In this work, efforts were made to compute a verifiable analytical result. The mean projection of any simulated scanner was chosen as something which could be analytically computed. The mean projection being a display of the counting of all the coincidence events detected for all detector pairs in a PET system, it was probably the most obvious way to analyze the efficiency improvement of recycling and ensure that the generated photons were following Poisson statistics. The simulated mean projections could then be compared to the analytical one to validate the simulations which were using the recycling technique.

This chapter treats in detail the methodology used to validate the efficiency improvement due to the recycling technique. Section 4.2 explains the construction of an analytical mean projection. Section 4.3 deals with the superposition of the mean projection. Section 4.4 discusses how the projections were compared to quantify the efficiency.

The validation of the improvements related to the accuracy of PETSIM do not need to be as complicated as the validation of recycling; the attenuation coefficients computed by the PETSIM program from the parameters of the new look-up table could simply be compared to the output attenuation coefficients of the XGAM program. As the reader will see in the next chapter, this approach confirms the accuracy improvements but it assumes that the authors of XGAM made experimental measurements to ensure that their databases were accurate.

## **4.2 Building an Analytical Mean Projection**

This section elaborates the equations used to build an analytical mean projection of a simulated PET system. A projection is a profile through the object been scanned as sampled by parallel coincident detector or crystal pairs. Each bin of the projection contains the number of either true, scattered or random coincidences detected for the corresponding crystal pair. The mean projection represents the average of all possible projections around the detector ring. It is useful for circularly symmetric objects where statistics of the simulation can be improved. As opposed to real life, simulated events detected are known to be either true, scattered or random coincidences. To simplify the

procedure to obtain an analytical mean projection, only the true coincidences were used to build the analytical mean projection.

The relationship to obtain the true coincidence rate for a given pair of detector crystals for a phantom being scanned within a particular PET scanner is very complex and probably impossible to establish without simplification. If an annihilation pair of photons is detected in two different crystals of the scanner, the paths followed by the two photons is not necessarily along the line joining the centre of the coincident crystal, as it is assumed in most PET scanners, nor along the line joining both centroids of interaction within the crystals. It is in fact something far more complex. The reasons are the following:

- (i) The positron produced by the  $\beta^+$ -emitter travels a short distance before having an annihilation with an electron to produce two 511.1 keV photons. The position of the annihilation may happen to be on the straight line joining the two coincident crystals but not the position of the positron creation.
- (ii) Because of the residual energy of the positron and/or the free electron, the path of the pair of annihilation photons are not collinear. The annihilation position can not possibly be on the straight line joining the two coincident crystals.
- (iii) The photon entering a crystal very often undergoes more than one interaction (Compton scattering and photoelectric absorption) within the crystal. These interaction locations are impossible to detect in a real scanner; one can only tell in which crystals the interactions occur. In PETSIM, the resulting point of interaction is computed as an average of all the points of interactions within

a crystal weighted by the energy deposited at each point of interaction. If the unscattered incident photon undergoes photoelectric absorption, all the energy is deposited at the first interaction point. For that condition only, the average interaction is collinear with the position where the annihilation took place and the point where the photon entered the crystal. But, since Compton scattering in the detectors produces a resulting photon which direction is at a certain angle with the incident photon, it is unlikely that the average point of interaction will be collinear with the annihilation position and the point where the unscattered photon entered the crystal.

The true coincidence rate relationship for a pair of detector has to include these effects if it is written for a given isotope distribution in real life, assuming that one knows the distribution. This is certainly not the case when a subject is imaged otherwise one would not need to image him.

Monte Carlo simulation is more flexible than real life: the complete history of a particle can be known. The source activity distribution is also well known since it is user-defined. Thus, several assumptions could be made to simplify the true coincidence rate relationship to compare it with data obtained from Monte Carlo simulations (as opposed to real scanners). For example, the true coincidence rate relationship could be simplified to a sum of line integrations if simulations were run so that:

- (i) the positron range was negligible; the point of annihilation was almost the same as the position of the isotope that produced the positron.

- (ii) the non-collinearity of the photon pair was negligible; the annihilation occurred on a line joining the points where the photons entered the crystals.
- (iii) only the photons that had one 511.1 keV photoelectric interaction within the crystals were counted.

Points (i) and (ii) produced a coincidence rate for a crystal pair that was only slightly different from the one obtained experimentally. Point (iii) is virtually impossible to compare experimentally since the energy resolution of a scanner is poor (at best a FWHM of 10% for NaI(Tl) crystals). Another reason is that a real scanner does not record the number of interactions within a crystal. However, it was unimportant then to know the experimental results since the objective was only to compare the coincidence rate of simulations of a PET scanner with analytical results. Since PETSIM can disable the positron range and the non-collinearity of the photon pair points (i) and (ii) could be respected. For point (iii) the previous versions of PETSIM were computing and storing within the DETECTOR GRH file the centroid of interactions and the energy deposited in the detectors for each photon interacting with them. Some modifications were made by the author to also record the number of interactions which occurred within a crystal (see Table 1.2, page 17). The three previous assumptions could then be made to simplify the coincidence rate relationship and still quantify accurately the simulation efficiency.

Some geometrical characteristic was also included to simplify the coincidence rate relationship for a pair of crystals. They were the following:

- (i) Use of a simple cylindrical water flood phantom that extend beyond the axial FOV of the scanner. This made the phantom circularly symmetric and

removed the angular dependence of the relationship, at least up to the block-based detector ring. This also removes the axial dependence of the relationship.

- (ii) Count for direct slices only. This was done to avoid computing the attenuations in the collimator septa for the cross slices.

With all the previous simplifications, the coincidence rate relationship for a pair of simulated crystals imaging a simple cylindrical water flood phantom could be approximated by a line integral along a straight line. The relationship was nevertheless:

$$\dot{N}(c) = N_s N_b \frac{a}{4\pi} \sum_{i_c=1}^{N_c} \int_{r=r_{min}(i_c)}^{r_{max}(i_c)} \int_{\phi=\phi_{min}(r)}^{\pi-\phi_{min}(r)} \left( z_s - 2\sqrt{R_{in}^2 - r^2} \cot \phi \right) L(r, \phi) A_{med}(r, \phi) A_{col}(r, \phi) \cdot \int_{\theta=-\theta_{max}(r)}^{\theta_{max}(r)} A_{det}(r, \phi, \theta) D(r, \phi, \theta) \sin \phi d\theta d\phi dr, \quad (4.1)$$

where  $\dot{N}$  is the coincidence rate in a pair of crystals separated by  $c$  crystals around the detector ring counting clockwise in a top view of the detector ring ( $c$  being the number of crystals over the shortest path between the two coincident crystals around the detector ring). In this equation,  $N_s$  is the number of superimposed direct slices.  $N_b$  is the number of detector blocks around the detector ring.  $a$  is the activity concentration of the water flood in Bq/cm<sup>3</sup>.  $N_c$  is the number of crystals per block in the transverse direction.  $i_c$  is the crystal number in the transverse direction for the detector block corresponding to the first coincident crystal counting clockwise ( $1 \leq i_c \leq N_c$ ).  $z_s$  is the slice thickness.  $R_{in}$  is the inner radius of the detector ring. The term in parenthesis is simply to avoid an integration in the



axial direction (i.e. along the z-axis). This term can replace the integration in the axial direction because of the axial symmetry within a slice of the system.  $r$ ,  $\theta$  and  $\phi$  are variables used to define a line of integration. They are defined in Figure 4.1.  $r$  represents the z-axis offset (or offset from the centre of the FOV) of the line of integration.  $\theta$  is the angle between the projection of the line of integration and the x-axis on a transverse plane (xy-plane).  $\phi$  is the angle between the line of integration and a line parallel to the z-axis.

In Equation (4.1), the x-axis is relative to the crystal separation. Equation (4.1) always forces the coincident crystal to be symmetrically disposed about the x-axis (see for example Figure 4.2). Thus, the x-axis is median and perpendicular to a line joining the two coincident crystals both being on a transverse cross section of the scanner. The origin of the x-axis is at the centre of the FOV.

In Equation (4.1),  $L$ ,  $A_{med}$ ,  $A_{col}$ ,  $A_{det}$  and  $D$  are functions representing the path length through the phantom ( $L$ ), the attenuation in the phantom medium ( $A_{med}$ ), in the collimator ( $A_{col}$ ) and in the detector ring ( $A_{det}$ ) and the detection of the photons in the coincident crystals ( $D$ ) along a line of integration. With the previous variable used to define a line of integration, the path length through the source is defined as the intersection between a line of interaction and the cylindrical source/phantom volume. Mathematically, that is:

$$L(r, \phi) = \begin{cases} \frac{2\sqrt{R_s^2 - r^2}}{\sin \phi}, & r < R_s \\ 0, & \text{Otherwise} \end{cases} \quad (4.2)$$

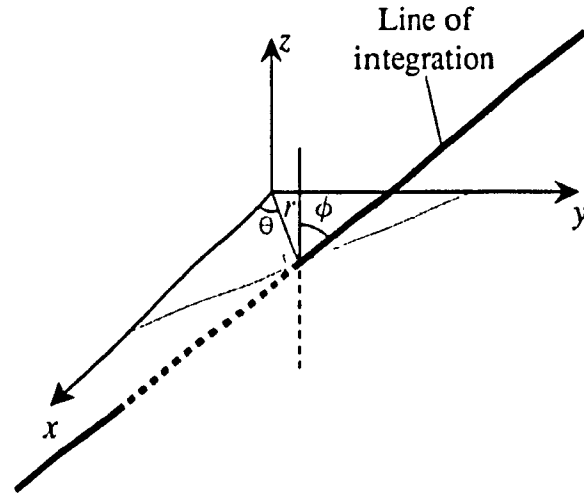


**Figure 4.1** Variables used to define a line of integration.

where  $R_s$  be the radius of the water flood. The attenuation in the phantom medium, is defined as:

$$A_{med}(r, \phi) = \exp(-\mu_{med}L(r, \phi)), \quad (4.3)$$

where  $\mu_{med}$  is the linear attenuation coefficient for the phantom medium at 511.1 keV.

The path length between two coincident crystals along a line of integration can be visualized as the intersection of the line of integration and a cylinder having a radius corresponding to the inner radius of the detector ring. The path length travelled in air by the photons on that line of integration is then the difference between the path length between the two coincident crystals and the path length through the phantom. So, mathematically, the attenuation in the collimator is:

$$A_{col}(r, \phi) = \exp\left(-\mu_{air}\left[\frac{2\sqrt{R_m^2 - r^2}}{\sin\phi} - L(r, \phi)\right]\right), \quad (4.4)$$

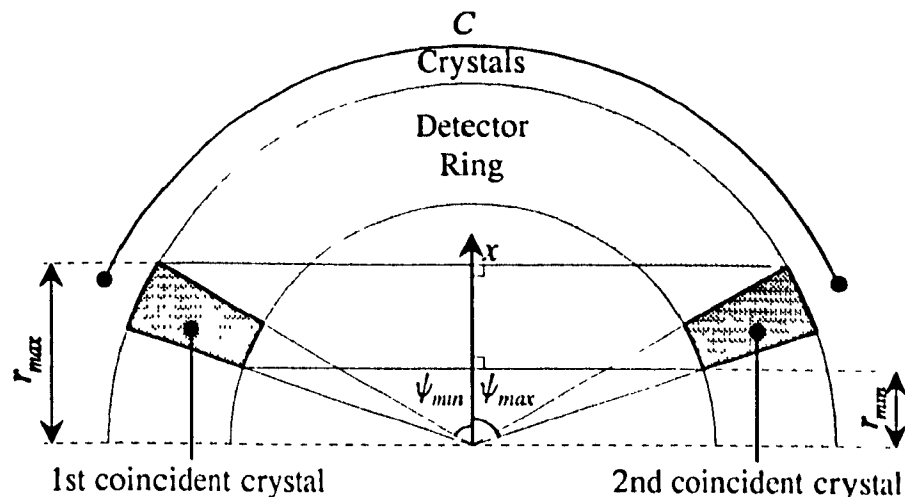


**Figure 4.2** Definitions of  $\psi_{min}$ ,  $\psi_{max}$ ,  $r_{min}$  and  $r_{max}$ .

where  $\mu_{air}$  is the linear attenuation coefficient for air at 511.1 keV.

In most new PET system, the detector ring is not simply a hollow cylinder having the attenuation characteristics and properties of the detector material. Most new PET scanners use detector blocks disposed all around the detector ring. Each block is composed of a matrix of crystals. Between each block, lead or tungsten septa are inserted in the detector ring to reduce the chance of Compton scatter from one block to the next. These also shield the outer crystals especially near the edges of the FOV to reduce radial blurring in the image. The analytical coincidence rate had to consider the attenuation within these septa when the line of integration crosses them. The boundary of the integrations in Equation (4.1) and the position of these septa depends on the relative position of the coincident crystals within the detector blocks. They also depends on the number of inter-block septa separating the coincident crystals. This number may vary by  $\pm 1$  for a given number of crystals separating the coincident crystals. Thus the equations to define the boundary of the integration of Equation (4.1) and the functions related to the detector ring

involve the use of integer functions to take the relative positions of the coincident crystals and the inter-block septa into account.

To define the functions related to the detector ring as well as the boundaries of the three integrations, other geometrical characteristics of the water flood phantom, the collimator and the detector ring were needed. Let  $R_{out}$  be the outer radius of the detector ring. Let  $f_d$  be the detector fraction around the ring, that is the ratio between the detector surface being on the inner surface of the detector ring and the total inner surface of the detector ring. The septum fraction  $f_s$  can then be defined as:

$$f_s = 1 - f_d, \quad (4.5)$$

and the crystal fraction,  $f_c$ , as:

$$f_c = \frac{f_d}{N_c}. \quad (4.6)$$

A variable  $\alpha$ , the sector angle (a sector being a detector block and a lead septum separating two detector blocks) was also defined. Thus  $\alpha$  was:

$$\alpha = \frac{2\pi}{N_b}. \quad (4.7)$$

If the two coincident crystals are separated by  $c$  crystals,  $n_s$ , the number of septa between the coincident crystals around the ring depends on  $i_c$  and is:

$$n_s = \text{int}\left(\frac{c + (i_c - 1)}{N_c}\right), \quad (4.8)$$

where "int" is a function which returns the largest integer smaller or equal to the value in parenthesis. To define the boundaries of integration,  $\psi_{min}$ , half the minimum opening angle for the two crystals can be computed using the relationship:

$$\psi_{min} = \frac{1}{2} \left( \left( c - \frac{1}{2} \right) f_c + n_s f_s \right) \alpha. \quad (4.9)$$

Similarly,  $\psi_{max}$ , half the maximum opening angle for the two coincident crystals is:

$$\psi_{max} = \psi_{min} + f_c \alpha. \quad (4.10)$$

A geometrical description of those variable is given in Figure 4.2.

We can now define the boundaries for the three integrations of Equation (4.1). The first boundary for the variable  $r$ ,  $r_{max}$ , corresponds to the distance between the  $x=0$  plane and the outermost line of integration crossing both coincident crystals, except if that distance is larger than the radius of the cylindrical flood phantom; then it has the value of this radius. The second boundary,  $r_{min}$ , corresponds to the distance between the  $x=0$  plane and the innermost line of integration crossing both coincident crystals unless the two coincident crystal are diametrically disposed; then it as the value of  $-r_{max}$ . Because of the previous definition of the  $x$ -axis, the innermost and outermost lines of integration are always parallel to the  $x=0$  plane. The reader is referred to Figure 4.2 for a geometrical definition of these boundaries. Mathematically, they are defined by:

$$r_{max} = \min(R_{out} \sin \psi_{min}, R_s), \quad (4.11)$$

where the function "min" returns the smallest value between the two in parenthesis and

$$r_{min} = \begin{cases} -r_{max}, & c = \frac{N_d N_c}{2} \\ R_{in} \sin \psi_{max}, & \text{Otherwise} \end{cases} \quad (4.12)$$

The boundaries for the variable  $\phi$  correspond to the angle made by a vertical line and a line joining the bottom of the slice at the first crystal position and the top of the slice at the second crystal position for a given offset from the centre of the scanner (variable  $r$ ). Mathematically, that can be expressed as:

$$\phi_{min}(r) = \tan^{-1} \left( \frac{2\sqrt{R_{in}^2 - r^2}}{z_s} \right). \quad (4.13)$$

The boundaries for the variable  $\theta$  correspond to the range of angles, in the transverse plane, a line of integration with an offset  $r$  can have such that the line of integration still crosses both coincident crystals. As illustrated in Figure 4.3, two cases are possible. In the first case (Figure 4.3a), the range of angles is limited by the closest point of the coincident crystals from the  $x=0$  plane. In the second case (Figure 4.3b), the range of angles is limited by the farthest point of the coincident crystals from the  $x=0$  plane. The limit between the two previous cases is when  $r$  is equal to  $h$ , the height of a triangle formed by the closest point of one of the coincident crystals from the  $x=0$  plane, the centre of the FOV and the farthest point of the other coincident crystal from the  $x=0$  plane. Using geometry rules for triangles (such as the sines' law) and Figure 4.4, one can find out that  $h$  is:

$$h = \frac{\sin(\psi_{min} + \psi_{max})}{\sqrt{\frac{1}{R_{in}^2} + \frac{1}{R_{out}^2} - \frac{2\cos(\psi_{min} + \psi_{max})}{R_{in}R_{out}}}}. \quad (4.14)$$

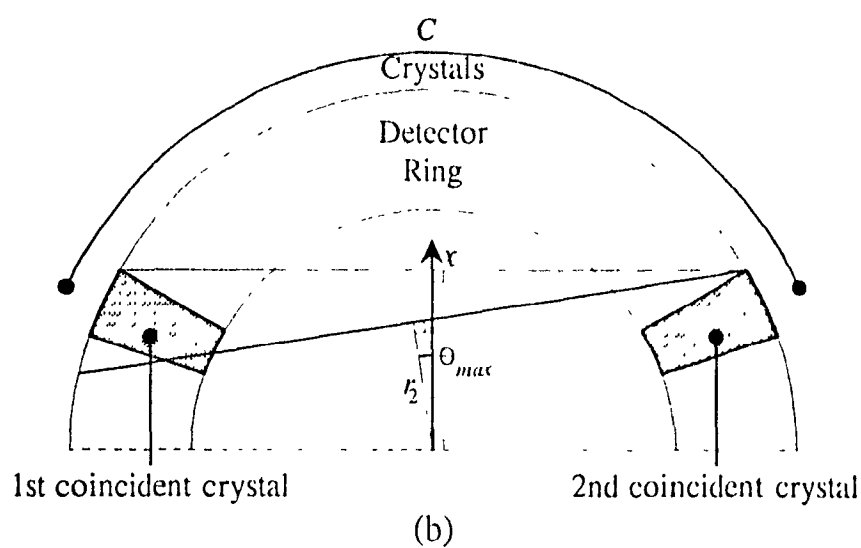
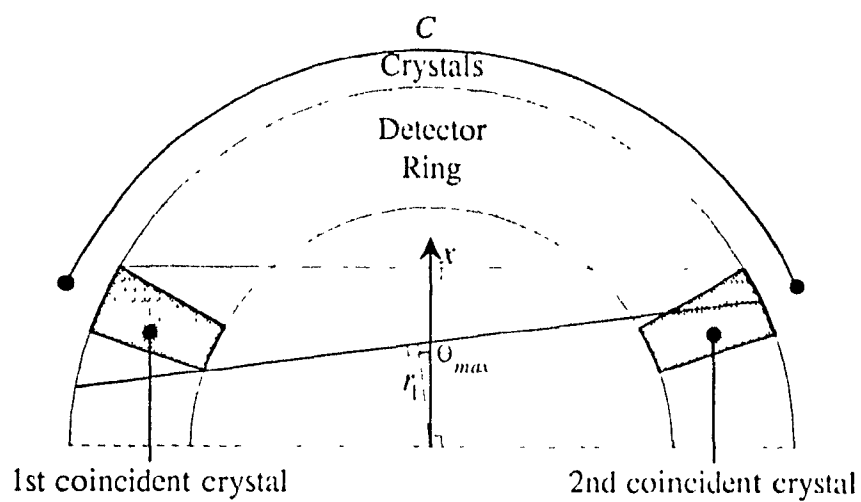


**Figure 4.3** Geometrical example of  $\theta_{max}$  as computed in Equation (4.15) for (a)  $r_1 \leq h$  and for (b)  $r_2 > h$ .

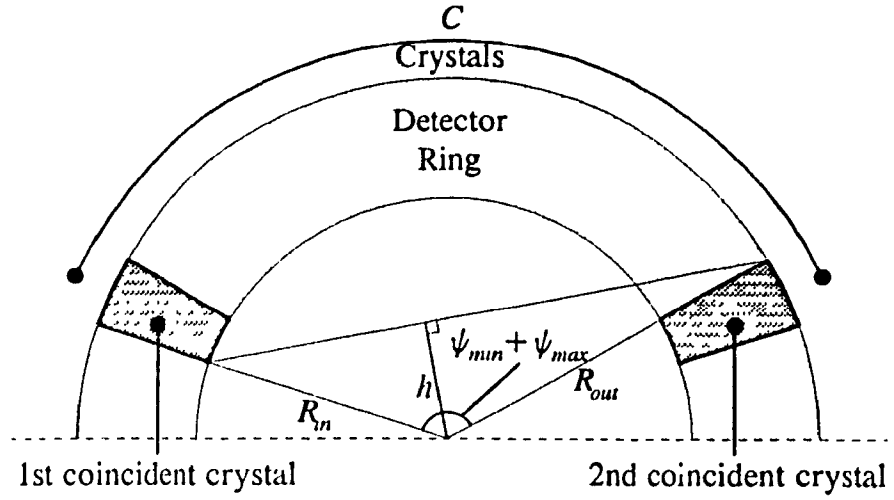


**Figure 4.4** Triangle used to define  $h$ .

The range of angles for the variable  $\theta$  in Equation (4.1) is then between  $-\theta_{max}$  and  $\theta_{max}$  where

$$\theta_{max}(r) = \begin{cases} \psi_{max} - \sin^{-1} \left| \frac{r}{R_{in}} \right|, & 0 \leq |r| \leq h \\ \psi_{max} - \sin^{-1} \left| \frac{r}{R_{out}} \right|, & \text{Otherwise} \end{cases}, \quad (4.15)$$

The function related to the detection of the coincident photons can be defined by the relationship:

$$D(r, \phi, \theta) = \left( \frac{\tau_1}{\mu_1} \right)^2 \left\{ 1 - \exp \left( -\mu_1 \frac{Y_{max}(r, \theta) - Y_{min}(r, \theta)}{\sin \phi} \right) \right\} \cdot \left\{ 1 - \exp \left( -\mu_1 \frac{Y_{max}(r, -\theta) - Y_{min}(r, -\theta)}{\sin \phi} \right) \right\}, \quad (4.16)$$



where  $\mu_1$  is the linear attenuation coefficient for the detectors at 511.1 keV and  $\tau_1$  is the photoelectric absorption partial interaction linear attenuation coefficient for the detectors at 511.1 keV. The first exponential function represent the attenuation in the first coincident crystal for the line of integration, the second exponential function, the attenuation in the second crystal.  $Y_{max}$  corresponds to the outermost point of the intersection between the line of integration and the coincident crystals.  $Y_{min}$  correspond to the innermost point of the intersection between the line of integration and the coincident crystals. The reader is referred to Figure 4.5 for a geometrical description of these variables. Mathematically, they correspond to:

$$Y_{max}(r, \theta) = \min\left(|r| \cdot \tan|\psi_{max} - \theta|, \sqrt{R_{out}^2 - r^2}\right), \quad (4.17)$$

where the function "min" returns the smallest value between the two in parenthesis and

$$Y_{min}(r, \theta) = \max\left(|r| \cdot \tan|\psi_{max} - f_c \alpha - \theta|, \sqrt{R_{in}^2 - r^2}\right), \quad (4.18)$$

where the function "max" returns the largest value between the two in parenthesis.

To define the functions related to the attenuation in the detector ring, other variables have to be defined. Two of these variables are the total attenuation path through the detector ring for the first and the second coincident crystal,  $p_1$  and  $p_2$ . These variables correspond to the path length between the detector's inner radius and the first or second crystal along the line of integration. These variables are dimensionless since they are multiplied by the linear attenuation coefficient of the media crossed by the line of integration. The reader is referred to Figure 4.5 for a geometrical description of these variables. Mathematically, they can be represented as:

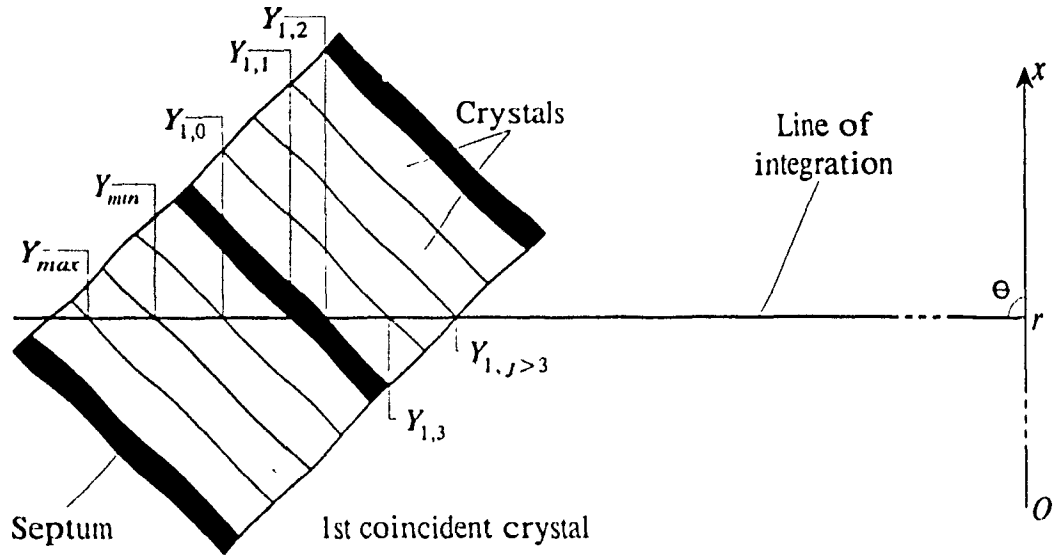


**Figure 4.5** Geometrical description of the variables used to define the detector functions. Only the ones related to the first coincident crystal are shown.

$$p_1(r, \theta) = \sum_{j=0}^{J_{\max}} \mu_{|j+1|_2} (Y_{1,j-1}(r, \theta) - Y_{1,j}(r, \theta)), \quad (4.19)$$

and

$$p_2(r, \theta) = \sum_{k=0}^{k_{\max}} \mu_{|k+1|_2} (Y_{2,k-1}(r, \theta) - Y_{2,k}(r, \theta)), \quad (4.20)$$

where  $\mu_1$  and  $\mu_0$  are the linear attenuation coefficient for the detector material and the septa material respectively. The indexes for the linear attenuation coefficient in the previous equations are taken modulo-2. When  $j=0$  and  $k=0$ , the functions  $Y_{1,-1}$  and  $Y_{2,-1}$  represent the innermost point of the intersection between the line of integration and the coincident crystals (the same definition as  $Y_{\min}$ ). They are thus defined by the relationships:

$$Y_{1,-1}(r, \theta) = Y_{\min}(r, \theta), \quad (4.21)$$

and

$$Y_{2,-1}(r, \theta) = Y_{min}(r, -\theta). \quad (4.22)$$

$Y_{min}$  is computed using Equation (4.18), (4.23), (4.24). When  $q \geq 0$ , the  $Y_{1,q}$ 's and the  $Y_{2,q}$ 's correspond to the distance between the origin of the line of integration and the intersection between detector block boundaries and the line of integration (see Figure 4.5). Mathematically, they are defined as:

$$Y_{1,q}(r, \theta) = \max \left( |r| \cdot \tan \left| \psi_{min} - \theta - \left( (N_c - i_c) f_c + \text{INT} \left( \frac{q}{2} \right) + |q|_2 f_s \right) \alpha \right|, \sqrt{R_m^2 - r^2} \right), \quad (4.23)$$

and

$$Y_{2,q}(r, \theta) = \max \left( |r| \cdot \tan \left| \psi_{min} + \theta - \left( (c + i_c - 1) f_c + \text{INT} \left( \frac{q}{2} \right) + |q|_2 f_s \right) \alpha \right|, \sqrt{R_m^2 - r^2} \right). \quad (4.24)$$

$j_{max}$  and  $k_{max}$ , the limits of the two summations in Equation (4.19) and Equation (4.20) mean that the summation is done until the value in parenthesis is equal to zero. This happens since the  $Y$ 's are all equal to the detector's inner radius for  $j > j_{max}$  and  $k > k_{max}$ .

The analytical coincidence rate is now completely defined using all the previous equations from Equation (4.1) to Equation (4.24). If the total number of annihilations is known instead of the activity, Equation (4.1) can also be used to compute the total number of coincidences detected for a given pair of crystals separated by  $c$  crystals by removing its time dependency. The activity is then replaced by the total number of annihilations over the volume of the source. The analytical mean projection is obtained by computing the coincidence rate or counts from  $c=1$  to  $c=N_r/2$ .

Notice that Equation (4.1) does not represent the counts for an individual pair of coincident crystals, but the sum of all the counts from all the individual pairs of coincident crystal separated by  $c$  around the ring. To obtain the counts for the individual pair of crystals, the summation over all  $i_c$  must be removed and the equation must be only for the  $i_c$  corresponding to the individual pair of crystals under investigation. The so modified Equation (4.1) must also be divided by  $N_D$  and  $N_S$ .

To validate the photons' recycling procedure, Monte Carlo simulations of the source distribution, the collimator and the detector were run for different GRH file sizes and different number of times the photons were recycled. These simulations were run for relatively small GRH files since, if our results were conclusive for these, the same would apply for longer runs. This has the advantage of reducing the time of the simulations and increasing the number of simulations which can be run over the same period. The Scanditronix PC2048B PET system [59] was chosen for all simulations. Each simulation modeled a 20 cm diameter 11 cm high cylindrical water flood phantom, a 15-slice multi-ring collimator (36 cm inner diameter and 50 cm outer diameter, direct slices thickness of 0.95 cm), and two rings of 64 BGO detector block (24 mm large by 50 mm high block, 30 mm deep and an array of 4x4 6 mm by 12.5 mm crystals per block). The attenuation geometry of the system is shown in Figure 4.6. This figure was done using the DRG program. The grey scale represents a logarithm scale of the linear attenuation coefficients of the materials at 511.1 keV. Air is at the bottom of the scale (white) and tungsten is at the top (black). To analyze the results from this simulated system, an analytical mean projection was computed using the previous equations and the quantities relative to the system as

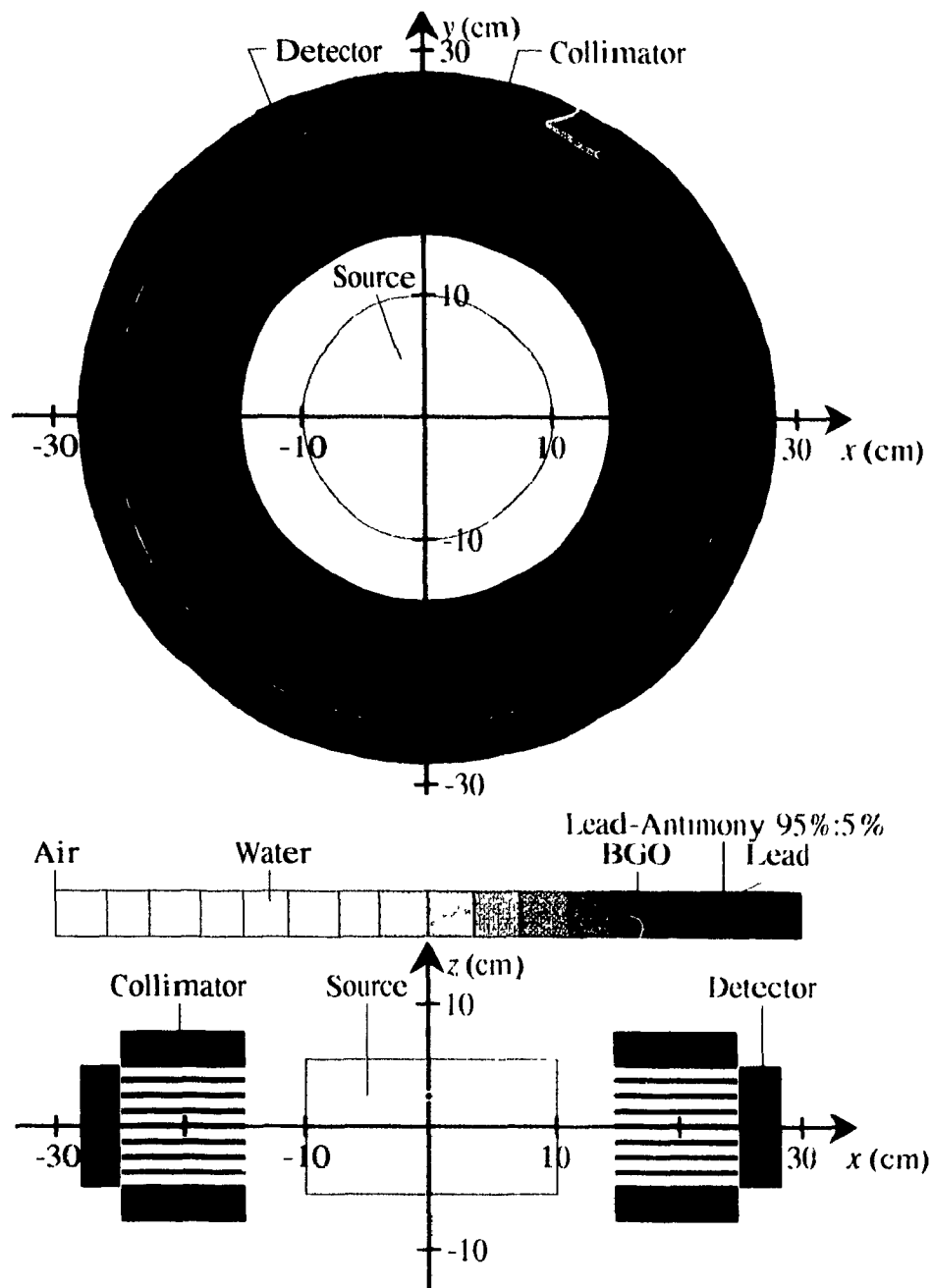


**Figure 4.6** Attenuation geometry used to test the recycling procedure. (a) Transverse cross section of the geometry at  $z=0$ . (b) Axial cross section of the geometry at  $y=0$ .

summarized in Table 4.1. In the table, the linear attenuation coefficients were computed from the parameters in the look-up table for an energy of 511.1 keV.

Table 4.2 gives the number of coincident counts as computed from Equation (4.1) with the parameters of Table 4.1 for all crystal separations of the system having a non-zero value. When the number of crystals separating the two coincident crystals was larger than  $N_b N_i / 2$  (which is 128 here),  $c$  was computed by subtracting the crystal separation from  $N_b N_i$ . The counts were normalized to one million counts detected. This corresponded to a uniform annihilation concentration of 1,711,474 annihilations per cubic centimetre in the source volume. Table 4.2 constituted the analytical mean projection. It included only the true coincident events detected in direct slices, each photon of the pair having only one interaction in the detectors depositing 511.1 keV. A graph representing the analytical mean projection is shown in Figure 4.7. As mentioned previously, the positron range and the

**Table 4.1** Summary of the parameters used to compute the theoretical mean projection.

Variables	Corresponding Value
$R_s$	10.00 cm
$R_{in}$	25.25 cm
$R_{out}$	28.25 cm
$z_s$	0.95 cm
$\mu_{med}$ (phantom medium is water)	$9.58 \times 10^{-2} \text{ cm}^{-1}$
$\mu_{air}$	$1.04 \times 10^{-4} \text{ cm}^{-1}$
$\mu_0$ (septa medium is lead)	$1.63 \text{ cm}^{-1}$
$\tau_1$ (detector medium is BGO)	$3.81 \times 10^{-1} \text{ cm}^{-1}$
$\mu_1$	$8.98 \times 10^{-1} \text{ cm}^{-1}$
$N_s$	8
$N_b$	64
$N_i$	4
$f_d$	0.9

**Table 4.2** Analytical number of true coincident counts per pair of crystals when each photon of the pair is depositing 511.1 keV into the crystal at only one interaction point.

Crystal separation	Counts	Crystal separation	Counts
94	1	129	14470
95	848	130	14446
96	6470	131	14439
97	12795	132	14419
98	16019	133	14438
99	17215	134	14471
100	17648	135	14529
101	17858	136	14556
102	17716	137	14632
103	17550	138	14723
104	17346	139	14854
105	17223	140	14926
106	16896	141	15064
107	16643	142	15218
108	16399	143	15433
109	16255	144	15549
110	15963	145	15749
111	15749	146	15963
112	15549	147	16255
113	15433	148	16399
114	15218	149	16643
115	15064	150	16896
116	14926	151	17223
117	14854	152	17346
118	14723	153	17550
119	14632	154	17716
120	14556	155	17858
121	14529	156	17648
122	14471	157	17215
123	14438	158	16019
124	14419	159	12795
125	14439	160	6470
126	14446	161	848
127	14470	162	1
128	14481		

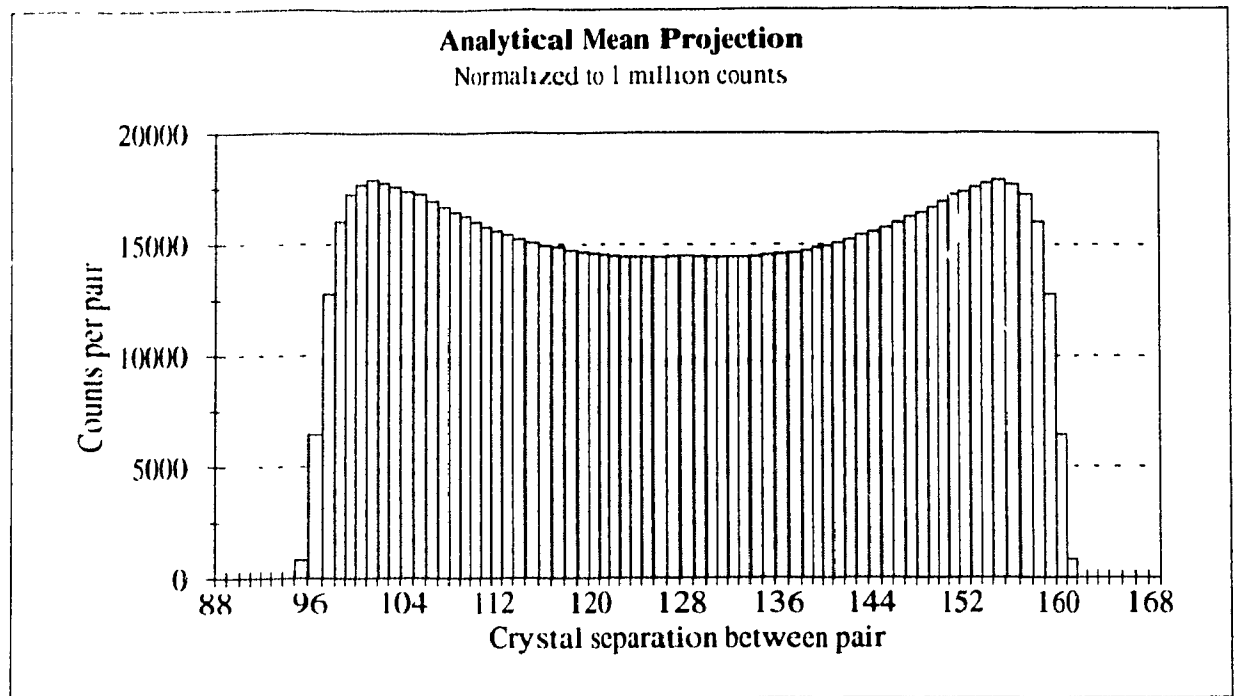


**Figure 4.7** Analytical mean projection for the simulated system.

photons' non-collinearity were turned off in the simulation programs to compare the simulations' mean projections with the analytical mean projection. The methodology to compare the projections is explained in the next section.

### 4.3 Superposing the Mean Projections

The analytical mean projection obtained in the previous section was compared to the simulated mean projections using the chi-square ( $\chi^2$ ) test for goodness of fit. This test is described below. For a more complete description the reader is referred to references [60,61,62]. The chi-square value was the value used to quantify the efficiency improvements due to the recycling technique.



The chi-square goodness of fit test is a test that verifies the conformity between an observed distribution (the simulated mean projection), and a theoretical distribution (the analytical mean projection). In general, the observations are distributed over  $l$  bins mutually exclusive and one wants to check if this simulated distribution is drawn from or fits the specified theoretical distribution. Let  $X_1, X_2, \dots, X_l$  be random variables of the counts observed for each bin and  $Np_1, Np_2, \dots, Np_l$ , the expected observations where the  $p_i$ 's represent the probability that whatever observation belongs to bin  $i$  and  $N$  is the total number of counts within the observed distribution, that is:

$$N = \sum_{i=1}^l X_i. \quad (4.25)$$

The possible generalization of the statistic which could measure the discrepancies existing between observed and expected counts is the variable  $\chi^2$  such that

$$\chi^2 = \sum_{i=1}^l \frac{(X_i - Np_i)^2}{Np_i}. \quad (4.26)$$

If  $\chi^2=0$ , observed and expected numbers of counts agree exactly while if  $\chi^2>0$ , they do not agree exactly. The larger the value of  $\chi^2$ , the larger the discrepancy between observed and expected numbers of counts.

In fact, the sampling distribution of  $\chi^2$  is approximated very closely by the chi-square distribution (given in Appendix C, page 118) if the expected observations  $Np_i$  are at least equal to 5, the approximation improving for larger values. If it is not the case, certain bins can be grouped together at the extremities of the distribution.  $l$  will then represents the

number of bins after grouping for the computation of the degrees of freedom of the chi-square. The number of degrees of freedom for this chi-square distribution is given by

$$v = l - 1, \quad (4.27)$$

since one degree of freedom is lost because of the restriction over the observations

$$\sum_{i=1}^l c_i = \sum_{i=1}^l N p_i = N. \quad (4.28)$$

From this relationship, if  $l-1$  of the expected observations are known, the remaining observation can be determined.

In practice, expected observations are computed on the basis of a hypothesis  $H_0$ . If under this hypothesis the value of  $\chi^2$  computed by Equation (4.26) is larger than some critical value such as  $\chi^2_{0.95}$  or  $\chi^2_{0.99}$ , which are the critical values at the 0.05 and 0.01 significance levels respectively, one would conclude that observed counts differ significantly from expected observations and would reject  $H_0$  by accepting a risk corresponding to the significance level of rejecting  $H_0$  whenever it was true. Otherwise, one would accept it or at least not reject it. This is called the chi-square test of hypotheses or significance. This test is usually used to determine how well theoretical distributions such as the normal (Gaussian), Poisson, multinomial, etc. fit empirical distributions. In this work, this test was not used to determine if the theoretical distribution fits the data, but to verify if the data in each bin follows Poisson statistics. The explanation is given below.

The theorem which summarizes the definition of the chi-square distribution is the following:

*Theorem 4.1:* Let  $Z_1, Z_2, \dots, Z_\nu$  be independent normally distributed random variables with mean 0 and variance 1. Such variables are commonly called standardized variables. Then  $\chi^2 = Z_1^2 + Z_2^2 + \dots + Z_\nu^2$  is chi-square distributed with  $\nu$  degrees of freedom.

This theorem signifies that for Equation (4.26) to be very close to be chi-square distributed, each terms representing a standardized variable  $Z_i$  corresponding to  $X_i$ , that is

$$Z_i = \frac{X_i - \mu}{\sigma} \quad (4.29)$$

must be very close to be normally distributed. That also means that each variable  $X_i$  must be very close to be a normally distributed variable with a mean  $\mu = Np_i$  and a variance  $\sigma^2 = Np_i$ . It is known that for reasonably large values of the mean  $\mu$ , the shape of the Poisson distribution is closely approximated by the normal distribution. Then, if Equation (4.26) is very closed to be chi-square distributed, then each  $X_i$  is very close to be a Poisson distributed around the mean  $Np_i$  if that mean is large enough.

When the simulated mean projections was compared to the analytical mean projection, it was assumed that the analytical mean projection really fits the simulated mean projection. So, the fitting of the analytical mean projection over the simulated mean projection was not the hypothesis tested. This assumption was formerly verified using conventional Monte Carlo simulations. So, if the theoretical distribution really represented the simulated mean projections when the recycling procedures were used, a value of  $\chi^2$  obtained using Equation (4.26) larger than the critical value meant that something else was wrong: according to the previous paragraph, the other possibility was that the counts

observed in each bin were not following Poisson statistics. Then, a test derived from the chi-square goodness of fit test was used to verify that the observed counts during simulation followed Poisson statistics.

The test used in this work is the following. The theoretical probability distribution of the mean projection (the  $p_i$ 's) were obtained by dividing each value of Table 4.2 by the total number of counts detected in the table, that is 1 million counts. Before testing the recycling procedure, the crystal separations at the extremities of the mean projection were regrouped to ensure that each bin had at least 5 counts (see above). Thus, crystal separations of 94, 95, and 96 crystals were regrouped in bin 1 and crystal separations of 160, 161 and 162 crystals were regrouped in bin  $l=65$ . Bin 2 corresponded to a crystal separation of 97 crystal, bin 3 to 98 crystals and so on. So,  $X_1$  corresponded to the counts observed in bin 1 (sum of the simulated counts for pair of crystals having a crystal separation of 94, 95 and 96 crystals),  $X_2$  corresponded to the counts in bin 2 (simulated counts for pair of crystal having a crystal separation of 97 crystals), and so on. The hypothesis  $H_0$  was: The simulation produced counts that were Poisson distributed for each bin. Thus,  $H_0$  was plausible and could not be rejected if

$$\chi^2 \leq \chi^2_{1-\alpha, \nu} \quad (4.30)$$

where  $\alpha$  is the significance level and  $\nu$  the degree of freedom. Otherwise,  $H_0$  was rejected. A significance level of 0.05 was used. Since  $l=65$ , the degree of freedom was 64 as computed by Equation (4.27). Figure 4.8 gives the probability distribution of the  $\chi^2$  with a 64 degrees of freedom. The vertical line corresponds to the value of  $\chi^2_{0.95, 64}$  which is 83.67 [63].  $H_0$  was rejected if  $\chi^2$  was larger than 83.67. The mean projections from the

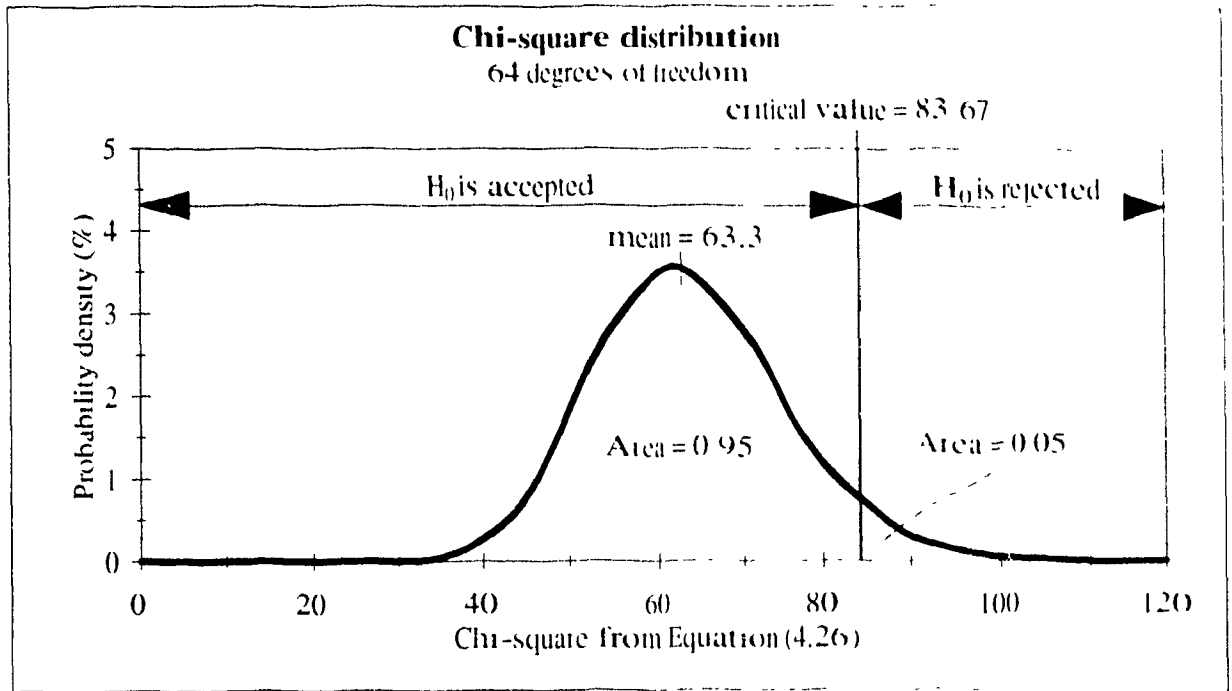


**Figure 4.8** The  $\chi^2$  probability density with  $\nu=64$ .  
simulations were computed with a procedure derived from ANALYZE.

#### 4.4 Comparing the Results

First of all, to compare simulation having the same statistical precision we needed to define a parameter which could quantify the statistical precision of the simulation. To quantify it, we defined a quality factor  $Q$  representing the standard error of the simulation as

$$Q = C \frac{\chi^2}{\sqrt{N}}, \quad (4.31)$$

where  $\chi^2$  is obtained from Equation (4.26).  $N$  is the total number of counts in the simulated mean projection.  $C$  is an arbitrary constant. It was set to

$$C = \frac{\sqrt{14112}}{\chi^2_{0.50,64}} = \frac{\sqrt{14112}}{63.3} = 1.88 \quad (4.32)$$

which corresponded to the square root of the total number of counts in the mean projection described above (14112 true coincident events where both photons deposited 511 keV in the detectors at one interaction point) for the long conventional Monte Carlo simulation described below divided by the mean of the chi-square distribution for 64 degrees of freedom. That way, the  $Q$  factor for the long conventional Monte Carlo simulation was about 1. Notice that as the statistical precision increases, the  $Q$  factor decreases.

To reduce the standard error by a factor of  $k$ , the sample size needs to be increased  $k^2$ -fold. With this definition of the  $Q$  factor, the  $Q$  factor was proportional to the standard error since if the data follows Poisson statistics,  $\chi^2$ , as defined by Equation (4.26) and illustrated in Figure 4.8, was located about the mean (63.3 for 64 degrees of freedom [60]).

As mentioned previously, a long conventional Monte Carlo simulation of the PET scanner described in Section 4.2 was first run to verify that the simulated mean projections were described by the analytical mean projection. The  $Q$  factors were computed for parts of the detection phase GRH file and plotted on a graph of the  $Q$  factor versus the number of counts in the simulation mean projections. The results are shown in a graph in the next chapter.

Then the average simulation time to produce one coincident event in the mean projection for each phase (source/phantom, collimation and detection) of the long

conventional Monte Carlo simulation was calculated. Remember that the mean projections are the ones defined previously in Section 4.2. The average simulation time was computed by dividing the time required to run each phase of the simulation by the total number of counts in the simulated mean projection. The average simulation disk space necessary to produce one coincident event in the mean projection was also calculated. This was done by dividing the size of each GRH file produced by each phase by the total number of counts in the simulated mean projection. Usually, the GRH output file size is user-specified. However in these simulations, it corresponded to the actual file size need to actually follow all the photons which were stored in the input GRH file, excepted in the source/phantom phase of the simulation where no GRH input file are required. The GRH output file of the source/phantom phase was set to 1 million blocks (1 block = 512 bytes). The results are given in the next chapter. These average simulation time and disk space were used to compare the simulation time and disk space of simulation using recycling procedures with those of a conventional simulation using the method described below.

Then many short simulations having a GRH output file from the source/phantom phase of the simulation four times smaller than that of the long simulation (i.e. 250000 blocks) and using different recycling combinations were run. For each simulation, the same GRH file from the source/phantom phase of the simulation were used. In these simulations, the intermediate GRH files were read from one to five times by the collimation phase and from one to seven times by the detection phase. This gave a total of 35 (7x5) different simulations which used different recycling procedures.

For each simulation, the number of counts in the mean projection and the  $Q$  factor, computed using Equation (4.31), was recorded. These were plotted on a graph in the next chapter. This graph allow one to verify if the simulation data were following Poisson statistics. The simulation time and disk space required by each simulation were also recorded.

To compare the efficiency improvements of the recycling technique over conventional simulations, the time and the disk space used by a simulation using recycling and giving Poisson statistics were compared to the time and the disk space used by a conventional simulation of the same system giving the same number of counts in the mean projection. This corresponded to simulations having about the same statistical precision\*. The time and disk space of the conventional simulations were computed by multiplying the counts in the mean projection by the average times and disk spaces recorded previously.

To avoid biased results and to really compare simulation having the same statistical precision instead of simulation giving the same number of counts in the mean projections for simulations not giving Poisson statistics we did the following: when the simulation gave a  $\psi^2$  value which was larger than the 0.05 significance level, the total number of counts in the simulated mean projection was reduced to

$$N' = \left( C \frac{\chi_{0.95;64}^2}{Q} \right)^2 \quad (4.33)$$

---

\* It is impossible to compare simulations having exactly the same statistical precision since the total counts in the simulated mean projection also follows Poisson statistics. Nevertheless, the simulations which were compared had enough counts in their mean projection so that their standard deviation of the total count was always lower than 2%.



which corresponds to the total number of counts required for the given  $Q$  factor to produce data which follow Poisson statistics. The result of all these simulations are given in the next chapter.

# Results and Discussion

---

### 5.1 Introduction

This chapter gives the results of the improvement done in the PET scanner Monte Carlo simulation programs called PETSIM. For all cases, including the tests on the new attenuation coefficients, a system comparable to the Scanditronix PC2048B PET scanner was simulated. Its description is given in Section 4.2 of the previous chapter. In this chapter, Section 5.2 gives the results for the improvement in the accuracy of PETSIM. Section 5.3 finds the characteristics of a long conventional Monte Carlo simulation. Section 5.4 gives the improvement on the efficiency of Monte Carlo simulation when the recycling technique is used.

### 5.2 Improvements in PETSIM's accuracy

Tables 5.1-5.5 represent an exhaustive look-up table which contains the attenuation parameters of the materials which can currently be used in PETSIM. To make the look-up table clearer, the materials were sorted in five categories: phantom materials, collimator materials, detector materials, packing materials (materials between the detector blocks) and gases. The last column is not part of the look-up table. It is shown here to give references to the reader who wants to know where the composition of the material was taken. The look-up table can be updated easily with the programs XGAM and ATTNPARAM if more, or even new materials are needed. Evaluation of detector materials can be performed

**Table 5.1** Compton scattering and photoelectric absorption partial interaction linear attenuation coefficient parameters for biological materials.

BIOLOGICAL MATERIAL	Compton	Photoelectric					Ref.
	Electron Density	Parameters Above K-edge		K-edge Energy	Parameters Below K-edge		
	$\rho_e$ ( $e/cm^3$ ) $\times 10^{23}$	$A_1$ $\times 10^3$	$B_1$	$E_K$ (keV)	$A_2$ $\times 10^3$	$B_2$	
Blood	3.513	7.110	3.178	< 15.0	--	--	[49]
Bone	5.267	39.89	3.075	< 15.0	--	--	[9]
Brain	3.438	7.031	3.171	< 15.0	--	--	[49]
Brain Stem	3.500	7.727	3.169	< 15.0	--	--	[49]
Cerebellum	3.428	7.044	3.172	< 15.0	--	--	[49]
Cerebrum	3.433	7.002	3.171	< 15.0	--	--	[49]
Cer.-Spin. Fluid	3.420	7.415	3.183	< 15.0	--	--	[49]
Eye Lenses	3.635	6.464	3.195	< 15.0	--	--	[49]
Fat	3.061	3.725	3.202	< 15.0	--	--	[9]
Hair	4.202	7.412	3.074	< 15.0	--	--	[49]
Heart	3.415	6.658	3.178	< 15.0	--	--	[49]
Lung	0.861	1.799	3.173	< 15.0	--	--	[49]
Muscle	3.445	7.070	3.175	< 15.0	--	--	[9]
Skin	3.639	6.618	3.182	< 15.0	--	--	[49]
Water	3.343	6.869	3.192	< 15.0	--	--	[50]

**Table 5.2** Compton scattering and photoelectric absorption partial interaction linear attenuation coefficient parameters for collimator materials.

COLLIMATOR MATERIAL	Compton	Photoelectric					Ref.
	Electron Density	Parameters Above K-edge		K-edge Energy	Parameters Below K-edge		
	$\rho_e$ (e/cm <sup>3</sup> ) x10 <sup>23</sup>	$A_1$  x10 <sup>3</sup>	$B_1$	$E_K$ (keV)	$A_2$  x10 <sup>3</sup>	$B_2$	
Lead	27.04	8720.	2.588	90.0	1722.	2.549	[50]
Lead 95 % (5% Antimony)	26.58	8342.	2.590	90.0	1444.	2.506	[50]
Tungsten	46.90	15540.	2.648	70.0	4202.	2.716	[50]

**Table 5.3** Compton scattering and photoelectric absorption partial interaction linear attenuation coefficient parameters for detector materials.

DETECTOR MATERIAL	Compton	Photoelectric					Ret.
	Electron Density	Parameters Above K-edge		K-edge Energy	Parameters Below K-edge		
	$\rho_e$ ( $e/cm^3$ ) $\times 10^{23}$	$A_1$  $\times 10^1$	$B_1$	$E_K$ (keV)	$A_2$  $\times 10^1$	$B_2$	
BeO	18.06	3793.	2.584	95.0	994.2	2.593	[51]
Al	10.44	2406	2.778	40.0	405.0	2.785	[50]
Si	14.20	1529.	2.940	< 15.0	--	--	[50]
P	17.40	3800	2.717	55.0	819.8	2.759	[51]
S	7.341	20.82	3.179	< 15.0	--	--	[50]
Cl	9.429	1999.	2.791	35.0	321.7	3.179	[50]
Fe (100)	8.818	2840.	2.588	90.0	561.0	2.549	[52]
Fe (100)	16.66	3940.	2.588	90.0	780.9	2.550	[50]
Pb	16.01	3266.	2.588	90.0	667.0	2.556	[50]
UO <sub>2</sub>	23.84	5952.	2.522	110.0	696.0	2.335	[50]
YAlO	14.93	1209.	2.878	< 20.0	--	--	[53]

more simply through simulations with the use of these programs and the look-up table.

Figure 5.1 gives an example of the command lines corresponding to the attenuation geometry definition in the PHANTOM program required to simulate a simple phantom. Figure 5.1(a) corresponds to the command lines required by the previous versions of PETSIM. The user had to remember and enter three parameters corresponding to the

```

CYL 0.3335, 9.444E3, 3.322, 10.00, 5.50, -5.50
CYL 1.0E-7, 0.00000, 0.000, 15.00, 6.00, -6.00
(a)

```

```

CYL WATER 10.00, 5.50, -5.50
CYL AIR 15.00, 6.00, -6.00
(b)

```

**Figure 5.1** Command lines used by the PHANTOM program to define the attenuation geometry of a simple 10 cm radius 11 cm high cylindrical water phantom. (a) Previous PETSIM version. (b) New PETSIM version.

**Table 5.4** Compton scattering and photoelectric absorption partial interaction linear attenuation coefficient parameters for packing materials and other solid materials.

PACKING MATERIAL OR OTHER SOLID MATERIAL	Compton	Photoelectric					Ref.
	Electron Density	Parameters Above K-edge		K-edge Energy	Parameters Below K-edge		
	$\rho_e$  (e/cm <sup>3</sup> ) x10 <sup>23</sup>	$A_1$  x10 <sup>3</sup>	$B_1$	$E_K$  (keV)	$A_2$  x10 <sup>3</sup>	$B_2$	
Aluminum	7.840	92.11	3.131	< 15.0	--	--	[50]
Bakelite	4.451	4.963	3.208	< 15.0	--	--	[9]
Calcium	4.628	176.2	3.054	< 15.0	--	--	[50]
Copper	24.51	2175.	2.967	< 15.0	--	--	[50]
Diamond	10.56	10.20	3.218	< 15.0	--	--	[50]
Graphite	6.769	6.540	3.218	< 15.0	--	--	[50]
Kovar	22.81	1709.	2.987	< 15.0	--	--	[50]
Lead Glass	2.124	415.9	2.588	< 15.0	--	--	[54]
Lucite	3.833	4.972	3.202	< 15.0	--	-	[9]
Polystyrene	3.380	2.805	3.218	< 15.0	--	--	[9]
Pyrex	6.676	48.16	3.131	< 15.0	--	--	[55]
Tantalum	40.33	13350.	2.655	70.0	3522.	2.721	[50]
Tin	18.47	4377.	2.811	30.0	645.6	2.802	[50]

**Table 5.5** Compton scattering and photoelectric absorption partial interaction linear attenuation coefficient parameters for gases.

GAS	Compton	Photoelectric					Ref.
	Electron Density	Parameters Above K-edge		K-edge Energy	Parameters Below K-edge		
	$\rho_e$  (e/cm <sup>3</sup> ) x10 <sup>17</sup>	$A_1$  x10 <sup>-3</sup>	$B_1$	$E_K$  (keV)	$A_2$  x10 <sup>-3</sup>	$B_2$	
Air	3622.	7680.0	3.169	< 15.0	--	--	[9]
Hydrogen	500.4	0.3360	3.295	< 15.0	--	--	[9]
Nitrogen	3506.	5768.0	3.205	< 15.0	--	--	[9]
Oxygen	4011.	10280.	3.192	< 15.0	--	--	[9]

Compton scattering and photoelectric attenuation coefficients. Figure 5.1(b) corresponds to the command lines required due to the development of the look-up table. As the reader can see in Figure Figure 5.1, the look-up table really eases the use of PETSIM; the user no longer needs to write the attenuation parameters (or "magic" numbers) but only the name of the material used. The information about the attenuation characteristics are read by the simulation programs by matching the user-specified material names with the appropriate ones in the look-up table.

Figure 5.2 shows how well Equation (1.12) for the Compton scattering partial interaction linear attenuation coefficients and the parametric model of Equation (3.2) for the photoelectric absorption partial linear attenuation coefficients fit the data from XGAM. However, a discrepancy appears at energies lower than about 100 keV for the Compton scattering partial interaction linear attenuation coefficient. Because XGAM uses a combination of the Klein-Nishina formula and the non-relativistic Hartree-Fock incoherent scattering functions (which is about equal to 1 above 100 keV) to calculate the incoherent scattering and PETSIM only uses the Klein-Nishina relationship, the two curves diverge at lower energy. The discrepancy is even larger for high atomic number materials since the electrons can not be considered free anymore. But this does not affect the precision of PET simulation since at energies lower than 100 keV, the probability of the photon undergoing photoelectric effect is usually much larger than Compton scattering, and this is especially true for high atomic number materials. Furthermore, in the simulation programs the user usually uses a cut-off energy which is above the region where the discrepancy becomes important, so the difference between the two curves of the Compton scattering linear

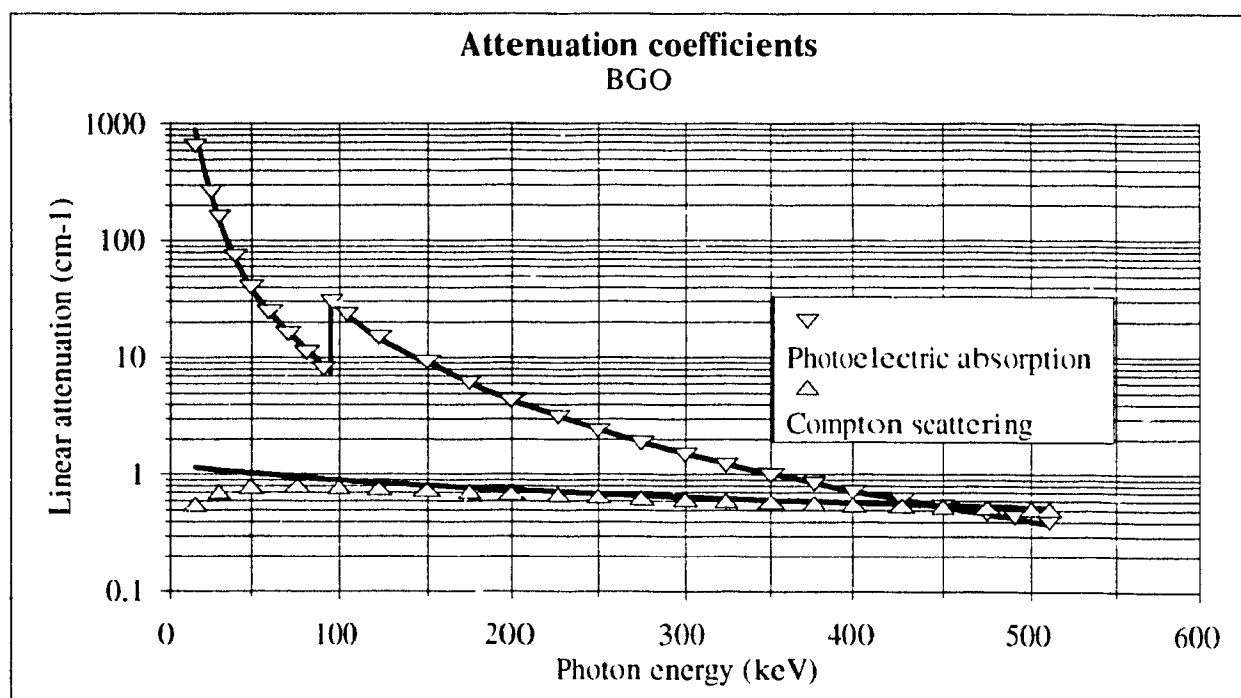
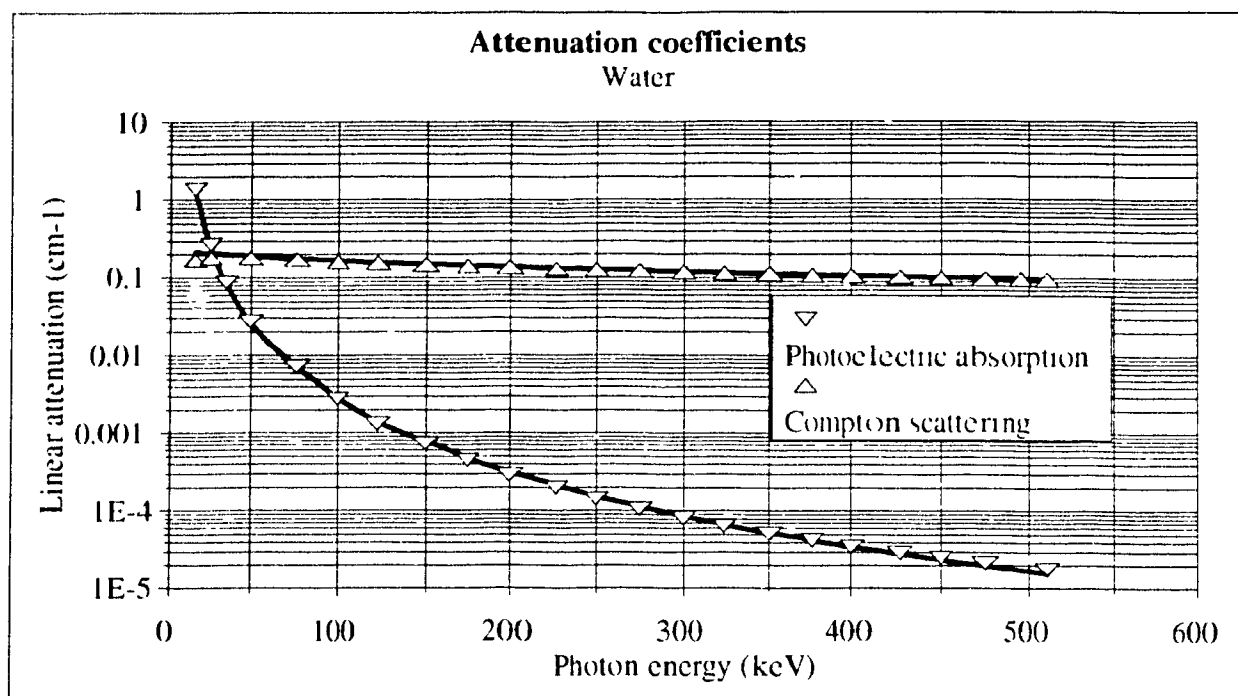
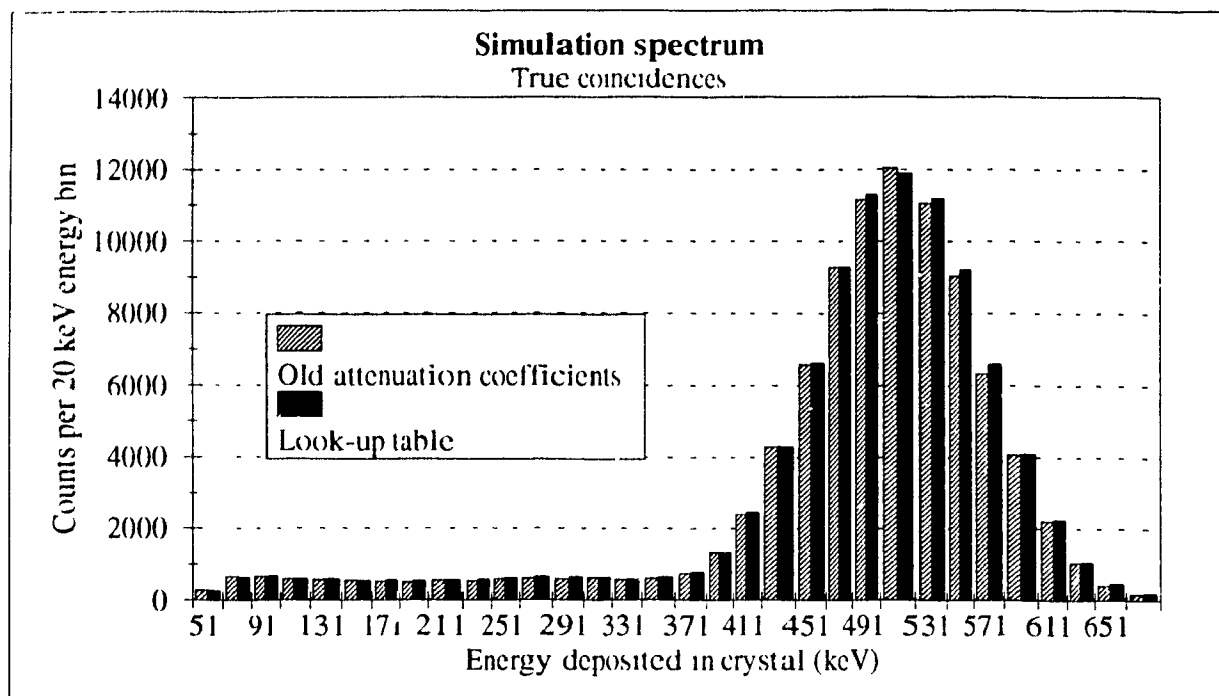


**Figure 5.2** Examples of how well the parameters fit curves through photoelectric and Compton scattering partial linear attenuations coefficients. The data points are from XGAM.

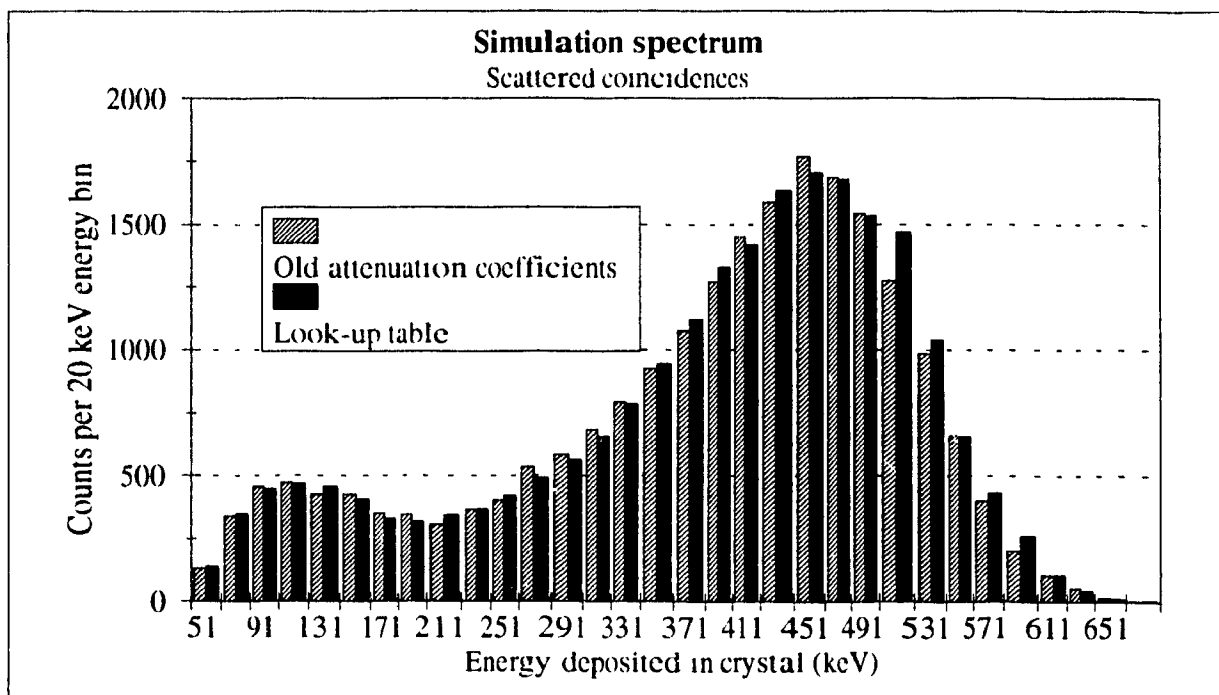
attenuation is not significant for PET simulations.

Figure 5.3 shows that almost exactly the same energy spectra for both true and scattered coincidences were produced by the simulation using the system described in Section 4.2 using the previous attenuation parameters and the new attenuation parameters stored in the look-up table. The new attenuation parameters includes the K-shell absorption peak for absorption energy larger than 15 keV as opposed to the previous attenuation parameters. Of course, in the true energy spectra, all true coincidences were accepted (as opposed to the true coincidences in the mean projections as defined in Section 4.1), otherwise the spectra would have given a Gaussian centred on 511.1 keV. These show that the new attenuation coefficients do not alter the conclusions of the previous papers.





(a)



(b)

**Figure 5.3** Spectrum from PETSIM simulation for (a) true coincidences and (b) scattered coincidences.

### 5.3 Characteristics of a conventional Monte Carlo simulation

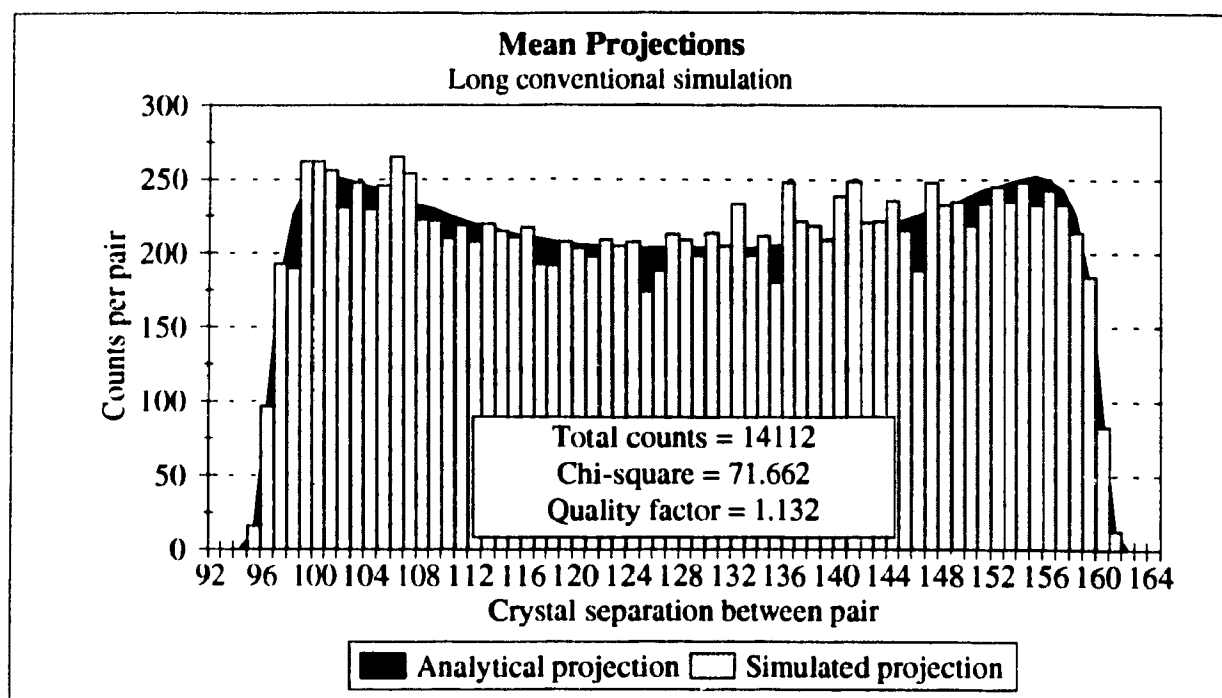
Table 5.6 gives the characteristics of the long conventional Monte Carlo simulation of the system described in Section 4.2 using PETSIM. The disk space corresponds to the disk space used by each phase's GRH output file. The time correspond to the CPU time used by each phase of the simulation. The average time and disk space correspond to the average time and disk space required to produce 1 event in the simulated mean projection. The simulation was run on a VAXstation 3100. This table clearly show that the most time consuming phase is the phantom phase. It is also the one that requires the most disk space.

Figure 5.4 compares the simulated mean projection with the theoretical mean projection. In this figure, both projections have the same total number of counts. This figure shows that PETSIM produced a mean projection for a long conventional simulation that is comparable to the theoretical mean projection

**Table 5.6** Characteristics of a long conventional Monte Carlo simulation using PETSIM.

Number of counts in mean projection			14112	
Chi-square $\chi^2$			71.662	
Quality factor $Q$			1.132	
Phase	Disk space (blocks)	Average Disk space (blocks)	Time (minutes)	Average Time ( $\times 10^{-1}$ minutes)
source/phan.	1000000	70.86	631.68	44.76
collimation	126490	8.96	106.10	7.52
detection	105400	7.47	31.96	2.26
total	1231890	87.29	769.74	54.55

1 block = 512 bytes



**Figure 5.4** Comparison between the simulated mean projection of a long conventional Monte Carlo simulation and the theoretical mean projection. The system used was the one described in section 4.2.

Figure 5.5 gives the  $Q$  factor defined in Section 4.4 for part of the long simulation as a function of the total number of counts in the mean projection. The line representing the mean was computed using  $\chi^2_{0.50,64} = 63.3$  in Equation (4.31). The line representing the 0.05 significance level was computed using  $\chi^2_{0.95,64}$  in Equation (4.31). The data points are not completely independent since they were obtained from only one simulation, i.e. that the counts in the mean projections that were used to compute a given data point were also used for the subsequent ones. Nevertheless, this figure shows that the events recorded in the mean projection were following Poisson statistics since no  $Q$  factors are above the 0.05 significance level line (refer to the definition of the hypothesis  $H_0$  defined in Section 4.3).

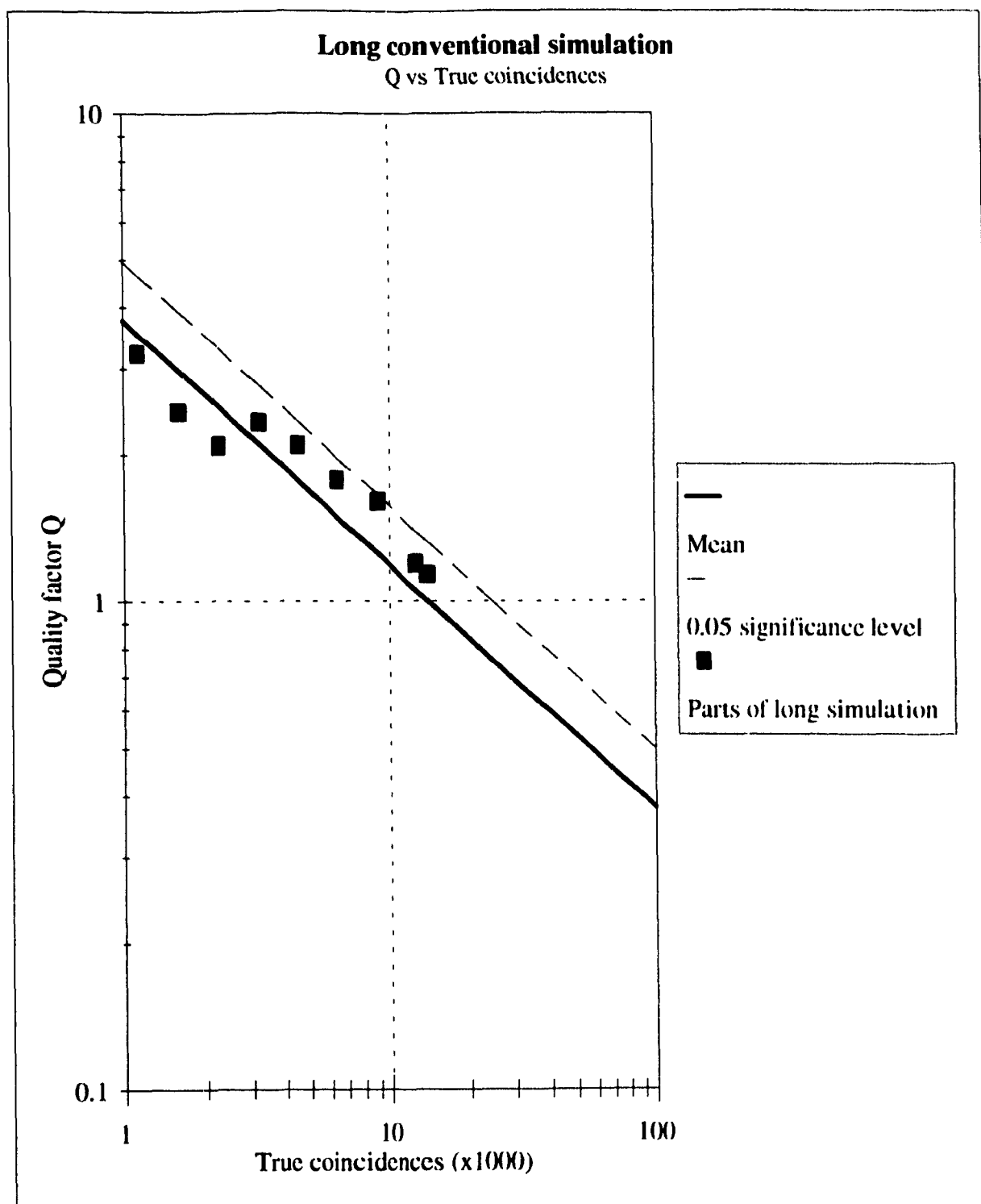


**Figure 5.5** Quality factor as a function of the total number of counts in the mean projection for part of the long conventional Monte Carlo simulation of the system described in section 4.2.

### 5.4 Efficiency improvements due to recycling

In this section, the following convention was used: a simulation where the intermediate GRH files were read  $x$  times by the collimation phase and  $y$  times by the detection phase was said to have the recycling procedure Col  $x$ , Det  $y$ . Thus, a simulation having a recycling procedure Col 1, Det 1 was simply a conventional Monte Carlo simulation where the intermediate GRH file produced by the source/phantom phase of the simulation had 250000 blocks. The recycling techniques were used when  $x$  or  $y$  was larger than 1.

Table 5.7 gives the characteristics of the simulation using the recycling procedure Col 1, Det 1. Since this is a conventional Monte Carlo simulation, the time and disk space required for each phase of the simulation is simply four times smaller than for the previous long Monte Carlo simulation (Table 5.6). For the same reason, the average time

**Table 5.7** Characteristics of the simulation using the recycling procedure Col 1, Det 1.

Number of counts in mean projection			3584	
Chi-square $\chi^2$			76.422	
Quality factor $Q$			2.396	
Phase	Disk space (blocks)	Average Disk space (blocks)	Time (minutes)	Average Time ( $\times 10^{-3}$ minutes)
source/phan.	250000	69.75	156.26	43.60
collimation	31640	8.83	26.71	7.45
detection	26370	7.36	8.11	2.26
total	308010	85.94	191.08	53.31

1 block = 512 bytes

and disk space required for each phase of the simulation to produce 1 event in the mean projection is about the same as for the long conventional Monte Carlo simulation.

Figure 5.6 shows the mean projection of the simulation which used the recycling procedure Col 1, Det 1. The reader can notice the increase of noise compared to Figure 5.4. The reason for this is that the simulation was four times shorter, thus the total number of counts in the mean projection was about four times smaller. The  $Q$  was thus about twice as large as for the long conventional simulation.

Table 5.8 gives the characteristics of the simulation using the recycling procedure Col 3, Det 2. Since the photons from the intermediate GRH file produced by the source/phantom phase of the simulation were read three times in the collimation phase, the

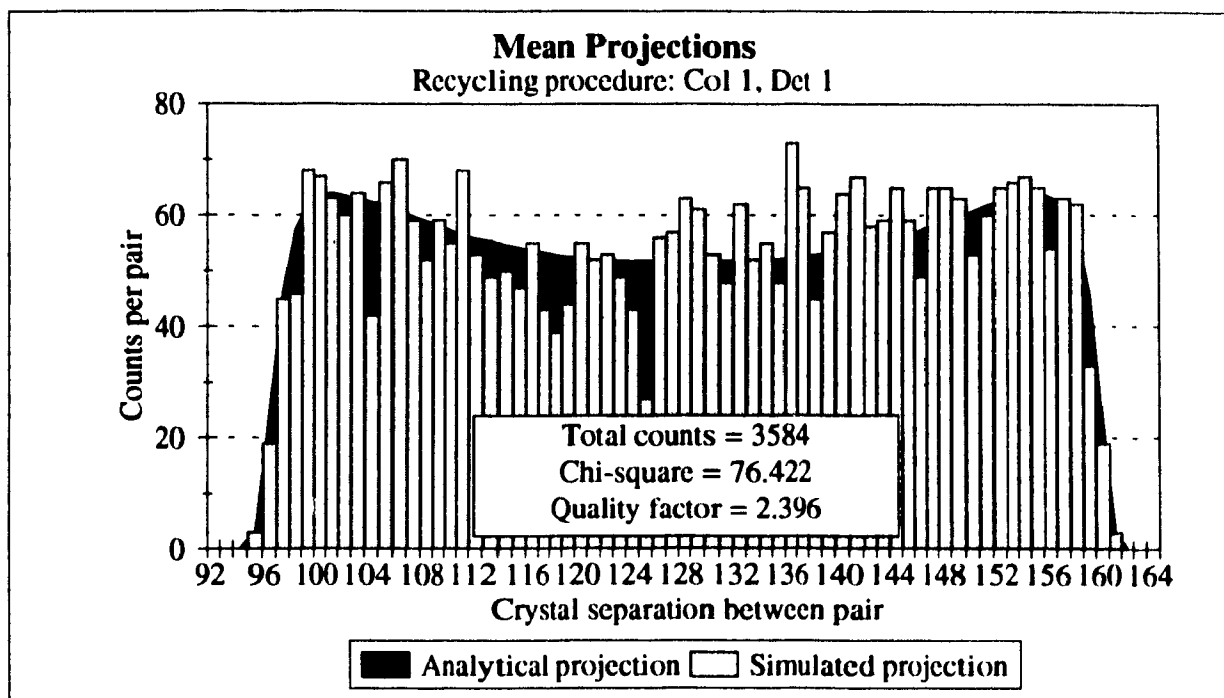


**Figure 5.6** Comparison between the simulated mean projection of a simulation using the recycling procedure Col 1, Det 1 and the theoretical mean projection.

**Table 5.8** Characteristics of the simulation using the recycling procedure Col 3, Det 2.

Number of counts in mean projection			20990	
Chi-square $\chi^2$			81.204	
Quality factor $Q$			1.052	
Phase	Disk space (blocks)	Average Disk space (blocks)	Time (minutes)	Average Time ( $\times 10^{-3}$ minutes)
source/phan.	250000	11.91	156.26	7.44
collimation	94680	4.51	79.86	3.80
detection	157710	7.51	50.51	2.41
total	502390	23.93	286.63	13.65

1 block = 512 bytes

time and disk space for this phase was about three times larger than for the simulation using the recycling procedure Col 1, Det 1. This increased the number of photons going out of the collimation phase by a factor of about 3. Similarly, since the intermediate GRH file produced by the collimation phase of the simulation was three times larger than for the simulation using the recycling procedure Col 1, Det 1 and because the file was read twice by the detection program, the time and disk space required by the detection phase was about 6 times ( $3 \times 2$  times) larger than for the simulation using the recycling procedure Col 1, Det 1. Table 5.8 shows the effect of recycling on the average simulation time and disk space required. Compared with the simulation using the recycling procedure Col 1, Det 1, both the average simulation time and the average disk space required were reduced for the source/phantom phase (reduced by about 1/6) and for the collimation phase (reduced by about 1/2) because more counts were obtained in the mean projection for the same GRH file from the source/phantom phase of the simulation. Thus, by comparing the total average

simulation time and disk space required from Table 5.7 and Table 5.8, the reader can notice that the overall simulation time and disk space required to obtain the same number of counts in the mean projection than a conventional Monte Carlo simulation are reduced when recycling is used. The quantification of the improvement in terms of time and disk space required are given in the next sub-sections.

Figure 5.7 shows the mean projection of the simulation which used the recycling procedure Col 3, Det 2. The reader can notice the reduction of noise compared to Figure 5.6, and this for the same intermediate GRH file from the source/phantom phase of the simulation. The total number of counts in the mean projection was about 6 times larger. The  $Q$  was also reduced.

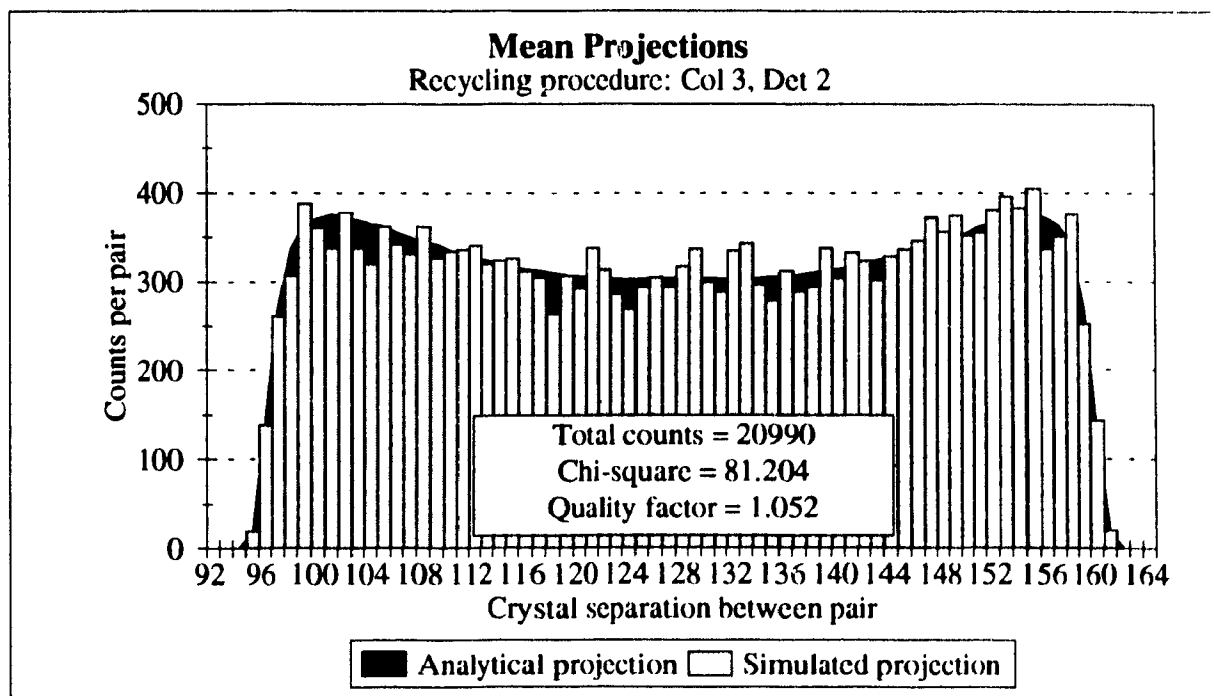


**Figure 5.7** Comparison between the simulated mean projection of a simulation using the recycling procedure Col 3, Det 2 and the theoretical mean projection.



The characteristics and the mean projections of the other 33 simulations were calculated but, to reduce the length of this thesis, they were excluded. Nevertheless, they were used to evaluate the time and disk space saved by the recycling technique. Their  $Q$  factors were also plotted in Figure 5.8. That way, the reader can understand the effect of recycling without the characteristics of all simulations.

Figure 5.8 gives the  $Q$  factor defined in Section 4.4 for part of the long simulation as a function of the total number of counts in the mean projection for simulations using different recycling procedures. The signification of the straight lines are the same as the ones in Figure 5.5. There are seven data points per set (excluding the last set). For each set, the left-hand data point corresponds to a recycling procedure Col  $x$ , Det 1 and the right-hand, to a recycling procedure Col  $x$  Det 7, where  $x$  was set between 1 and 5. The data points do not lay on a smooth curve since they were obtain from only one simulation. To obtain a smooth curve, which is computationally impossible, the mean of a large number of simulations would have to be computed for each data point. Nevertheless, the reader can notice that, as the number of counts increases, the  $Q$  factor generally decreases, thus giving an improved statistical precision for a given GRH file produced by the source/phantom phase of the simulation. The data points tend to level off when the data are "over" recycled, meaning that even if the number of events in the mean projection increased, the  $Q$  factor was not improved anymore. All data points above the 0.05 significance level line indicate that the counts in the bins of the simulated mean projections were not Poisson distributed when the corresponding recycling procedure was used in these simulations.

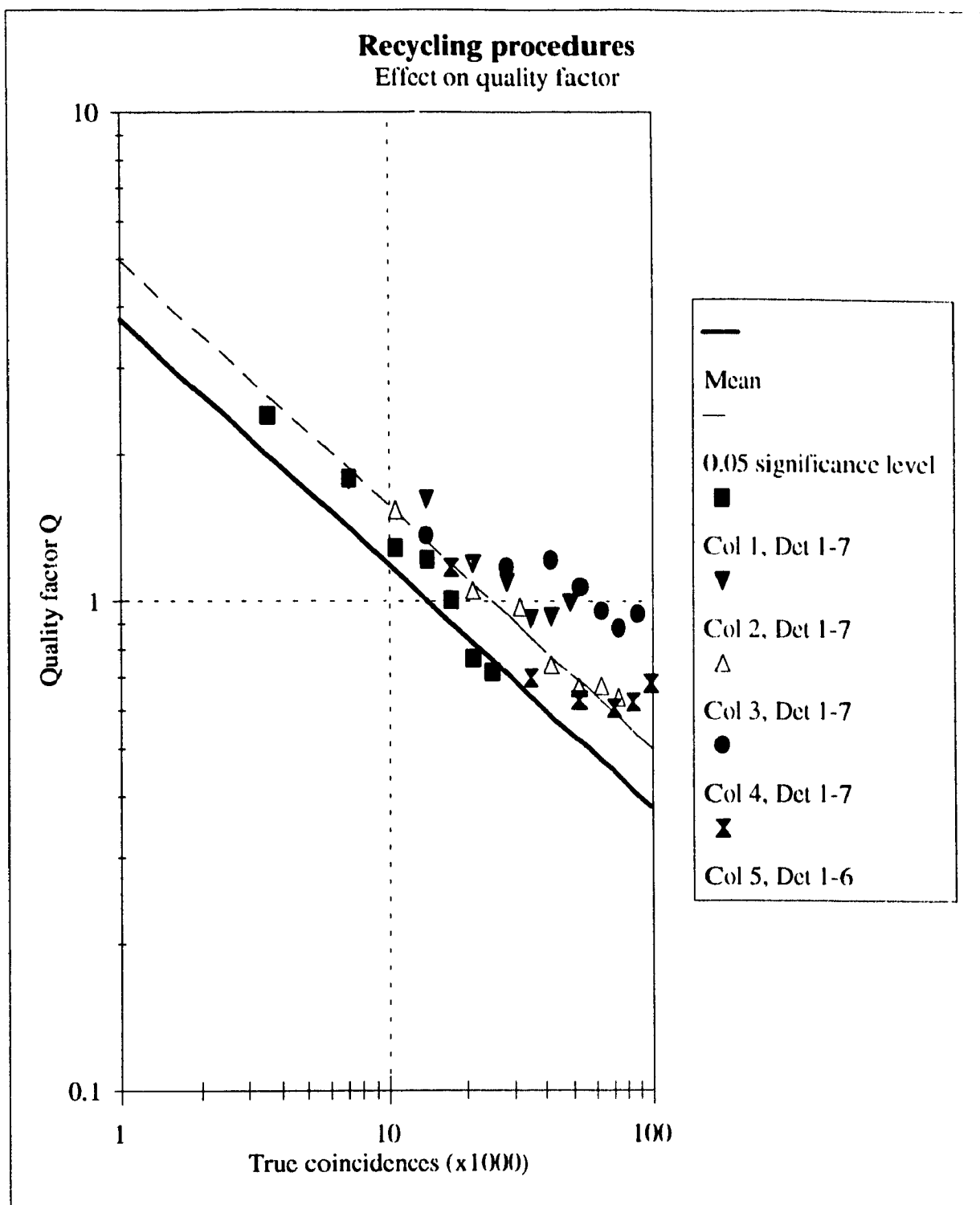


**Figure 5.8** Quality factor for simulations using different recycling procedures. For each set, the left-hand data point corresponds to Det 1 and the right-hand, to Det 7 (Det 6 for the last set).

### A. Time saved

Figure 5.9 presents the relative simulation time required for simulations using different recycling combinations compared to a conventional Monte Carlo simulation. These were computed using the average simulation time to generate 1 event in the mean projection. Remember that to avoid biased results, the total number of counts in the simulated mean projection (used to compute the average simulation time) was reduced using Equation (4.33) when the photons were not following Poisson statistics in a given simulation. This figure shows that when the photons are read twice, in the collimation phase or in the detection phase, the simulation time was about 60% of the simulation time required for a conventional Monte Carlo simulation. It also shows that a reduction to 20% of the simulation time

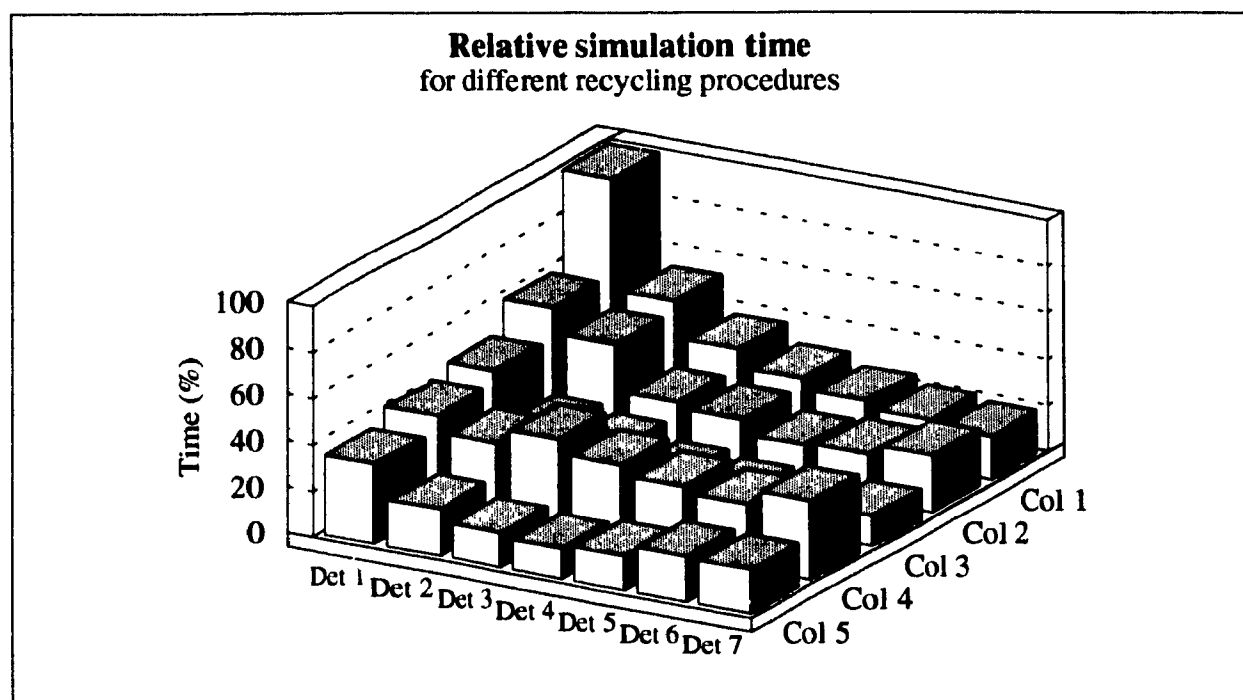


**Figure 5.9** Relative simulation time required for 35 different recycling combinations compared to a conventional Monte Carlo simulation (100%) to obtain a given statistical precision.

required compared to the time of a conventional simulation was achievable when recycling was used many times in the same simulation.

Figure 5.10 presents the relative simulation time required for different phases of the simulation to obtain a given statistical precision for several recycling procedures. For each of them the time to run the source/phantom phase of the simulation were the same since the same GRH file from the source/phantom phase was used for every simulation. However, the simulation times for the other phases were increasing with the number of times the photons were recycled. Since the number of counts in the mean projection was also increasing with the number of times the photons were recycled, the overall effect of recycling was reducing the total simulation time. The sum of the simulation times for each phase of any recycling combination corresponds to the data plotted in Figure 5.9.

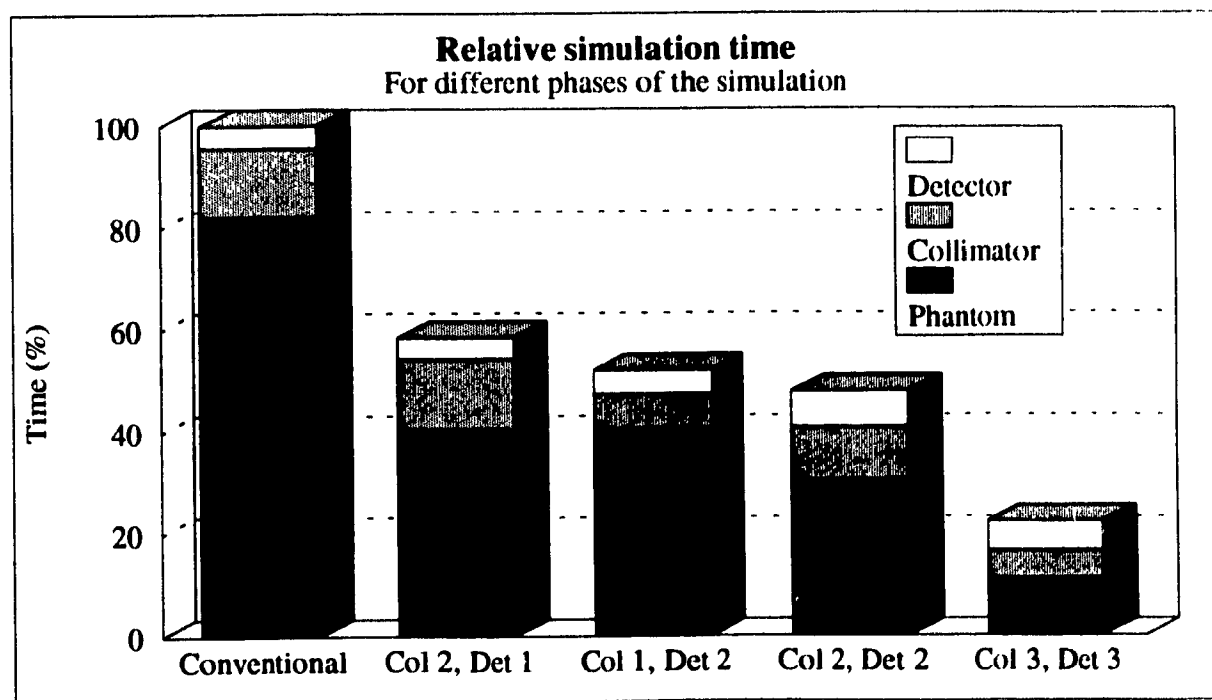


**Figure 5.10** Example of relative simulation time required for different phases of the simulation to obtain a given statistical precision.

### ***B. Disk space saved***

Figure 5.11 presents the relative disk space required for simulations using different recycling combinations compared to a conventional Monte Carlo simulation. These were computed using the average disk space required to generate 1 event in the mean projection. Remember that to avoid biased results, the total number of counts in the simulated mean projection (used to compute the average disk space required) was reduced using Equation (4.33) when the photons were not following Poisson statistics in a given simulation. This figure shows that when the photons are read twice, in the collimation phase or in the detection phase, the disk space required for a simulation is about 60% of the disk space required for a conventional Monte Carlo simulation. It also shows that a reduction to

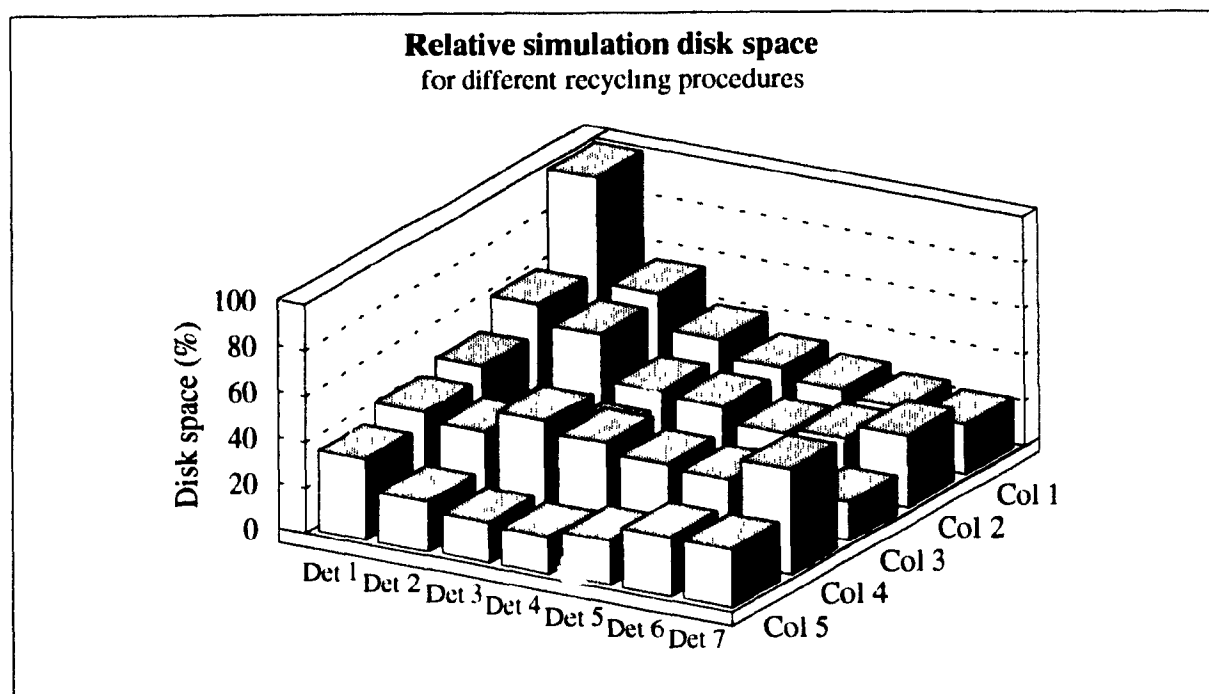


**Figure 5.11** Relative disk space required for 35 different recycling combinations compared to a conventional Monte Carlo simulation (100%) to obtain a given statistical precision.

20% of the disk space required compared to the that of a conventional simulation was achievable when recycling is used many times in the same simulation.

Figure 5.12 presents the relative disk space required for different phases of the simulation to obtain a given statistical precision for several recycling procedures. For each of them, the same GRH file from the source/phantom phase for every simulation was used. However, the disk space required for the GRH files of the other phases were increasing with the number of times the photons were recycled. Since the number of counts in the mean projection was also increasing with the number of times the photons were recycled, the overall effect of recycling was reducing the total disk space used for a given statistical precision. The sum of the disk spaces required for each phase of any recycling combination corresponds to the data plotted in Figure 5.11.

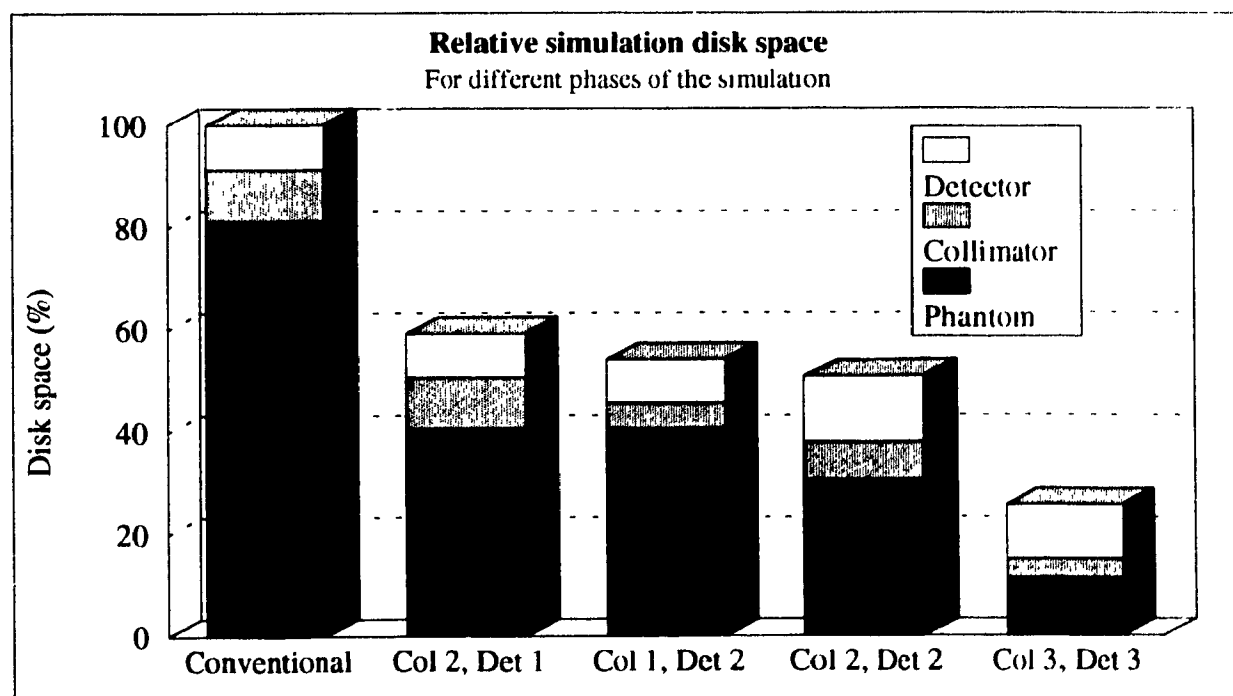


**Figure 5.12** Example of relative disk space required for different phases of the simulation to obtain a given statistical precision.

### Conclusion

---

A technique to produce a look-up table for Monte Carlo simulation of PET scanners that contains information about the Compton scattering and photoelectric linear attenuations for a list of materials that are susceptible to be used in PET was presented. More realistic geometries are now possible, since one can simulate a brain or a heart. This enables one to generate effective count-rate curves for organs of interest as well as traditional flood phantoms. New materials can also be added to the look-up table. Evaluation of new detector materials can then be performed more simply in the simulation program with this new technique.

It was also demonstrated that the efficiency of Monte Carlo simulation programs which cascades the simulation process into phases could be improved by recycling the photon from the previous phases in the collimation and detection phases. When the photons are read twice or three times in a given phase, the recycling technique works well. However, it is considered essential to compare the simulated mean projection with an analytical mean projection to ensure that the photons follow Poisson statistics when the photons are recycled many times in the same phase. Since the recycling technique gives the photons additional chances of being detected, it is suggested to recycle the photons only if the efficiency in terms of the ratio photons in-out of the phase is low. That way, it is more likely to produce a simulation where the photons follow Poisson statistics.

## References

- 
- [1] W.-D. Heiss, C. Beil, K. Herholz, G. Pawlik, R. Wagner and K. Wienhard, *Atlas of Positron Emission Tomography of the Brain* (Berlin: Springer-Verlag, 1985).
  - [2] M.C. Graham, R.E. Bigler, "Principles of Positron Emission Tomography (PET)," *Physics of Nuclear Medicine: Recent Advances*, American Association of Physicists in Medicine (AAPM) Monograph 10, ed. D.V. Rao, R. Chandra and M.C. Graham (New York: American Institute of Physics, 1983), 384-409.
  - [3] S.E. Derenzo, "Precision Measurement of Annihilation Point Spread Distributions for Medically Important Positron Emitters," *Proc. 5th Int. Conference on Positron Annihilation*, ed. R.R. Hasiguti and K. Fujiwara (Sendai: Japan Institute of Metals, 1981), 819-23.
  - [4] Z.H. Cho, J.K. Chan, L. Eriksson, M. Singh, S. Graham, N.S. MacDonald and Y. Yano, "Positron Ranges Obtained from Biomedically Important Positron-emitting Radionuclides," *J. Nucl. Med.* **16** (1975): 1174-6.
  - [5] E.J. Hoffman and M.E. Phelps, "An Analysis of Some of the Physical Aspects of Positron Transaxial Tomography," *Comput. Biol. Med.* **6** (1976): 345-60.
  - [6] M. Deutsch, "Annihilation of Positrons," *Progress in Nuclear Physics* **3** (1953): 131-58.
  - [7] S. De Benedetti, C.E. Cowen and W.R. Konneker, "On the Angular Distribution of Two Photon Annihilation Radiation," *Phys. Rev.* **177** (1950): 205-12.
  - [8] P. Colombino, B. Fiscella and L. Trossi, "Study of Positronium in Water and Ice from 22 to -144°C by Annihilation Quantum Measurements," *Nuovo Cimento* **38** (1965): 707-23.
  - [9] H.E. Johns and J.R. Cunningham, *The physics of radiology*, 4<sup>th</sup> ed. (Springfield, Illinois: Thomas, 1983), 719-25.
  - [10] W. Heitler, *The quantum theory of radiation* (Oxford: Oxford University Press, 1954).
  - [11] O. Klein and Y. Nishina, "Über die Streuung von Strahlung durch freie Elektronen nach der neuen relativistischen Quantendynamik von Dirac," *Zett. Physik* **52** (1929): 853-68.
  - [12] L.R. Lupton and N.A. Keller, *MONTÉ and ANALI: A General Purpose Monte Carlo Simulation for the Design of Single-Slice Positron Emission Tomography Ring Cameras*, Report No. AECL-7680, (Chalk River, Ontario: Atomic Energy of Canada Limited, 1982).



- [13] E.D. Cashwell and C.J. Everett, *A Practical Manual on the Monte Carlo Method for Random Walk Problems* (London: Pergamon Press, 1959).
- [14] N.P. Buslenko, D.I. Golenko, Y.A. Shreider, I.M. Sobol and V.G. Sragovich, *The Monte Carlo Method: the Method of Statistical Trials*, (London: Pergamon Press, 1962).
- [15] J.M. Hammersley and D.C. Handscomb, *Monte Carlo Methods*, (London: Methuen & Co Ltd, 1964).
- [16] J.F. Williamson, "Monte Carlo Simulation of Photon Transport Phenomena: Sampling Techniques," *Monte Carlo Simulation in the Radiological Sciences*, ed. R.L. Morin (Boca Raton, Florida: CRC Press, 1988).
- [17] S.E. Derenzo, "Monte-Carlo Calculations of the Detection Efficiency of arrays of NaI(Tl), BGO, CsF, Ge, and Plastic Detectors for 511 keV photons," *IEEE Trans. Nucl. Sci.* **NS-28** (1981): 131-6.
- [18] N.A. Keller and L.R. Lupton, "PET Detector Ring Aperture Function Calculations using Monte-Carlo Techniques," *IEEE Trans. Nucl. Sci.* **NS-30** (1983): 676-80.
- [19] L.R. Lupton and N.A. Keller, "Performance study of single-slice positron emission tomography scanners by Monte Carlo method techniques," *IEEE Trans. Med. Imag.* **MI-2** (1983): 154-68.
- [20] J. Logan and H.J. Bernstein, "A Monte-Carlo Simulation of Compton Scattering in Positron Emission Tomography," *J. Comp. Assist. Tomograph.* **7** (1983): 316-20.
- [21] C.W. Stearns, C.A. Burnham, D.A. Chesler and G.L. Brownell, "Simulation Studies for Cylindrical Positron Tomography," *IEEE Trans. Nucl. Sci.* **NS-35** (1988): 708-11.
- [22] J.G. Rogers, R. Harrop, P.E. Kinahan, N.A. Wilkinson, G.H. Coombes, P.W. Doherty and D.P. Saylor, "Conceptual Design of a Whole-Body PET Machine," *IEEE Trans. Nucl. Sci.* **NS-35** (1988): 680-4.
- [23] T.K. Lewellen, C.P. Anson, D.R. Haynor, R.L. Harrison, A.N. Bice, S.F. Schubert, R.S. Miyaoka, S.B. Gillispie and J. Zhu, "Design of a Simulation System for Emission Tomographs," *J. Nucl. Med.* **29** (1988): 871.
- [24] M. Dahlbom, L. Eriksson, G. Rosenqvist and C. Bohm, "A Study of the Possibility of using Multi-Slice PET Systems for 3D Imaging," *IEEE Trans. Nucl. Sci.* **NS-36** (1989): 1066-71.
- [25] J.G. Rogers, M. Stazyk, R. Harrop, C.J. Dykstra, J.S. Barney, M.S. Atkins and P.E. Kinahan, "Towards the Design of a Positron Imaging Camera," *IEEE Trans. Nucl. Sci.* **NS-37** (1990): 789-94.
- [26] A.N. Bice, T.K. Lewellen, R.S. Miyaoka, R.L. Harrison, D.R. Haynor, K.R. Pollard, C.P. Hanson and S.B. Gillispie, "Monte-Carlo Simulation of BaF<sub>2</sub> Detectors used in Time-Of-Flight Positron Emission Tomography," *IEEE Trans. Nucl. Sci.* **NS-37** (1990): 696-701.
- [27] C. Michel, A. Bol, T. Spinks, D. Townsend, D. Bailey, S. Grootenck and T. Jones, "Assessment of Response Function in Two PET Scanners with and without Interplane Septa," *IEEE Trans. Med. Imag.* **MI-10** (1991): 240-7.

- [28] G. Tzanakos and S. Pavlopoulos, "Development and Validation of a Simulation Model for the Design of a PET Scanner," *IEEE Trans. Nucl. Sci.* **NS-39** (1992): 1093-8.
- [29] N.A. Keller and L.R. Lupton, *A special purpose Monte Carlo simulation to model detector aperture functions in positron emission tomography ring cameras*, Report No. CRNL-2513 (Chalk-River, Ontario: Atomic Energy of Canada Limited, 1984).
- [30] C.J. Thompson, "The effect of collimation on scatter fraction in multi-slice PET," *IEEE Trans. Nucl. Sci.* **NS-35** (1988): 598-602.
- [31] C.J. Thompson, "The effect of collimation on singles rates in multi-slice PET," *IEEE Trans. Nucl. Sci.* **NS-36** (1989): 1072-7.
- [32] C.J. Thompson, "The effect of detector material and structure on PET spatial resolution and efficiency," *IEEE Trans. Nucl. Sci.* **NS-37** (1990): 718-724.
- [33] C.J. Thompson, "The effects of collimation on PET images noise due to scatter, random counts and dead time," *J. Cereb. Blood Flow and Metab.* **11** (1991): A31-7.
- [34] C.J. Thompson, J.-M. Cantu and Y. Picard, "PETSIM: Monte Carlo simulation of all sensitivity and resolution parameters of cylindrical positron imaging systems," *Phys. Med. Biol.* **37** (1992): 731-49.
- [35] Y. Picard, C.J. Thompson and S. Marrett, "Improving the Precision and Accuracy of Monte Carlo Simulation in Positron Emission Tomography," *IEEE Trans. Nucl. Sci.* **NS-39** (1992): 1111-6.
- [36] Digital Equipment Corporation, *VAX-11 FORTRAN language reference manual* (Maynard, Massachusetts: Digital Equipment Corporation, 1982), C31-2.
- [37] C.J. Thompson, source code of PETSIM (unpublished).
- [38] M.G. Kendall and B. Babington Smith, *Tables of random sampling numbers*, Tracts for Computers **24** (Cambridge: Cambridge University Press, 1939).
- [39] Rand Corporation, *A million random digits with 1000,000 normal deviates* (Glencoe, Illinois: Free Press, 1955).
- [40] J.M. Hammersley, "Electronic computers and the analysis of stochastic processes," *Math. Aids Comput.* **4** (1950): 56-7.
- [41] D.H. Lehmer, "Mathematical methods in large-scale computing units," *Ann. Comput. Lab. Harvard Univ.* **26** (1951): 141-6.
- [42] M. Greenberger, "Notes on a new pseudorandom number generator," *J. Assoc. Comp. Mach.* **8** (1961): 163-7.
- [43] T.E. Hull and A.R. Dobell, "Random number generators," *Soc. Indust. Appl. Math. Rev.* **4** (1962): 230-54.
- [44] J.S. Hendricks, "Effects of Changing the Random Number Stride in Monte Carlo Calculations," *Nucl. Sci. Eng.* **109** (1991): 86-91.
- [45] D.R. Haynor, R.L. Harrison, T.K. Lewellen, A.N. Bice, C.P. Anson, S.B. Gillispie, R.S. Miyaoka, K.R. Polland and J.B. Zhu, "Improving the Efficiency of Emission Tomography Simulations using Variance Reduction Techniques," *IEEE Trans. Nucl. Sci.* **NS-37** (1990): 749-53.

- [46] M.J. Berger, *X-ray and gamma-ray attenuation coefficients and cross sections database V 2.0 Standard reference data*, version 2.0, National Institute of Standards and Technology, Standard Reference data Program, (Gaithersburg, Maryland: U.S. Department of Commerce, 1990).
- [47] J.H. Hubbell, W.J. Veigele, E.A. Briggs, R.T. Brown, D.T. Cromer, and R.J. Howerton, "Atomic Form Factors, Incoherent Scattering Functions, and Photon Scattering Cross Sections," *J. Phy. Chem. Ref. Data* **8** (1979): 69-105.
- [48] J.H. Scofield, *Theoretical Photoionization Cross Sections from 1 to 1500 keV*, Report No. UCRL-51326 (Livermore, California: University of California, Lawrence Livermore National Laboratory, 1973).
- [49] Task Group on Reference Man, *Report of the task group on reference man*, International Commission on Radiological Protection (ICRP) publication #23, 1<sup>st</sup> ed. (New York: Pergamon Press, 1975), 280-324.
- [50] R.C. Weast (ed.), *CRC handbook of chemistry and physics*, 71<sup>st</sup> ed. (Cleveland, Ohio: CRC Press, 1990).
- [51] R. Gariod, R. Allemand, E. Cormoreche, M. Laval and M. Moszynski, "The "Leti" positron tomograph architecture and time of flight improvements," *Workshop on Time-of-Flight Tomography*, Washington University, St. Louis, Missouri, May 1982, 25-9.
- [52] D.W. Townsend, "Positron emission tomography with the high density avalanche chamber positron camera," Université de Genève, Genève, Suisse, Thèse de Privat-Docent, (1987).
- [53] S.I. Ziegler, J.G. Rogers, V. Selivanov and I. Sinitzin, "Characteristics of the New YAlO<sub>3</sub>:Ce Compared with BGO and GSO," *IEEE Trans. Nucl. Sci.* **NS-40** (1993): 194-7.
- [54] A. Del Guerra, "PET: Advances in MWPC cameras," in *Advances in medical imaging and related dosimetry*, Lecture 30, Erice, Sicily, July 1986.
- [55] G.W. McLellan and E.B. Shand, *Glass engineering handbook*, 3<sup>rd</sup> ed. (New York: McGraw-Hill, 1984).
- [56] S.E. Derenzo, H. Zaklad and T.F. Budinger, "Analytical study of a high-resolution positron ring detector system for transaxial reconstruction tomography," *J. Nucl. Med.* **16** (1975): 1166-73.
- [57] E. Tanaka, N. Nohara, T. Tomitani and M. Endo, "Analytical study of the performance of a multilayer positron computed tomography scanner," *J. Comp. Assist. Tomograph.* **6** (1982): 350-364.
- [58] A. Mazé and R. Lecomte, "Analytical study of the effect of collimation on the performance of PET cameras in 3-D imaging," *IEEE Trans. Nucl. Sci.* **NS-37** (1990): 823-831.
- [59] A.C. Evans, C.J. Thompson, S. Marrett and E. Meyer, "Performance evaluation of the PC-2048, a new 15-slice encoded-crystal PET scanner for neurological studies," *IEEE Trans. Med. Imag.* **MI-8** (1991): 245-50.
- [60] M.R. Spiegel, *Theory and problems of Probability and Statistics*, metric ed., Schaum's outline series, (New York: McGraw Hill, 1982).

- [61] G. Baillargeon et J. Rainville, *Introduction à la statistique appliquée: une approche multidisciplinaire*, 5ième éd. (Trois-Rivière, Québec: les éditions SMG, 1976).
- [62] R.V. Hogg and A.T. Craig, *Introduction to Mathematical Statistics*, 4th ed. (New York: Macmillan, 1978).
- [63] W.H. Beyer (ed.), *CRC handbook of tables for probability and statistics* (Cleveland, Ohio: CRC Press, 1966).

# Appendix A: Example of a Simulation Batch File

## Sample file:

```

                                !** Environment definition (I/O to disk) **
$ SET DEF USER$DISK:[MNI.YANI.MONTE]
$ ASSIGN KEAVAX$DKA500:[MNI.YANI.MONTE] PH:
$ ASSIGN KEAVAX$DKA500:[MNI.YANI.MONTE] CO:
$ ASSIGN KEAVAX$DKA500:[MNI.YANI.MONTE] DE:
$ ASSIGN USER$DISK:[MNI.YANI.MONTE] PP:
$ ASSIGN USER$DISK:[MNI.YANI.MONTE] CP:
$ ASSIGN USER$DISK:[MNI.YANI.MONTE] DP:

                                !** Simulation of source/phantom phase **
$ RUN PP:PHANTOM
200000,50          !Maximum number of CPU minutes, low energy threshold in keV
25000,             !Output GRH file size (x10 blocks or x5120 bytes)
PH:WATER.GRH       !Output GRH file name

Water Phantom, diam=20cm, height=11cm, in Air
CYL WATER          10.00, 5.50, -5.50,,,,, Water
CYL AIR            15.00, 6.00, -6.00,,,,, Air
CYL VACUUM         40.00, 10.00, -10.00,,,,, end, phantom description

Water Phantom Source Distribution.
0.0, 0.0, 5.5, 5.5,,,,, !Non-collin. angle, Positron max energy, +/-z limit
1, 0.00,10.00, +5.50, -5.50, 0.00, 0.00, CYL
0,

                                !** Simulation of collimation phase **
$ RUN CP:COLLIMATOR
PH:WATER.GRH       !Input GRH file name
6400,2,1.25,       !Output file size, # of times data read, random displ.
CO:COL_2.GRH       !Output GRH file name
1,12,

3 mm LEAD Scanditronix PC-2048 for 15 slice 30 cm id 50 cm od collimator
CYL AIR            15.0, 8.00, -8.00,,,,, Air until collimators
CYL LEAD_ANTIMONY5% 25.0, 0.15, -0.15,,,,, central 3 mm LEAD
CYL AIR            25.0, 1.10, -1.10,,,,, air between speta
CYL LEAD_ANTIMONY5% 25.0, 1.40, -1.40,,,,, 2nd 3 mm LEAD
CYL AIR            25.0, 2.35, -2.35,,,,, air between speta
CYL LEAD_ANTIMONY5% 25.0, 2.65, -2.65,,,,, 3rd 3 mm LEAD
CYL AIR            25.0, 3.60, -3.60,,,,, air between speta
CYL LEAD_ANTIMONY5% 25.0, 3.90, -3.90,,,,, 4th 3 mm LEAD
CYL AIR            25.0, 4.85, -4.85,,,,, air between speta
CYL LEAD_ANTIMONY5% 25.0, 7.70, -7.70,,,,, lead outer collimator
CYL AIR            25.0, 98.8, -98.8,,,,, air outside collimator
CYL VACUUM         40.0, 99.0, -99.0,,,,, end, collimator description
```

! \*\* Simulation of detection phase \*\*

\$ RUN DP:DETECT

CO:COL 2.GRH !Input GRH file name

16200,3,1.0,, !Output GRH file size, # of time data read, random displ.

DE:COL 2\_DET 3.GRH!Output GRH file name

26.25,50,64,1.0 !Effective radius, low energy threshold, number of blocks,  
!septa thickness

2x64BGO blocks 9.82 cm high 3 cm deep with lead in gaps 50.5 cm diam

CYL AIR 25.25, 4.91, -4.91,,,,, Air in collimator

CYL BGO 28.25, 4.91, -4.91,,,,, BGO crystals

CYL LEAD 28.25, 4.91, -4.91,,,,, Lead

CYL VACUUM 40.00, 12.0, -12.0,,,,, end, detector description

! \*\* end of simulation

\$ EXIT

## Appendix B: Fitting of Photoelectric Coefficients

The photoelectric attenuation data from the XGAM output table consist of  $N$  pairs of measurements  $(h\nu_i, \tau_i)$  of an independent variable, the energy of the photon,  $h\nu_i$  (expressed in keV), and a dependent variable, the photoelectric absorption partial interaction linear attenuation coefficient (expressed in  $\text{cm}^{-1}$ ). The objective is to fit the data with an equation of the form

$$\tau = a \cdot (h\nu)^{-b}, \quad (\text{B.1})$$

by determining the values of the parameters  $a$  and  $b$ . Equation (B.1) can be linearized by taking the natural logarithm on both side of the equation. This operation gives

$$\ln \tau = \ln a - b \ln(h\nu) \quad (\text{B.2})$$

which as the form

$$y = A + Bx, \quad (\text{B.3})$$

where

$$\begin{aligned} y &= \ln \tau \\ A &= \ln a \\ B &= -b \\ x &= \ln(h\nu) \end{aligned} \quad (\text{B.4})$$

The pair of measurements  $(h\nu_i, \tau_i)$  can also be replaced by  $(x_i, y_i)$  using the previous equation. The values of coefficients  $A$  and  $B$  are determined using the method of least-squares fit to a straight line. It consists in determining the coefficient such that  $\chi^2$ , the sum of the squares of the differences between the  $y_i$ 's and the corresponding values ( $y = f(x_i)$ ), is minimized. Mathematically,  $\chi^2$  is defined by

$$\chi^2 = \sum_{i=1}^N (y_i - A - Bx_i)^2. \quad (\text{B.5})$$

The minimum value of this function is one which yields a value of 0 for both of the partial derivatives with respect to each of the coefficients, that is:

$$\begin{aligned} \frac{\partial}{\partial A} \chi^2 &= \frac{\partial}{\partial A} \left[ \sum_{i=1}^N (y_i - A - Bx_i)^2 \right] \\ &= -2 \sum_{i=1}^N (y_i - A - Bx_i) = 0 \\ \frac{\partial}{\partial B} \chi^2 &= \frac{\partial}{\partial B} \left[ \sum_{i=1}^N (y_i - A - Bx_i)^2 \right] \\ &= -2 \sum_{i=1}^N [x_i (y_i - A - Bx_i)] = 0. \end{aligned} \quad (\text{B.6})$$

These equations can be rearranged to yield a pair of simultaneous equations

$$\begin{aligned} \sum_{i=1}^N y_i &= \sum_{i=1}^N A + \sum_{i=1}^N Bx_i = aN + b \sum_{i=1}^N x_i, \\ \sum_{i=1}^N x_i y_i &= \sum_{i=1}^N Ax_i + \sum_{i=1}^N Bx_i^2 = A \sum_{i=1}^N x_i + B \sum_{i=1}^N x_i^2. \end{aligned} \quad (\text{B.7})$$

The solution for the coefficients  $A$  and  $B$  is found by replacing  $A$  in the second of the simultaneous equation by an expression obtained by isolating  $A$  in the first equation. The solutions are



$$\begin{aligned}
 A &= \frac{\sum_{i=1}^N x_i^2 \sum_{i=1}^N y_i - \sum_{i=1}^N x_i \sum_{i=1}^N x_i y_i}{N \sum_{i=1}^N x_i^2 - \left( \sum_{i=1}^N x_i \right)^2} \\
 B &= \frac{N \sum_{i=1}^N x_i y_i - \sum_{i=1}^N x_i \sum_{i=1}^N y_i}{N \sum_{i=1}^N x_i^2 - \left( \sum_{i=1}^N x_i \right)^2}.
 \end{aligned}
 \tag{B.8}$$

The solutions of Equation (B.1) are then

$$\begin{aligned}
 a &= \exp \left\{ \frac{\sum_{i=1}^N (\ln(h\nu_i))^2 \sum_{i=1}^N \ln \tau_i - \sum_{i=1}^N \ln(h\nu_i) \sum_{i=1}^N \ln(h\nu_i) \ln \tau_i}{N \sum_{i=1}^N (\ln(h\nu_i))^2 - \left( \sum_{i=1}^N \ln(h\nu_i) \right)^2} \right\} \\
 b &= - \frac{N \sum_{i=1}^N \ln(h\nu_i) \ln \tau_i - \sum_{i=1}^N \ln(h\nu_i) \sum_{i=1}^N \ln \tau_i}{N \sum_{i=1}^N (\ln(h\nu_i))^2 - \left( \sum_{i=1}^N \ln(h\nu_i) \right)^2},
 \end{aligned}
 \tag{B.9}$$

using Equation (B.4).

## Appendix C: $\chi^2$ Distribution

---

The probability density  $f(x=\chi^2, \nu)$  for  $\chi^2$  is given by

$$f(x=\chi^2, \nu) = \frac{1}{2^{\nu/2} \Gamma(\nu/2)} x^{\nu/2-1} e^{-x/2}, \quad (\text{C.1})$$

where the gamma function is given by the recurrence formula:

$$\begin{aligned} \Gamma(\nu/2) &= (\nu/2 - 1) \Gamma(\nu/2 - 1) \\ \Gamma(1) &= 1 \\ \Gamma(1/2) &= \sqrt{\pi} \end{aligned} \quad (\text{C.2})$$

The probability distribution, that is the probability of observing a value of chi-square smaller than  $\chi^2$ , for a random sample of  $N$  observations with  $\nu$  degrees of freedom is the integral of Equation (C.1), that is:

$$F(\chi^2, \nu) = \frac{1}{2^{\nu/2} \Gamma(\nu/2)} \int_0^{\chi^2} x^{\nu/2-1} e^{-x/2} dx. \quad (\text{C.3})$$